UNIVERSITY OF
BIRMINGHAM

Formulation and application of encapsulated chemical sorbents

By

Gilmore Wellio

A thesis submitted to
the University of Birmingham
for the degree of
DOCTOR of PHILOSOPHY

School of Chemical Engineering
College of Engineering and Physical Sciences
University of Birmingham
October 2020

Abstract

Encapsulated sorbents are emerging as a new tier of composite sorbent materials that furnishes liquid sorbents with the properties of solid sorbents. The favourable properties of selectivity and high loading capacity of liquid sorbents are further enhanced by the discretization into smaller encapsulated units of higher surface area which also reduce solvent loss and retain precipitates and by-products. Recently, encapsulated sorbents have been demonstrated in applications for the removal of CO_2 from effluent gases using advanced solvents with the potential of increasing the energy efficiency of the process with respect to established technologies.

Sorption thermochemical energy storage systems could equally benefit from encapsulation where liquid sorbents consisting of aqueous solutions of hygroscopic salts are prone to crystallization and corrosion issues. It is immediately clear that for such composite materials, shell material development should be geared towards selectively permeable shell materials able to retain the hygroscopic salts whilst allowing exchange of the solvent (water) with the environment. Additionally, such shell materials must have sufficient mechanical strength to withstand rupture as well as thin walls to minimise

mass transfer resistances. Moreover, the impact of the deformability of the encapsulated sorbents under external loads, such as in packed beds, on the sorption performance requires greater investigation. In this work a microfluidic approach is utilized for the encapsulation of aqueous solutions of $LiBr$ and $CaCl_2$ using thiol-ene-based photopolymers for the shell material. A simplified technique for the construction of glass capillary microfluidics is presented and assessed and the mechanical and sorption properties of microcapsules with different shell materials characterised.

A microfluidic device (MFD) assembled from capillaries of a predetermined size connected with specially designed 3D-printed connectors was used to form core-shell microcapsules by exposing generated double emulsions to ultra-violet light (365 nm). It was shown that the device assembly technique allowed for reproducible MFDs and that double emulsion generation modes were consistent with theoretical predictions in-spite of fluctuating flow systems during the emulsion generation process thus highlighting the device robustness. Additionally, a decussate droplet generation mode, where double and single emulsion droplets are generated alternatively, was also observed and it was shown that the number of oil droplets increased with the continuous phase flowrate whilst the total oil volume remained unchanged. Microcapsules with a water core and three types of shell materials made from bi-, tri- and tetra-functional thiol monomers reacting with a tri-functional alkene were produced utilizing the free-radical photo-initiated thiol-ene reaction (named DT, PT and TT microcapsules, respectively). Observation of the dehydration process of the microcapsules at ambient conditions revealed extensive buckling for the DT microcapsules followed by the TP and TT mi-

crocapsules, respectively, in correlation with extent of cross-linking. Initial buckling time followed the same trend and also corroborated by dynamic water vapour loss measurements of the three microcapsule types. The deformation behaviour and mechanical strength of the microcapsules were characterised using the micromanipulation technique. Elastic behaviour was shown for DT and PT microcapsules whereas TT microcapsules showed elastic-plastic behaviour with a distinguishable yield point. This was in agreement with glass transition measurements which showed DT and PT microcapsule shells were in the rubbery state and TT microcapsules in the glassy state at the measurement temperature. Modelling of the force and displacement micromanipulation data showed good agreement with the Hertz model for TT microcapsules and with the Tatara model for the rubbery DT and PT microcapsules. The mean Young's moduli of the capsules were determined to be 31.1 $\pm$ 3.4 MPa, 9.0 $\pm$ 3.2 MPa and 135.9 $\pm$ 1.8 MPa for the DT, PT and TT microcapsules, respectively. However, these values were shown to represent a first approximation due to volume changes as a result of the permeability of the microcapsule shell wall.

These shell materials were used further to successfully encapsulate aqueous $LiBr$ solution alongside two additional shell materials, a fluoropolymer (F) and a thiol-ene polymer formed from a terta-thiol and bi-functional alkene (TP). Additionally, the DT shell material was also used to encapsulate $CaCl_2$ salt solution for comparison with the $LiBr$ core. The water vapour sorption dynamics of the microcapsules were characterised by simultaneous thermal analysis (STA). A linear driving force model allowed for the sorption properties to be compared using a single parameter, the time constant. The

absorption-desorption cycle stability was assessed by comparing the consecutive cycles which indicated loss of the salt from the core. Further examination of the microcapsules by a combination of scanning electron microscopy and x-ray computed tomography showed that a layer of salt crystals forms along the internal surface of the microcapsules during desorption cycles. This verification provides insight into the sorption-desorption transport mechanism and indicates the possible driving force for salt loss.

This work can serve as an early guide to the development of encapsulated chemical sorbents for thermochemical energy storage applications. The combination of microfluidics and photopolymers has been shown to be amenable for prototyping of these new sorbent materials. Formulation and mechanical property considerations have been highlighted. The studies on the distribution of the salt core after absorption-desorption cycling will be beneficial to future work in shell material development.

Contents

List of Figures

List of Tables

List of Abbreviations

a	Surface area $[m^2]$
Bo	Bond number [-]
C	Compliance $[m]$
c_1	Arbitrary constant 1 [-]
c_2	Arbitrary constant 2 [-]
Ca	Capillary number [-]
CV	Coefficient of variation [%]
C_ν	Volumetric concentration of water vapour [-]
D	Particle diameter $[m]$
$d_{4,3}$	Volume mean diameter [m]
d_a	Alignment capillary internal diameter $[m]$
d_c	Collector capillary orifice diameter $[m]$
D_{cap}	Double emulsion diameter $[m]$

D_{core}	Double emulsion core diameter $[m]$
d_i	Injector capillary external diameter $[m]$
d_k	Diameter of the kth particle [m]
d_n	Injector capillary orifice diameter $[m]$
D_{oil}	Oil droplet diameter $[m]$
d_{thread}	Fluid thread diameter $[m]$
$d_{v0.1}$	Size below which 10vol% of material is contained $[m]$
$d_{v0.5}$	Size below which 50vol% of material is contained $[m]$
$d_{v0.9}$	Size below which 90vol% of material is contained $[m]$
d_ϵ	Displacement error $[m]$
E	Young's modulus $[Pa]$
f	Centre-to-centre distance of microcapsule and core $[m]$
F	Frequency of droplet generation $[Hz]$
F_c	Compressive force $[N]$
f_ϵ	Enhancement factor [-]
g	Acceleration due to gravity $[m\ s^{-2}]$
$\overline{h}$	Average microcapsule shell thickness $[m]$
h	Microcapsule shell thickness $[m]$
L	Characteristic length $[m]$
l	Injector-collector capillary distance $[m]$

m	Mass $[kg]$
$\dot{m}$	Water mass flowrate $[kg\ s^{-1}]$
m_0	Initial mass $[kg]$
m_{eq}	Equilibrium mass $[kg]$
M_R	Relative molar mass $[g\ mol^{-1}]$
$\dot{n}$	Molar flux $[mol\ s^{-1}]$
P	Total pressure $[Pa]$
p	Vapour pressure $[Pa]$
p_0	Reference pressure $[Pa]$
p_c	Actual vapour pressure $[Pa]$
p_{cap}	Internal capsule pressure $[Pa]$
PCM	Phase change material
P_{H_2O}	Water vapour permeability $[m^{-1}]$
p_{sat}	Saturated vapour pressure $[Pa]$
Q	Volumetric flowrate $[m^3\ s^{-1}]$
Q_{cond}	Heat of condensation $[W]$
Q_g	Volumetric gas flowrate $[m^3\ s^{-1}]$
R	Microcapsule radius $[m]$
r	Radius $[m]$
r	Microcapsule core radius $[m]$
R_c	Critical radius $[m]$
Re	Reynold's number [-]
R_G	Universal gas constant $[J\ mol^{-1}\ K^{-1}]$
RH	Relative humidity [-]

R_θ	Thermal resistance $[K\ W^{-1}]$
s	Span of size distribution [%]
t	Time $[s]$
T_{eq}	Equilibrium temperature $[K]$
TES	Thermal energy storage
T_g	Glass transition temperature $[°C]$
$\overline{u}$	Average fluid velocity $[m\ s^{-1}]$
u	Fluid velocity $[m\ s^{-1}]$
u_c	Compression speed $[m\ s^{-1}]$
V_0	Initial volume $[m^3]$
V_{core}	Average inner phase volume per emulsion droplet $[m^3]$
V_{oil}	Average middle phase volume per emulsion droplet $[m^3]$
We	Weber number [-]
x	Conversion [-]
x_0	Equilibrium conversion [-]
ΔH	Molar enthalpy change $[J\ mol^{-1}]$
ΔP	Pressure difference $[Pa]$
ΔP_c	Critical buckling pressure $[Pa]$
ΔP_{plat}	Plateau pressure drop $[Pa]$
Δp_{vap}	Partial vapour pressure difference $[Pa]$
ΔQ	Heat flow $[W]$
ΔS	Molar entropy change $[J\ mol^{-1}\ K^{-1}]$

ΔT	Temperature difference $[K]$
ΔV	Volume change $[m^3]$
γ	Interfacial tension $[N\ m^{-1}]$
δ	relative displacement $[m]$
ζ	Empirical flow parameter [-]
η	Effective liquid viscosity $[Pa\ s$
κ	Transducer sensitivity $[m]$
$\overline{\mu}$	Coefficient of variation [%]
μ	Dynamic viscosity $[Pa\ s]$
ν	Poisson's ratio [-]
ρ	Density $[kg\ m^{-3}]$
σ	Standard deviation
τ	Characteristic time $[s]$

CHAPTER 1

Introduction

1.1 Background

The microencapsulation of chemical sorbents separates the sorbent from the external environment whilst allowing mass transfer through a semi-permeable membrane. Mass transfer rates are enhanced by the resulting increase in surface area. For volatile chemical sorbents or those with high viscosity, toxic or precipitant by-products, slow absorption kinetics and corrosive properties (Vericella et al. (2015) and Moore et al. (2018)); microencapsulation could be a game changer. Benign, low cost solvents that are lean in water and thus more energy efficient can now be considered as competitive alternatives against problematic conventional solvents in applications such as carbon dioxide capture. For liquid chemical sorbents, it combines the benefits of liquid sorbents with those of solid adsorbents.

Microencapsulation is a versatile technique with a broad range of methods

developed for the encapsulation of various materials with benign or aggressive chemical properties. The encapsulating material can be organic or inorganic depending the application requirements and properties of the encapsulated material. Furthermore, the morphology of the microcapsule can be controlled to form matrix structures, microcapsules with hierarchical porosity as well as the simple core-shell structure. In core-shell microcapsules, the chemical sorbent is confined in a central core surrounded by a thin semipermeable shell. Mass transfer through the shell is often the rate-limiting step and can thus be controlled by the choice of material permeability and thickness. This presents an opportunity for tailoring composites for chemical sorption application. The shell also governs the microcapsule mechanical properties and can be tailored to allow a microcapsule to accommodate volume changes due to sorbate uptake or resist buckling as a result of sorbate loss. There is therefore a need to identify desirable shell mechanical properties for particular sorbent applications given the large number of permutations made possible through sorbent encapsulation.

Microencapsulation of liquid sorbents for CO_2 capture addresses the key issues of high energy penalty and high equipment cost associated with the conventional systems which use aqueous amine solutions. Novel solvents based on aqueous carbonate solutions and ionic liquids have been proposed as candidate solutions with low energy penalty, low degradation or low corrosion (Yu et al. 2020). These solvents have limitations posed by precipitates and high viscosity, respectively, however, their performance has been enhanced by microencapsulation (Vericella et al. (2015) and Nabavi et al. (2016)).

Another area that could potentially benefit from the use of encapsulated

sorbents is that of thermochemical energy storage. In this field, hygroscopic salts, their hydrates and solutions are used to store and release thermal energy by desorbing or absorbing water vapour. The energy is stored in chemical form, minimising thermal losses, making this an attractive energy storage technology, particularly in domestic solar heating/cooling applications. A key challenge with using salt hydrates for thermochemical energy storage is the liquefaction and subsequent loss of the salts as well as reduced surface area due to agglomeration of salts leading to a deterioration in cycle stability. Impregnation of the salt in porous host matrices such as vermiculite, expanded natural graphite and zeolites has been used as a method to stabilise the salt (Aristov 2012). Such composites inevitably have reduced energy storage densities and slower reaction rates. To the best of the author's knowledge, the only research on encapsulating thermochemical energy storage material was by Gaeini et al. (2018) who produced spray-dried microcapsules with a calcium chloride core and ethyl cellulose shell and found them to have greater cycle stability and faster kinetics compared with the salt-in-matrix samples. However, these microcapsules had a comparatively lower volumetric energy storage density than their salt-in-matrix counterparts.

The primary focus of this work is to study the mechanical and sorption/desorption properties of microencapsulated thermochemical materials. This work contributes to the development of new composite energy storage materials in the form of microencapsulated thermochemical materials and to understanding the impact of the morphological, mechanical chemical properties on the sorption performance, energy storage capacity and stability. The long-term goal is to create a facile method of developing tailored sorbents that

could have significant impact in delivering targeted and optimised systems in the future. The main goals are: a) formulation: design a facile method to produce microencapsulated sorbents under benign conditions and produce microencapsulated thermochemical materials (MTCMs) for further analysis; b) microcapsule characterisation: analyse the chemical and mechanical properties of MTCMs with the use of the micromanipulation techniques to fully characterise their mechanical properties; c) sorption/desorption dynamics: analyse their dynamic sorption/desorption properties as measured using the simultaneous thermal analysis (STA) technique and characterise their cycle stability through a combination of three-dimensional imaging and scanning electron microscopy (SEM).

The thesis outline is presented Section 1.2.

1.2 Thesis layout

Chapter 2

An overview of the microencapsulation techniques available for the encapsulation of chemical sorbents are presented. Particular focus is placed on the promising technique of microfluidics including microfluidic device fabrication and operation. A survey of the use of encapsulated sorbents in a range applications is also executed and the key requirements of microcapsules for each application is discussed. Furthermore, thermochemical energy storage is introduced in greater detail and the potential benefits offered by microencapsulation in this field is identified. Lastly, the characterisation of

the mechanical properties of microcapsules is presented, including the micromanipulation technique and the determination of parameters such as the Young's modulus by the use of surveyed models. The impact of these mechanical parameters is discussed in relation to the performance of microcapsules at different operating conditions.

Chapter 3

The materials and methods applied in the formulation and characterisation of microcapsules are presented. The conditions for sorption/desorption experiments and equipment configurations are also described.

Chapter 4

The preparation of glass capillary microfluidics is described in detail including a discussion on the practical implications and issues addressed as well as the operation of the devices to produce microcapsules. Results of the effect of the variation of microfluidic parameters on the microcapsules produced are discussed. Additionally, the measurement results of microcapsule size and shell thickness distributions and heterogeneity are presented.

Chapter 5

In this chapter, the mechanical strength of microcapsules produced from three types of thiol-ene shell material is presented and the impact of glass transition temperature and cross-link density discussed. Furthermore, the water vapour permeability of the microcapsules is presented and its impact

on the mechanical behaviour under compression discussed and their impact on sorption performance considered.

Chapter 6

The sorption/desorption results of thiol-ene and fluoroacrylate microcapsules with a $LiBr$ and $CaCl_2$ core are presented. Size and thickness distribution as well as salt loading capacity data are also presented and their impact on the sorption dynamics and energy storage capacity discussed. The microcapsule stability results are also presented and the use of three-dimensional characterisation techniques on microcapsule salt leaching is demonstrated.

Chapter 7

The overall conclusions are presented in this final chapter, including recommendations for future work.

CHAPTER 2

Literature review

In this chapter, the application of encapsulated chemical sorbents is presented with specific literature examples in the more advanced CO_2 capture applications. Subsequently, the sorption and mechanical property requirements for microcapsules with encapsulated sorbents are determined with specific focus on their application in the encapsulation of sorption thermochemical materials for energy storage. Available techniques of microencapsulation are reviewed with particular focus on microencapsulation by microfluidics, identified as a suitable technique for the rapid prototyping of encapsulated materials. An overview of the characterisation of the mechanical properties of microcapsules is also presented, in particular, the use of micromanipulation in the determination of microcapsule deformation behaviour and intrinsic material properties based on a variety of modelling methods also reviewed in this chapter. The field of sorption thermochemical energy storage is also introduced and potential benefits of microencapsulation in the development

of new composite sorbents in the context of this field are also discussed. Furthermore, the characterisation techniques of composite sorption materials are also discussed to allow for the selection of appropriate methods for the characterisation of encapsulated sorption thermochemical materials.

2.1 Application of encapsulated liquid sorbents

The application of encapsulated solvents in the field of CO_2 capture has been the subject of much interest over the last decade. The limitations of the mature amine-based CO_2 scrubbing technology are well established and act as a reference point for quantifying the benefits of any new technological improvements. Encapsulation offers a solution to challenges faced in using the different solvents currently available for CO_2 capture. The encapsulating shell is able to retain volatile solvents, precipitates (when beneficial as with aqueous potassium and sodium carbonate solutions), degradation products as observed with amine solvents (Gouedard et al. 2012) as well as minimising contact between corrosive solvents and vessel walls. The challenges and developments in this particular application field serve as key learning points for similar future applications involving encapsulated solvents that exchange species through a semi-permeable shell.

Stolaroff et al. (2016) encapsulated water-lean solvents for CO_2 absorption applications. Solvents with a lower water content reduce the thermal energy consumption in post-combustion carbon capture systems compared with conventional aqueous amine-based systems which require heat to remove water during regeneration of the solvent. However, these solvents have high

viscosity and slow CO_2 uptake rates which was shown to be improved by 3.5 times compared with a liquid film as a result of the encapsulation of an ionic liquid in 100 – 600 μm microcapsules with a poly(dimethylsiloxane)-based (PDMS-based) shell (Stolaroff et al. 2016).

Another group of alternative solvents to the traditional amine solvents are those based on the aqueous solutions of the inorganic salts K_2CO_3 and Na_2CO_3. The carbonate solutions are relatively cheap, have low toxicity and low volatility and do not degrade in comparison to amine solutions (Knuutila et al. 2009). K_2CO_3 and Na_2CO_3 solutions (up to 30wt% carbonate) were encapsulated with a silicone shell material (permeability, 3260 $Barrer$) by Vericella et al. (2015) in order to overcome issues related with slow absorption kinetics and handling of precipitates which are drawbacks to using these salt-based solvents. In this instance, absorption was improved by nearly an order of magnitude compared with liquid pools of the solvent with an equivalent surface-to-volume ratio to packed towers. Additionally, sorption capacity was shown to be similar to that in amine-based systems, however, operating at more moderate solvent regeneration temperatures ($70°C$ – $150°C$) than the latter.

The silicone shell material used was also permeable to water and depending on the operating conditions, loss of water resulted in precipitation of the carbonates, reducing absorption capacity. Under conditions where absorption of water occurred instead, an energy penalty during solvent regeneration was introduced. Buckling and swelling of the capsules during these processes also affected the overall mass transfer rates as demonstrated in the modelling work of Finn & Galvin (2018). In a subsequent work, Finn et al. (2019) also

showed that water loss from the capsules was enhanced in a packed bed by compression due to the gas flow. This compression induced mass flow was affected by the capsule properties such as shell thickness and Young's modulus as well as the microcapsule size.

Chen et al. (2014) produced acrylic microcapsules with amine cores of triethylenetetramine (TETA) and diethylenetriamine (DETA). The core was initially encapsulated as an aqueous solution by double emulsion templating in microfluidics and the water later removed by heating resulting in a more concentrated amine content in the core. This work demonstrated a method to utilise selective permeability of the shell to modify the properties of the core after microencapsulation.

Formation of microcapsules in the previously described works, relied on double emulsion templated formation of microcapsules by microfluidics. This is a method that allows for the flexible generation of double emulsions with rapid results and is particularly important for explorative works involving shell material screening. Santiago et al. (2018) encapsulated ionic liquids in an inorganic shell through a process which involved the creation of silica-based templates using the sol-gel process and silica nano-particles, followed by calcination and subsequent loading with a carbon precursor and finally, a pyrolysis step to form 'carbon capsules' which were used as a porous matrix for carrying ionic liquid cargo. Microcapsules produced in this manner had sub-micron sizes and thus high surface area, however, the steps involved in their preparation could be potentially costly from an economic and sustainability point of view.

The potential benefits that such microencapsulated solvents can have

over mature technologies such as packed beds are not a sovereign remedy to the drawbacks of such systems. The diminutive scale of microencapsulated solvents enhances viscous resistance effects to the replenishment of unspent solvent near the capsule wall impacting the mass transfer kinetics. The shell material also introduces an additional mass transfer resistance and finally, for sufficiently small microcapsules, absorption rates may be controlled by the reaction kinetics, in which case, there would be no further mass transfer enhancement. On the basis of these considerations, Moore et al. (2018) concluded that microencapsulation can be expected to increase the specific absorption rate of gases by one and up to two orders of magnitude for chemical and physical solvents, respectively.

The use of a selectively permeable membrane as the shell material allows for exchange of the sorbate with the solvent without any losses of the solvent. Research in this field has focussed on solvent-compatible shell materials with high permselectivity for the sorbate and good thermal resistance. However, the mechanical properties of the capsule can also have a significant impact on the mass transport properties of the microcapsules beyond the simple requirement of high rupture strength to prevent solvent loss. For example, Finn & Galvin (2018) observed enhanced water loss rates from the core of microcapsules produced by Vericella et al. (2015) under humid conditions due to slight compression in a fluidized/packed bed. Compression of the highly deformable microcapsules (wall thickness 10 – 50 μm and Young's modulus circa 150 kPa) raised the internal pressure in the core such that the solvent was forced through the semi-permeable shell. A model was developed to predict water loss in the capsules accounting for the rise in internal pressure

due to compression by utilizing a model developed by Taber (1982) for the deformation of a thick-walled microcapsule under a point load. Such a change in the solvent concentration affects the CO_2 sorption performance of the encapsulated sorbent and highlights the importance of understanding the mechanical properties and deformation behaviour of encapsulated sorbents.

In summary, microencapsulation of chemical sorbents has the potential to improve the sorption kinetics by increasing the surface area available for mass transfer. It also allows for the containment of volatile or corrosive solvents as well as undesirable by-products or precipitates. Such advantages have been utilized in the development of new sorbent materials for CO_2 capture but could be equally applied in other sorption processes limited by slow kinetics, precipitates and unwanted by-products. The importance of the mechanical properties to the mass transfer processes has also been demonstrated and this is a field still requiring significant research. These factors are governed by the materials and methods of microencapsulation and are introduced in the following subsection.

2.2 Microencapsulation techniques of chemical sorbents

The process of microencapsulation involves isolating a specific material; either solid, liquid or gas from the environment, by encasing it in a shell to form particles in the mircometer scale (Giro-Paloma et al. 2016). The required shell material must be inert with respect to the core and possess the mechanical and thermal stability to withstand the thermal and mechanical

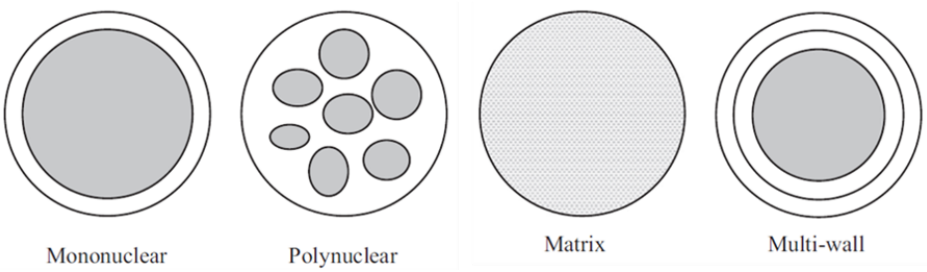

Figure 2.1: Different morphologies of microcapsules as illustrated by Jamekhorshid et al. (2014).

stresses under the expected working conditions.

Microencapsulation enhances heat and mass transfer due to the higher surface-to-volume ratio (Jamekhorshid et al. 2014). The microcapsule may take many forms depending on the properties of the core material and the encapsulation technique used. Common morphologies include the mononuclear, poly-nuclear, matrix and multi-wall forms as illustrated in Figure 2.1.

Microencapsulation techniques can be categorised according to the type of process as chemical, physico-chemical and physical (Jamekhorshid et al. (2014) and Krajišnik et al. (2017)) as summarised in Figure 2.2. The choice of microencapsulation method depends on the properties of the core and shell precursors (or final shell properties) as well as the desired scale of microcapsule production. The technique of microfluidics has been included as a separate technique in Figure 2.2 as it can encompass elements of the other three techniques and differs primarily in that highly monodisperse microcapsules can be formed with this technique.

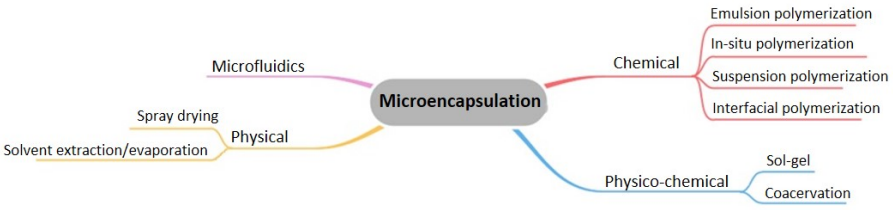

Figure 2.2: Schematic of microencapsulation techniques.

Chemical methods

The chemical methods of encapsulation are dominated by heterogeneous polymerisation, which usually occurs in systems of two immiscible liquids, with one dispersed in the other. The emulsification step determines the size and size distribution of the resulting microcapsules. The monomers and initiator molecules may be present in either of the liquid phases or both depending on the system of polymerisation.

- *Interfacial polymerisation*

  Interfacial polymerisation occurs at the interface of two immiscible liquids which are also solutions of the reactive monomers (Yashin & Balazs 2004). In an emulsion, the monomers are contained in the dispersed and continuous phases and react at the interface. Diffusion of the monomers to the interface is gradually inhibited by the growing polymer wall at the interface which influences the properties of the shell (Perignon et al. 2015).

- *In-situ polymerisation*

  The key difference of this method to the former, as highlighted by Alva et al. (2017), is that it involves no monomers but rather pre-polymers

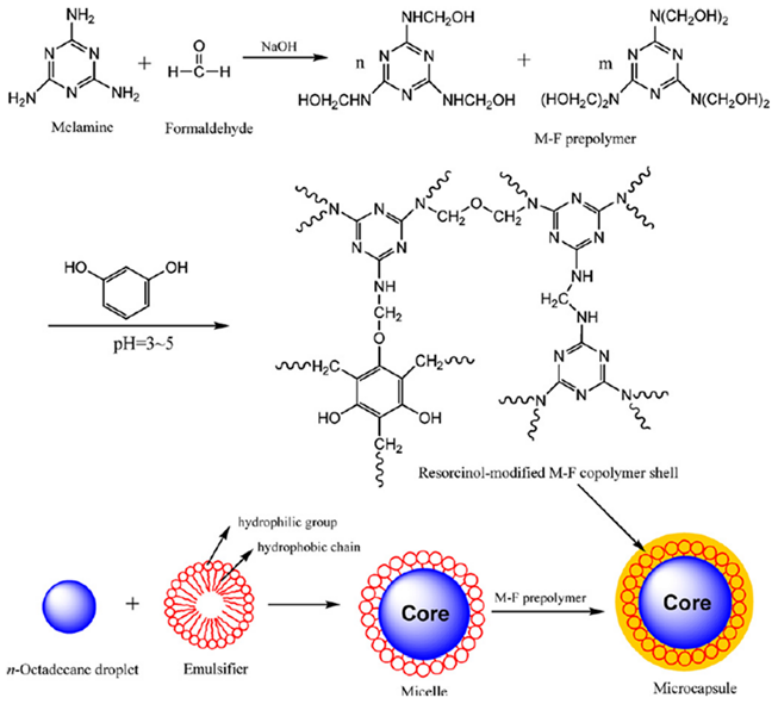

Figure 2.3: Schematic of the microencapsulation of n-octadecane with a melamine-formaldehyde shell by Zhang & Wang (2009).

(or polymer precursors), in the polymerisation step. An illustrative schematic of this technique is shown in figure 2.3 for the encapsulation of n-octadecane (a phase change material) with a melamine-formaldehyde (MF) shell from the work of Zhang & Wang (2009).

- *Suspension polymerisation*

  This method involves free radical polymerisation where the initiator is soluble in the monomer and both are insoluble in the bulk fluid (Arshady 1992). Suspension of the monomer phase is attained through continuous stirring and action of an appropriate droplet stabiliser which may also act to prevent the agglomeration of the polymer particles or microbeads to be formed. Initiation of the polymerisation is triggered

at the appropriate temperature and continuous stirring allows for a narrow size distribution of the particles formed.

- *Emulsion polymerisation*

  Emulsion polymerisation is another method involving free radical polymerisation. An emulsion of a relatively insoluble monomer phase is dispersed in the polymerisation medium and stabilised by a surfactant. In contrast with suspension polymerisation, the initiator is soluble in the polymerisation medium and insoluble in the monomer phase (Arshady (1992) and Alva et al. (2017)). The monomer is distributed within the polymerisation medium in droplets, surfactant micelles and as dissolved species. Initiation of the polymerisation occurs in the bulk phase, forming oligoradicals which can grow by the continued addition of more oligoradicals or monomers, stabilised by the surfactant molecules (Jamekhorshid et al. 2014). However, oligoradicals can also enter micelles which subsequently polymerise. Micelles are aggregates of $\sim$ 102 surfactant molecules formed when the surfactant concentration is above the critical micelle concentration (van Herk & Gilbert 2013).

Physical-chemical methods

The physical-chemical group of microencapsulation techniques includes methods which combine aspects of both the chemical and physical encapsulation techniques. Due to compatibility of the shell material to solvents discussed in this work, the sol-gel process is highlighted under this group of methods.

It is also one of the few methods available for producing inorganic shell materials. However, important techniques such as coacervation (Giro-Paloma et al. 2016) also fall under this group of techniques but will not be covered here.

- *Sol-gel method and sol-gel microencapsulation*

  The sol-gel process allows for the formation of metal and metalloid oxides from their alkoxides, usually at ambient temperatures. For a single alkoxide species such as $Si(OR)_4$, where R represents a short chain alkyl group, the process involves a hydrolysis step followed by a polycondensation step as shown below (Zhang et al. 2011):

  Hydrolysis

  $$Si(OR)_4 + H_2O \rightleftharpoons Si(OR)_3OH + ROH \tag{2.1}$$

  Polycondensation

  $$Si(OR)_3OH + Si(OR)_4 \rightleftharpoons (RO)_3Si - O - Si(OR)_3 + ROH \tag{2.2}$$

  $$2Si(OR)_3OH \rightleftharpoons (RO)_3Si - O - Si(OR)_3 + H_2O \tag{2.3}$$

  These reactions result in the formation of colloidal particles (solid particles with diameters 1-100 nm) constituting a sol which is defined as a dispersion of colloidal particles or polymers in a liquid. Formation of the sol is followed by gelation of the discrete colloidal particles or by disordered networks of covalently or physically linked polymer chains formed by the polycondensation reaction (Hench & West 1990).

A common silica precursor for microencapsulation is tetraethoxysilane (TEOS) and was used by Zhang et al. (2011) to encapsulate n-octadecane with a silica shell. An archetypal procedure, it involved the dropwise addition of sol solution based on TEOS into an oil-in-water (o/w) emulsion of n-octadecane in acid catalyst, resulting in the formation of a silica shell due to polycondensation of the hydrolysed TEOS. The microcapsules formed showed improved thermal conductivity of the shell due to the presence of silica compared with polymer shells such as melamine formaldehyde (MF).

Physical techniques

- *Solvent evaporation*

  The solvent evaporation method is widely used in the development of slow release drugs in the pharmaceutical industry. Realisation of the final microcapsule form with the encapsulated active pharmaceutical ingredient (API) depends on the hydrophilicty or hydrophobicity of the API, however, in all cases the formation of the polymer shell is a result of the evaporation of a solvent from an emulsified polymer solution. The API release profile depends on the microcapsule size, morphology and encapsulation efficiency which are properties governed by the emulsion properties and operating conditions such as temperature and pressure (Li et al. 2008).

- *Spray drying*

  Spray drying is used industrially for the production of various powder

products as it allows for continuous production at high throughput. In encapsulation, this process involves the following steps: (a) a solution of the encapsulating material with an appropriate solvent is prepared, this is immiscible with the core material; (b) an emulsion of the "shell solution" with the core liquid is formed; (c) the emulsion is atomised and dried (spray-dried) to form microcapsules (I Ré 1998). Table 2.1 summarises the techniques and their advantages and disadvantages.

The techniques summarised in Table 2.1 are excellent for the bulk production of microcapsules and the resulting microcapsules have characteristically broad size distributions as well as shell thickness distributions. This variability in the microcapsule sizes emanated from the emulsification method used in these techniques which usually involves high shear mixing of the immiscible phases. For monodisperse size distributions with values of the coefficient of variation (CV) less than 10%, microfluidics are often used and offer control of not only the microcapsule size but the shell thickness and the ability to create higher order emulsions.

2.3 Microfluidic generation of microcapsules

Microfluidics involve the manipulation of fluids at the sub-millimetre scale. At these length-scales fluid flow is laminar and viscous and surface tension effects dominate over gravity effects (Rapp 2017*a*). Flow generation is usually achieved through the use of syringe pumps that inject fluid into the microchannels. Combining flows of immiscible fluids in a device of a specific geometry allows emulsions to be generated with precise control on emulsion

Table 2.1: Summary of advantages and disadvantages of various microencapsulation techniques (Wang, Hui et al. (2020); Giro-Paloma et al. (2016)).

Method	Size [μm]	Advantages	Disadvantages
Chemical			
In-situ	0.05 - 1100	Simple operation Uniform shell	Difficult to control
Interfacial polymerisation	0.5 - 1000	Fast process and compact shell formation	Limited core-shell combinations
Emulsion	0.05 - 5	Fast process producing a high molecular weight shell	
Suspension	2 - 4000	Cost effective	Limited water-soluble monomers
Physicochemical			
Sol-gel	0.2 - 20	Mild reaction conditions Shell with high thermal conductivity	Relatively new process in microencapsulation
Physical			
Solvent evaporation	0.5 - 1000	Simple operation	Use of harsh solvents
Spray drying	5 - 5000	Low-cost and high throughput	Agglomeration of particles Coating is not always guaranteed

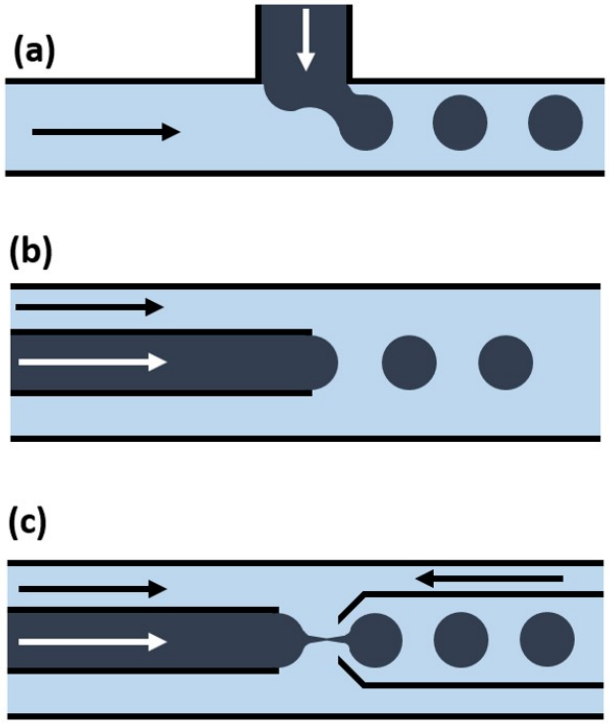

Figure 2.4: Schematic of common microfluidic device geometries used to generate emulsions: a) T-junction, b) co-flow and c) flow-focusing. The black and white arrows signify the flow directions of the continuous and dispersed phases, respectively.

droplet size and distribution as well as morphology. Different device geometries have been explored to generate multi-emulsions in microchannels. They include T-junctions, co-flowing devices and flow-focusing devices as illustrated in Figure 2.4. They offer control over the emulsion morphology whilst maintaining the monodisperse qualities associated with microfluidic devices.

In a simple co-flow system Figure 2.4(b) where the "droplet phase" is fed into the continuous phase through a nozzle, a viscous drag force is applied by the continuous phase and detaches the droplet from the nozzle by overcoming

the capillary force. This viscous drag force scales linearly with the droplet diameter. A critical radius R_c at which the droplets form can be determined from a balance of the viscous drag force and the capillary force as in Equation 2.4 (Seemann et al. 2011).

$$\underbrace{6\pi R_c \eta u_2}_{\text{viscous drag}} = \underbrace{2\pi r \gamma}_{\text{capillary force}} \tag{2.4}$$

Where r is the radius of the injector nozzle, η is the effective viscosity of the liquid, u_2 is the velocity of the continuous phase and γ is the interfacial tension. As the droplet grows and nears the critical radius, a thin neck develops between the droplet and the nozzle and starts to elongate and narrow due to the flow of the continuous phase, eventually this thinning is driven by the capillary force due to an energetic instability. The droplet ruptures from the nozzle and may produce satellite droplets in the process.

In a flow-focusing geometry, the streams are forced through a small orifice and generate smaller droplets compared to a co-flow geometry of the same dimensions. The smaller droplet size is brought about by the large flow rates as the fluids pass through the orifice. By varying the flow conditions, flow-focusing devices allow for the variation of the "effective geometry" of the device and thus allows for greater control of the droplet size. In a flow-focusing device pinch-off arises by action of the continuous phase flow when the droplet phase obstructs the entrance to the orifice thus droplet size can also be manipulated by choice of the collector capillary orifice diameter unlike with the co-flow geometry.

In addition to viscous drag and capillary forces, droplet formation in

Table 2.2: Non-dimensional numbers for the characterisation of dominant forces in microfluidic droplet generation.

Name (Symbol)	Formula	Physical interpretation	Typical values in microfluidic systems
Reynolds number (Re)	$Re = \frac{\rho u L}{\mu}$	Inertial force/viscous force	$10^{-6} - 10$
Capillary number (Ca)	$Ca = \frac{\mu u}{\gamma}$	Viscous force/interfacial tension	$10^{-3} - 10$
Weber number (We)	$We = \frac{\rho u^2 L}{\gamma}$	Inertial forces/interfacial tension	< 1
Bond number (Bo)	$Bo = \frac{\Delta \rho g L^2}{\gamma}$	Buoyancy/interfacial tension	$\ll 1$

microfluidic devices can also be governed by inertial forces and gravity (Zhu & Wang 2017). The dominance of each of these four types of forces on the droplet formation processes can be conveniently represented by a set of non-dimensional numbers as shown in Table 2.2.

2.3.1 Droplet formation modes

There are generally two distinct regimes of droplet formation, dripping and jetting, which are determined by the flow conditions. Droplet break-up in both the dripping and jetting regimes is a result of detachment of the droplet phase induced by the interfacial tension and viscous drag of the continuous phase (Chen et al. 2015). Droplet production in dripping mode occurs at low flowrates and results in highly mono-disperse emulsion droplets that form

close to the collector capillary orifice. On the other hand, droplets produced in the jetting mode form farther away from the orifice and have higher polydispersity. The mono-dispersity of the droplets in microfluidics operating in dripping mode arises due to the fact that the break-up of the unstable filament connecting the droplet with the nozzle is governed by a single mode of deformation (Seemann et al. 2011). Erb et al. (2011) developed an analytical expression from a force balance of viscous and interfacial forces to predict the droplet size in the dripping mode which coincided with a range of experimental data using a variety of fluids. They proposed that droplet rupture occurs above a critical capillary number ($Ca = 0.1$) which showed good agreement with experimental data. Increasing the flowrate of the continuous phase leads to an extension and narrowing of a continuous jet of the inner fluid which breaks up farther away from the nozzle. Breakup of this cylindrical jet can be described according to the Rayleigh-Plateau instability and is susceptible to different unstable modes leading to the observed reduction in mono-dispersity of the droplets produced (Seemann et al. 2011). However, Guillot et al. (2007) have shown that these unstable modes can be confined by the correct choice of channel diameter leading to the formation of a stable jet that runs along the length of the channel. Kim et al. (2015) used this method to form ultrathin microcapsules in a flow-focusing device. Microcapsules with an ultrathin shell have a lowered mass transfer resistance through the shell which is important in situations where mass transfer through the shell is the rate limiting step.

At low Reynold's numbers (less than 100), the transition from dripping to jetting in co-flowing devices can be attained by either increasing the flowrate

of the continuous phase whilst keeping the flowrate of the dispersed phase constant or vice versa. The transition in the first case is governed by a balance between viscous and interfacial forces and is described by a critical capillary number (Ca_{crit}). However, in the latter case, the transition is dependent on inertial forces with respect to interfacial forces and is thus described by a critical Weber number (We_{crit}) (Utada et al. 2007). Thus, for any immiscible fluid combinations, the production of monodisperse emulsion droplets can be ensured by maintaining the flow conditions below the critical We_{crit} and Ca_{crit} values where dripping is predicted.

2.3.2 Double emulsion formation

In double emulsion formation there are two droplet formation events, the core droplet, encapsulated by the shell droplet. Independent adjustment of the flow conditions of each stream means the dripping and jetting regimes of either stream can be matched or decoupled depending on the desired morphology of the final emulsion droplet. The optimal conditions for the formation of a uniform core-shell structure include the coupling of the dripping regimes of the core and shell phases. Utada et al. (2007) showed that dripping to jetting occurs when both the Capillary and Weber numbers are small or their sum is approximately equal to one. Increasing either will lead to jetting by domination of either the viscous or inertial forces signified by a narrowing or widening jet, respectively. They described six flow conditions leading to different microcapsule structures depending on whether the middle fluid was experiencing extended jetting, shortened jetting or dripping and whether the

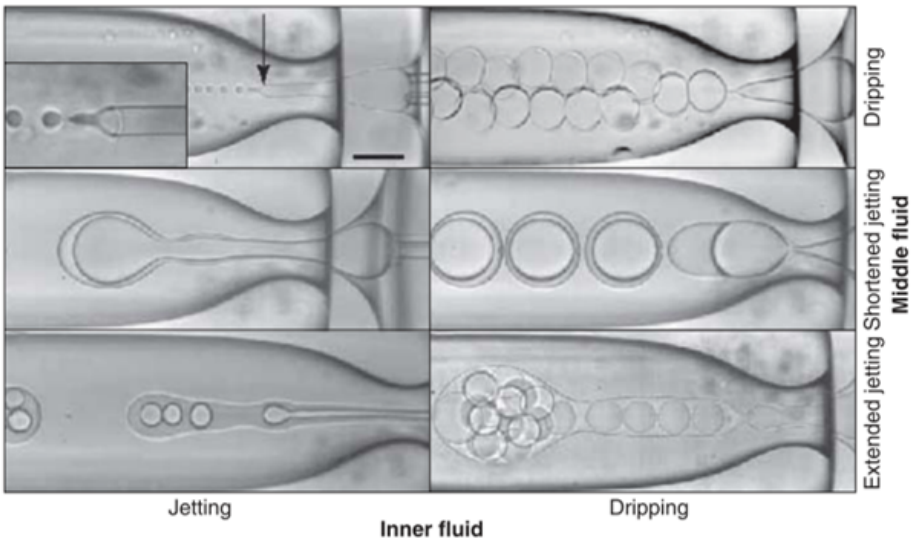

Figure 2.5: Dripping and jetting regimes leading to various droplet morphologies of emulsions produced by Utada et al. (2007) in a microfluidic device. Scale bar represents 200 μm and applies to all images.

inner fluid was jetting or dripping. Figure 2.5 shows the different regimes possible.

Chen et al. (2015) studied the effects of the ratios of the viscosities, flow rates and interfacial tensions of the three phases in a flow focusing device on the double emulsion formation using a computational fluid dynamics (CFD) simulation. They found that dripping was the predominant droplet formation mechanism for the case that the middle phase is less viscous than the continuous phase. Furthermore, it was shown that in the dripping mode the viscosity has little effect on the droplet size as the dominating factor is the interfacial tension.

For the cases where the middle phase is more viscous, jetting is the predominant droplet formation mode as the higher viscosity has a stabilising effect (viscous damping) on the thin interface resulting in larger droplets

(Chen et al. 2015). Zhou et al. (2006) showed that when the viscosity of the inner fluid is greater than that of the outer fluid, or the inner fluid has an excessively low capillary number, the middle fluid breaks before the inner fluid and thus the shell ruptures and encapsulation is unsuccessful. This sets a constraint on the choice of inner and middle phase combinations for a given set of flow conditions. In the other extreme, where the viscosity of the middle fluid is much greater than the viscosity of the continuous phase, a jet is formed and pinch-off by the continuous phase is reduced resulting in rupture and loss of the inner phase, setting another boundary in the choice of fluid combinations and flow rates.

For cases where the interfacial tension on the inner interface is greater than that on the external interface, a spherical internal droplet is formed before the middle fluid is pinched off by the outer fluid. The more flexible outer interface is easily deformable by viscous drag leading to a non-uniform distribution of the middle fluid. For the cases where the interfacial tension on the outer interface is greater than that of the inner interface, a long filament of the inner and middle fluids can be observed during droplet formation before both fluids break, to form a droplet (Chen et al. 2015). In this case, the internal interface is more deformable.

The flow conditions and fluid properties characterised by non-dimensional numbers such as the Weber and Capillary numbers control all aspects of the resulting emulsion droplet size and morphology. As these emulsion drops are precursors for the final microcapsule product, a particularly important property to control in core-shell double emulsions is the middle phase thickness. This forms the dense shell in polymer core-shell microcapsules and

dictates the microcapsule strength as well as heat and mass transfer properties. For sorption applications, the semi-permeable shell presents a mass transfer resistance that must be minimised by reducing the shell thickness whilst maintaining microcapsule strength. The middle phase thickness in microfluidics is governed by the flow ratio of the middle and inner fluids and, from a mass balance, the diameter of the inner fluid (and middle phase thickness) can be determined from the emulsion diameter considering a mass balance of the flows (Nabavi et al. 2017).

2.3.3 Microfluidic device fabrication

The most commonly used method for the fabrication of microfluidics is by soft lithography through the use of poly(dimethylsiloxane) (PDMS) in replica moulding. The flexible nature of PDMS means that channel geometry is not precise and may deform under high pressure flow conditions. PDMS can also suffer from swelling and other issues related to material incompatibility such as dissolution or diffusion. However, many methods have been developed to coat PDMS surfaces to counter these effects such as with silica via a sol-gel process (Aymerich et al. 2016). Fabrication of the device usually involves the production of masters by contact photolithography from which a replica is made with PDMS. This replica mould is then bonded to a glass cover and tubing connected directly by piercing the PDMS with the tubing. This fabrication method lends itself to much flexibility and an array of complex channel structures can be produced. Alternative device fabrication materials with lower permeability compared with PDMS include photocurable thiol-

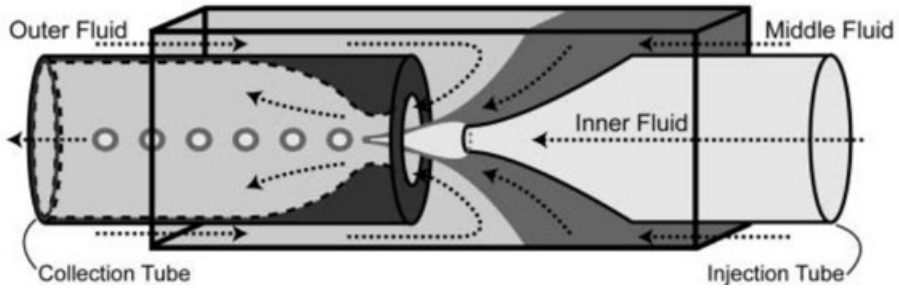

Figure 2.6: Capillary alignment technique using a square capillary with nested round capillaries of a similar outer diamter to the internal square height. Adapted from Utada et al. (2005)

ene resins (Sticker et al. 2020). This can be achieved using the same master as with the PDMS method or recently, by 3D printing. However, there is still a limit in 3D printer resolution with regards to channel sizes for typical microfluidic devices.

Glass has good solvent resistance and high transparency which makes it suitable for microfluidic applications that use especially harsh solvents or are combined with photopolymerization of the generated emulsions to form microcapsules. Methods for producing glass microfluidics include dry and wet etching, machining (Wang et al. 2018), laser ablation (Wlodarczyk et al. 2019) and glass capillary assembly (Amato et al. 2017). Glass capillary assembly is a simple method to produce glass microfluidics through the alignment of concentric glass capillaries as shown in Figure 2.6. Alignment of injector and collector capillaries is attained by inserting round tapered capillaries in a square capillary of fractionally larger internal width than the injector and collector capillaries.

Tapered glass capillaries are produced by pulling a heated glass capillary in a pipette puller where the glass necks and elongates until it breaks to form

a sharp point. The tip is then enlarged to the required diameter by sanding it down to the desired size. This is a prolonged and laborious process with low reproducibility. A faster method was developed by Wei et al. (2019) using hydrofluoric acid (HF) to etch the pulled capillaries to the desired diameter, however, safety concerns with the use of HF affect the practicality of the technique. Epoxy resin is used to bond all the compartments together, including the tubing. This fixes the device geometry, however, some adjustable devices have been developed in cases where flexibility of the geometry is required (Bandulasena et al. (2019) and Zhu & Wang (2017)).

Wettability of microfluidic channels

The stability of droplet production in microfluidic devices is dependent on the wettability of the microchannels. For oil-in-water emulsions, hydrophobic walls are required and for water-in-oil emulsions, hydrophilic walls are required. This prevents rupturing of the emulsion droplet on contact with the microfluidic channel walls. Consequently, for double emulsions, regions of hydrophilic and hydrophobic wettability are required in the same device (Okushima et al. (2004) and Abate et al. (2008)). For example, for an o/w/o double emulsion, the walls of the injector and collector capillary would be modified to be hydrophilic and hydrophobic, respectively. The surface wettability of the channel walls can be manipulated by methods which include silane coatings, surface photopolymerization, laminar flow patterning and initiated chemical vapour deposition (Thompson et al. 2016). The modular nature of glass capillary microfluidics allows for a simpler process of surface modification of the different regions for double emulsion generation compared

with PDMS microfluidics made from a single master. For example, Amato et al. (2017)) formed water-in-oil-in-water (w/o/w) double emulsion in a flow focusing device where the injector and collector capillary surface were modified to be hydrophobic and hydrophilic, respectively, prior to device assembly by use of silanes.

2.3.4 Microcapsule formation in microfluidic devices

Upon generation of the emulsion of the final microcapsule product, formation of the solid particle is achieved using techniques similar to those summarised in Table 2.1. The shell formation scheme chosen depends on the chemicals used and the desired morphological and material properties of the final microparticle product. For on-the-fly microcapsule formation, a rapid reaction immediately after an emulsion drop is generated reduces the risk of blockages in the microfluidic channel due to reactants sticking to the walls or coalescence of droplets leading to agglomerates. Alternatively, the produced emulsion droplets can be collected and cured in a separate step.

In the class of physical methods (Table 2.1), solvent evaporation/extraction has been employed in conjunction with microfluidics for the formation of structured microcapsules. For example, Watanabe et al. (2014) used solvent extraction in microfluidics to form polymer microcapsules (sodium poly (styrenesulfonate)) with a smooth surface and porous interior. The microparticle precursor was an aqueous solution of the polymer dispersed in hexadecane at a T-junction followed by extraction of the water induced by contacting with methyl ethyl ketone to form the solid particles. A schematic of

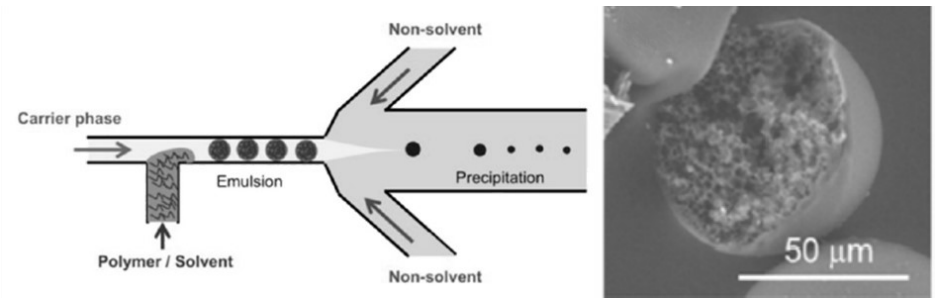

Figure 2.7: Left: schematic of microfluidic assembly showing generation of emulsion of polymer solution at a T-junction followed exposure to non-solvent in a downstream precipitation step. Right: Resulting microcapsule showing smooth surface and porous interior (Soppimath et al. 2001).

the formation process and an SEM micrograph of the resulting microcapsule are shown in Figure 2.7. In an earlier but similar work, Soppimath et al. (2001) prepared cellulose acetate matrix-type microcapsules with ibuprofen to demonstrate its slow-release properties in pharmaceutical applications. The polymer was dissolved in a solution of acetone and dichloromethane and dispersed in water using microfluidics. Solvent evaporation was then used to extract the solvents to form a polymer matrix with an imbedded drug. The solidification process is dependent on several factors which include the solubility and diffusivity of the different components and their concentration as well as surfactants and temperature. The drawbacks of these techniques are in the use of harsh solvents and the complexity of solvent and polymer selection.

Under the class of chemical methods (Table 2.1), the reactions in other heterogenous polymerization methods (suspension polymerization, emulsion polymerization, etc.) can equally be applied to emulsions generated by microfluidics. Both chain growth and step-growth polymerization reactions can

be used in these heterogeneous systems. In contrast to the solvent evaporation/extraction methods, the form of the emulsion template is preserved in the resulting microcapsule with these methods. Thus, a w/o/w double emulsion will form true core-shell microcapsule.

A set of step-growth reactions that have shown increasing popularity in microfluidic systems are the thiol-Michael and radical mediated thiol-ene/yne "click" reactions. As the term "click" reactions indicate, they occur under fairly mild reaction conditions, have rapid kinetics, high yields, limited by-products and lend themselves to modularity (Hoyle & Bowman 2010). This modularity and tunability make this a powerful system for developing novel and tailored encapsulation systems for existing and yet-to-be-discovered applications. Examples include the shell material for the encapsulated CO_2 solvents developed by Stolaroff et al. (2016) (Section 2.1) where thiol and vinyl functionality was grafted onto PDMS copolymers which ensured compatibility between the amine core and shell as well as high CO_2 permeability.

The radical mediated mechanism begins by generation of a radical from the initiator (photo-, redox or thermal initiator) with the appropriate trigger. The radical abstracts the hydrogen from the thiol to generate a thiol-centred radical which generates a carbon-centred radical by adding across a C=C bond followed by chain transfer to a new thiol. The process of addition and chain transfer continues until termination (Amato et al. 2017). The nucleophile-catalysed anionic mechanism involves generation of a thiolate by proton abstraction from the thiol by a base which subsequently produces a carbon-centred anion by adding across an electrophilic C=C bond. The resulting anion can abstract a proton from the conjugate acid or from an-

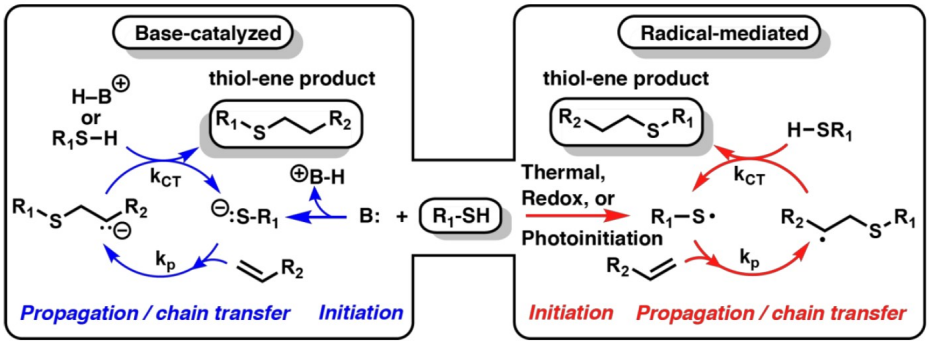

Figure 2.8: Base-catalysed (thiol-Michael) addiition (left) and radical-mediated thiol-ene addition (right). Adapted from the work of Amato (2018).

other thiol to regenerate the base or the thiolate, respectively (Amato 2018). Whether the reaction occurs via the UV-initiated free-radical mechanism or the nucleophile-catalysed anionic mechanism (catalysed thiol Michael addition) is governed by the electronic nature of the C=C group (Kwisnek 2011). The reaction scheme is shown in Figure 2.8.

The photo-initiated polymerization (photopolymerization) route works well in microfluidic systems as the reaction can be carried out in-situ by exposure to light at an appropriate wavelength. This is a simple process to perform at lab-scale compared with temperature-initiated or redox initiated systems. Acrylate photopolymerization systems enjoy much ubiquity but suffer from oxygen inhibition and shrinkage arising from the chain-growth polymerisation that these systems undergo (Kwisnek 2011). In contrast, thiol-ene photopolymerization reactions are insensitive to oxygen which simplifies the emulsion preparation process as the photopolymers do not require degassing (Nair et al. 2010).

Multifunctional thiols and alkenes react to form polythioether networks with a range of chemical and mechanical properties that are dependent on the

identities of the monomer precursors. Gelation at high conversions during the photopolymerization of thiol-ene photopolymers gives them the advantages of low shrinkage, homogeneous network density and narrow glass transitions compared with acylate-based photopolymers (Hoyle & Bowman 2010). Selection of the monomers allows for the formation of dense networks that can be used as gas barrier membranes in packaging (Kwisnek et al. 2009), CO_2 gas separation membranes (Kwisnek et al. 2014) as well as hydrophilic, water permeable hydrogels with controllable degradation at specific pH for the release of specific active ingredients (Rydholm et al. 2005). Additionally, thiol-ene crosslinking can be used to improve the properties of conventional materials as in the work of Sierke & Ellis (2019) where poly(vinylidene difluoride) (PVDF) water filtration membranes were strengthened against compaction by cross-linking with a thiol-modified silsesquioxane. Resistance to compaction as quantified by an increase in the Young's modulus of 49% was achieved with the addition of 10% silsesquioxane without excessive flux reduction. In a similar work, Fei et al. (2017) formulated crosslinked polyacrylonitrile (PAN) membranes under benign thiol-ene reaction conditions to enhance their resistance to fouling. Thus for applications where membranes made from conventional thiol and alkene monomers are not suitable, chemical modification can be utilised so materials can be formed rapidly and under milder, more sustainable conditions.

2.4 Characterisation of microcapsule mechanical properties

A requirement of a good microencapsulation system is to be able to retain its contents often under an applied stress either internally or externally. Internal pressures can arise from osmotic stresses (Zhang et al. 2019) or gas generation (Paret et al. 2015) and external stresses can arise from shear flows (Finken et al. 2011) or rubbing as is the case with fabric enhancing microcapsules (Liu 2010). The Young's modulus which indicates the ability of a capsules to withstand deformations and its rupture strength, associated with a capsules ability to retain its contents are important parameters for the characterisation of microcapsule mechanical properties.

Techniques employing atomic force microscopy (AFM), micropipette aspiration, texture analyser and osmotic stresses have been employed in the study of the mechanical properties of microcapsules (Mercadé-Prieto & Zhang 2012). However, limitations discussed in greater detail by Liu (2010), such as high sensitivity to surface inhomogeneities, complex force calibration and microcapsules size limitations have led to the development of the micromanipulation technique (Zhang et al. 1991). In this technique, single microcapsules are compressed between two parallel surfaces allowing for the direct measurement of the deformation behaviour, rupture strength as well as the estimation of the Young's modulus from analytical or finite element models.

2.4.1 Micromanipulation

The mechanical strength of three types of microcapsules consisting of different shell materials were compared by Sun & Zhang (2002) using the micromanipulation technique. They were able to determine a clear bursting event for microcapsules with a melamine-formaldehyde and urea-formaldehyde (UF) shell but not for the gelatine microcapsules tested. Compression and decompression below the bursting force also revealed hysteretic behaviour with the MF and UF microcapsules, indicating plastic behaviour.

The rupture force of microcapsules has also been shown to be proportional to the particle diameter (Zhang et al. (1992) and Mercade-Prieto, R & Nguyen (2011)). Chan et al. (2011) studied the effect of the formulation on the mechanical properties of alginate beads by varying the alginate concentration and gelling agent. Micromanipulation measurements showed that the stiffness of the microcapsules increased with alginate and gelling agent concentration allowing for the tailoring of the formulation conditions to a particle of desired stiffness. The drawbacks of this technique are that it is slow (compression of one particle at a time), the resolution is limited to force transducer resolution and the scatter in data due to variation in the microparticle structure. In addition, the contact area between the probe and particle is often not known and nominal values have to be used unless values are calculated directly based on theoretical methods or images of the deformation process taken.

2.4.2 Theoretical models of microsphere and microcapsules deformation

Intrinsic mechanical properties such as the Young's modulus of solid elastic spheres and fluid-filled membrane shells cannot be directly inferred from the force – displacement profiles (Liu 2010). Common theoretical models employed in the deformation of solid elastic spheres include the Hertz and Tatara theories, for cases where auto-adhesive effects are negligible (Liu et al. 1998). For fluid-filled membrane shells, theoretical models include the shell model (Taber 1982) and membrane model by Feng & Yang (1973) later extended by Lardner & Pujara (1980). Identification of applicable theories for the deformation of elastic spheres and fluid-filled membrane shells rests on the assessment of the loading/unloading curves of these structures as well as their geometry of deformation (Liu 1995).

The Hertz theory describes the deformation of spheres at small strains in the elastic regime. The nominal strains are restricted to less than 10% and it is assumed that the surfaces of the bodies in contact are continuous and non-conforming. The bodies are also assumed to be linearly elastic materials on to which only normal compressive forces are transferred due to the prescribed condition of frictionless contact surfaces. An applied compressive force F_c, on a particle of diameter D between two parallel plates resulting in a relative displacement δ between the plates can thus be related according to Equation 2.5, the Hertz model.

$$F_c = \frac{E\sqrt{D}}{3(1-\nu^2)}\delta^{\frac{3}{2}} \tag{2.5}$$

where E is the Young's modulus and ν is the Poisson's ratio of the material, usually assumed to be equal to 0.5.

For nominal strains greater than 10% but less than 60%, the Tatara model was developed which also accounts for the non-linear elastic behaviour observed at large strains via a strain-dependant Young's modulus (Tatara 1993). The Tatara model consists of a set of equations requiring a numerical solution, however, a semi-empirical simplification of the Tatara model, Equation 2.6, has been applied previously for the estimation of the Young's modulus assuming linear elasticity (Yan et al. 2009).

$$F_c = \frac{E\sqrt{D}}{3(1-\nu^2)}\delta^{\frac{3}{2}} + c_1\delta^3 + c_2\delta^5 \tag{2.6}$$

where c_1 and c_2 are arbitrary constants. Equation 2.6, though empirical, captures the third and fifth power correlations of the displacement with the applied compressive force that is often observed at higher strains of deformed elastic spheres.

The Hertz and Tatara models have been used to describe the mechanical behaviour of several microcapsules. Both the Hertz and Tatara models consider a homogeneous spherical object thus using such models to estimate the mechanical properties of the shell in microcapsules only gives information about the behaviour of the overall composite capsule. For deformations of microcapsules with shell thickness ratios in the range 0.4 to 12%, Mercade-Prieto, R & Nguyen (2011) presented a simplified method to estimate the

elastic properties of the shell material as well as an estimation of the shell thickness based on FEM results for deformations in the range 0.03 to 0.1. The Young's modulus of a microcapsule may be affected by the degree of swelling of the capsules and indeed the concentration of components of the core.

For fluid-filled shells, the models developed by Feng & Yang (1973) and Lardner & Pujara (1980) were developed based on the assumption that the shell wall was thin enough to be treated as a membrane. This implies that the wall cannot support out-of-plane shear stresses and bending moments (Stenson et al. 2009). The liquid-filled shells are assumed to have a constant volume throughout the deformation and the liquid, incompressible. Furthermore, the shell material is assumed to be homogenous and isotropic. Finally, analysis of micromanipulation compression data requires that the selection of an appropriate stress and strain relationship (constitutive equation) be made. Two groups of governing equations derived by Lardner & Pujara (1980) can then be solved numerically which simulate the deformation profile of the compressed liquid-filled shell, given the material properties and compression displacement. A non-dimensional comparison between the analytical predictions and the compression data allow for the properties of the shell material to be estimated. Table 2.3 presents a series of investigative works that have previously applied this methodology to investigate the material properties of fluid-filled membrane entities such a mammalian and plant cells as well as the constitutive equations used.

Table 2.3: Compression testing on core-shell microparticles and strain models adopted

Reference	Particle type	Constitutive model
Liu (1995)	Tomato cells	Mooney-Rivlin
Wang et al. (2004)	Tomato cells	Cheng (1987) function
Keller & Sottos (2006)	UF microcapsules	Cheng (1987)
Tan et al. (2008)	Zebrafish embryos	Mooney-Rivlin
Stenson et al. (2009)	Yeast cells	Finite (Green) and Hencky (Logarithmic) strain

2.4.3 Microcapsule permeability and buckling

Permeability is a parameter describing the flux of a chemical species through a membrane. It is defined as the product of the solubility and diffusion coefficient of the species through a membrane (Crank 1979). The use of this parameter is generally applied in describing membrane transport assuming a solid-diffusion mechanism (Wijmans & Baker 1995). Microcapsules with permeable shell walls will inevitably change in volume under compression thus the assumption of constant volume in the compression models discussed previously does not hold. Wang et al. (2004) accounted for this volume change in their model for the compression of cultured tomato cells by calculating the microcapsule volume at each equilibrium compression step. The cell wall was assumed to have a constant hydraulic conductivity (permeability) allowing the volume change to be related to the compression distance and the internal hydrostatic pressure.

As the volume of the contents of a spherical shell are reduced, there is a linear regime before buckling where the spherical shape of the shell is preserved and the pressure difference across the shell wall ΔP is proportional

to the ratio of the volume change ΔV to the initial volume V_0. During this process the shell experiences elongational shear (provided its Poisson's ratio is nonzero) (Coupier et al. 2019). This region can be described according to Equation 2.7.

$$\Delta P = \frac{2Eh}{3(1-\nu)R}(\frac{\Delta V}{V_0}) \tag{2.7}$$

Classical buckling theory gives the critical pressure difference ΔP_c at which buckling occurs according to Equation 2.8.

$$\Delta P_c = \frac{2E}{\sqrt{3(1-\nu^2)}}(\frac{h}{R})^2 \tag{2.8}$$

where ν is the Poisson's ratio of the shell material, E is the Young's modulus, h is the shell thickness and R is the radius of the sphere (Coupier et al. 2019). After buckling, a third stage is observed described by Coupier et al. (2019) as the post-buckling plateau, where the pressure drop no longer changes with respect to the volume fraction. The plateau pressure drop ΔP_{plat} can be predicted with the Equation 2.9.

$$\Delta P_{plat} = \frac{E}{(1-\nu^2)^{0.75}}(2.34 \times 10^{-6} + 0.9(\frac{h}{R})^{2.57}) \tag{2.9}$$

Experimental results by Coupier et al. (2019) demonstrated the validity of this relationship for thickness ratios up to 0.3 whilst a Poisson's ratio of 0.5 or greater was shown to be valid if the material could withstand deformations of as much as 200% without plastic deformation or rupture.

For permeable shells, the rate of transfer of the solvent from the micro-

capsule core $\dot{n}$ is dependent on the internal capsule pressure p_{cap}, the partial vapour difference of the solvent across the shell Δp_{vap} and the permeability P_{H_2O} as described by Equation 2.10,

$$\dot{n} = \frac{P_{H_2O}}{h} a(\Delta p_{vap} - p_{cap}) \tag{2.10}$$

where h is the shell thickness and a is the microcapsule surface area (Finn et al. 2019).

2.5 Thermal energy storage

Thermal energy storage is a technology that can be applied to mitigate the differences in energy supply and demand over a range of timescales from a daily basis to a season-to-season basis. Correcting the supply and demand mismatch is particularly important towards promoting the widespread use of renewable resources such as solar energy where the energy is often generated during periods of low demand. Thermal energy storage (TES) plays an important role in this aspect, particularly in domestic applications such as space heating and cooling as well as refrigeration. Heat can be stored in the form of sensible heat as with hot water storage tanks (Wang et al. 2016); latent heat, through the use of various phase change materials (PCMs) (Hussain et al. 2020) as well as through the use of sorption thermochemical heat storage materials (Yan et al. 2016).

Sensible Heat Storage

Sensible heat storage is a cheap and readily available technology and involves heating the storage medium (usually a liquid) to a set temperature which is stored in an insulated vessel until required. The energy stored is governed by the specific heat capacity of the storage medium and the temperature rise and is thus severely limited by relatively low energy density values and challenges with insulation. Common solid storage media include rock and concrete which can be used as a thermal mass for building temperature regulation (Fan & Luo 2017). Examples of liquid sensible heat storage media include water and oils such as engine oil (Ebrahimi & Keshavarz 2015). Water is the most common liquid storage medium due to its availability and benign properties.

Latent Heat Storage

An improvement to the sensible storage system was attained through the use of PCMs in latent heat storage systems where energy is stored by melting a PCM and insulating it until required. This greatly improves the energy storage density as the specific latent heat is much greater than the specific heat capacity with the additional advantage that heat could be delivered at a fixed melting/freezing temperature. However, such systems still face challenges with insulation as well as heat and mass transport as a result of phase separation of the solid and liquid PCM as well as supercooling (Zahir et al. 2019). This has led to the development of novel heat exchanger designs and composite materials. Nano-enhanced PCMs are composites consisting of a

dispersion of nanoparticles of a high thermal conductivity material in a PCM for enhanced thermal conductivity and reduction in sub-cooling of the PCM due to the presence of nucleation sites (Leong et al. 2019). Another composite material developed for the enhancement of the heat transfer properties of PCMs is microencapsulated PCMs. In this case, the heat transfer benefits are from a kinetic approach where the surface area and surface-to-volume ratio of the PCM are increased by microencapsulation. This introduced the first real attempt in using microencapsulation in energy-related applications. New challenges were discovered with the encapsulation of PCMs requiring strong microcapsules that could resist the volume expansion/contraction related to the phase change process, possess encapsulating material of high thermal conductivity and have reduced sub-cooling. This serves to highlight the structural and material challenges imposed on microcapsules in energy applications.

Sorption Thermochemical Energy Storage

Greater energy storage densities are available with the use of thermochemical energy storage materials up to an order of magnitude greater than that of sensible heat storage (Aydin et al. 2015). This translates into a smaller footprint of energy storage systems which is particularly important for domestic applications. Thermochemical energy storage relies on the energy changes that occur during a reversible sorption reaction of the typical form $A + B \rightleftharpoons AB + energy$, where A is the sorbent, B is the sorbate (usually a vapour) and AB is the resulting product of the two. A sorbent is defined as a material that has the ability to attract and hold gases and liquids (the

sorbate) (Kalogirou & Florides 2016). The sorption reaction may be due solely to a sorption process resulting from the physisorption of the sorbate governed by van der Waals interactions and hydrogen bonding or it may be the result of chemisorption where chemical bonding is involved as in hydration reactions. The forward process involves the release of energy in the form of heat upon contact between the sorbent and sorbate. Depending on the degree of interaction and the physical form of the sorbent, a sorption system can be classified as a liquid absorption, solid absorption or a solid adsorption system. Absorption results in a physical change of the sorbent, for example, the dissolution of hygroscopic salt crystals upon exposure to water vapour whereas the bulk sorbent is unchanged in adsorption. The reversibility of the reaction means that by heating the discharged system above the equilibrium sorption temperature, the components can be separated back into sorbent and sorbate allowing the heat to be stored for an extended period in "chemical form" with negligible heat loss (Zondag 2015).

The magnitude of the heat released depends on the degree of interaction (physisorption, chemisorption, etc.). It is the sum of the heat of condensation of the vapour sorbate and the sorbent-sorbate binding energy. This binding energy is dependent on the sorbate concentration as well as the operating temperature and pressure of the system (Hauer 2007). For instance, when LiBr solution is used as the sorbent, a typical solution of $50wt\%$ LiBr is diluted by absorption of water vapour to a concentration of $38wt\%$ (N'Tsoukpoe et al. 2010) and the binding energy released in this case is the solution heat (Wu 2010) which is dependent on the solution concentration, the temperature and vapour pressure throughout the absorption cycle. A sig-

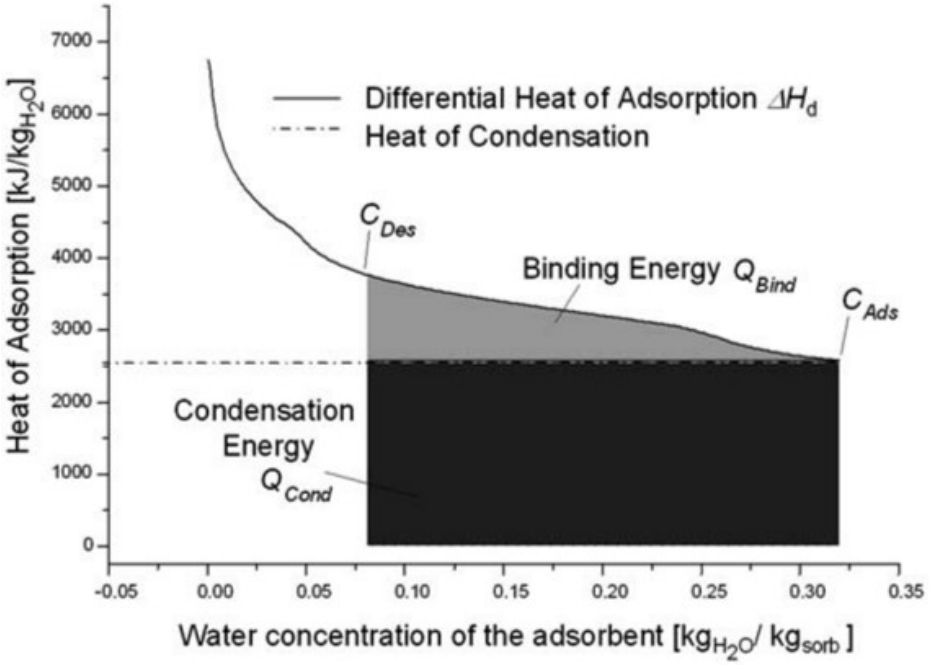

Figure 2.9: Typical curve of heat of adsorption as a function of water content for a zeolite material (Hauer 2007).

nificant fraction of the energy density associated with sorption heat storage materials is due to the heat of vaporisation of the vapour (especially in the case of solid physisorption as with zeolites) (Zondag 2015). This is often an order of magnitude larger than the heat of fusion of the same material which is why sorption heat storage systems can theoretically reach higher energy storage densities than latent heat storage systems. Figure 2.9 presents the contribution of the condensation energy and the binding energy to the heat of adsorption during water adsorption in an example zeolite system from the work of Hauer (2007). The decrease in heat of adsorption with water uptake is explained by the fact that the first layer of water molecules is bound more strongly to the surface compared with subsequent layers.

A sorbate in the vapour form also means that it is easier to separate

from the sorbent which can be stored separately for extended periods with negligible heat loss. However, sorption systems are usually more complex than sensible and latent heat storage systems and also suffer from material degradation over repeated sorption/desorption cycles.

The equilibrium composition of the forward products in the reversible reaction depends on the temperature and vapour pressure. The equilibrium temperature can be related to the vapour pressure according to the Clausius-Clapeyron in Equation 2.11,

$$T_{eq} = \frac{\Delta H}{(\Delta S - R_G \ln(\frac{p}{p_0}))} \tag{2.11}$$

where T_{eq} is the equilibrium temperature, p is the vapour pressure, p_0 is the reference pressure, R_G is the universal gas constant, ΔS is the entropy change and ΔH is the associated enthalpy change. The entropy term is largely governed by the sorbate and the enthalpy term is largely dependent on the sorbent and reflects the nature of the bonding interaction between sorbent and sorbate (Zondag 2015) . Sorption equilibrium data are a useful tool in the assessment of the suitability of a particular sorbent-sorbate pair to a particular application. These are often determined experimentally over a range of temperatures and vapour pressures.

System Classification

Thermochemical heat storage systems can be classified depending on whether they are isolated from the environment as in closed systems or exposed to the external environment as in open systems. In a closed system the sorbate

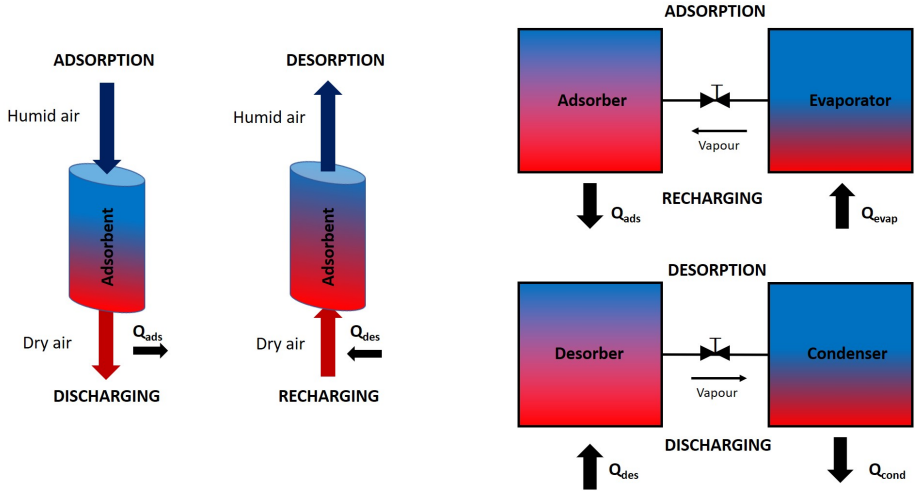

Figure 2.10: Schematic of adsorption and desorption cycles in open (left) and closed (right) sorption systems.

is stored in a separate vessel, usually as a condensed liquid to reduce the occupied volume and also with the possibility of using the condensation energy (Frazzica & Freni 2017). In open systems the sorbate is exchanged with the environment and is thus restricted to water vapour unlike with closed systems where other working fluids such as ammonia and ethanol can be used. Figure 2.10 is a schematic showing the working principles of the two systems.

Closed systems are usually operated in vacuum conditions which allows for a low temperature heat source to recharge the system. The evaporated sorbate is then condensed and stored as shown in Figure 2.10. The heat of condensation Q_{cond} can be further utilised or expelled to the environment. When heating is required, water vapour generated in the evaporator is allowed to contact the absorption bed in the reactor to release heat. This cycle can also be used for cooling and refrigeration, with the environment to be cooled acting as the low-temperature heat source. Indeed, there is an overlap

of sorption materials for thermal energy storage and heat pumps/refrigerators and similar material-related issues arise in both systems as summarised by Cabeza et al. (2017). For the same sorbent material, it is therefore important to consider that the reaction temperatures will be different depending on the system when selecting materials. Open systems operate at ambient conditions and the condensation energy is not utilised during the discharging process in contrast to closed systems where condensation of the vapour adds a significant energy contribution to the heat released (Vasta et al. 2018). The energy storage capacity of open systems depends on the moisture available at ambient conditions thus, sorbent material with a high water-uptake is particularly desirable for application in such systems. Additionally, sorbent materials with a large uptake over a narrow range of the relative vapour pressure and temperature are the most promising for adsorption thermal energy storage (Aristov 2007*b*).

2.5.1 Materials for thermochemical energy storage

TCMs are generally classified according to the reactions which govern their sorption process, namely, adsorption, absorption and chemical reactions (Solé et al. 2015). Adsorption is defined as a surface process where molecular transfer from a bulk fluid to a solid surface occurs as a result of physical (van der Waals forces or hydrogen bonding) or chemical bonds (Artioli 2008). As it is a surface process, its effect is maximised by large surface areas. Absorption involves the incorporation of a fluid into a bulk solid or liquid to form a solution. Finally, the chemical reactions in relation to TCMs refers to

reversible chemical reactions such as those involving salt hydrates and water, where the sorbate is incorporated into the hydrate crystal structure without dissolution. However, these salts are often also hygroscopic and have a high affinity for water vapour sorption (Van Campen et al. 1983) which makes avoiding dissolution a challenge. Figure 2.11 presents a categorization of some example sorption pairs according to sorbent form and interaction as presented by Jarimi et al. (2018). A fourth category for composite materials is presented and consists of hygroscopic salts imbedded in a porous host material and thus the sorption behaviour is an amalgamation of that of the porous host material (physisorption) and the salt hydrate (chemisorption).

The properties of a suitable material for sorption heat storage as specified by Jarimi et al. (2018) and Casey et al. (2014) are as follows:

- Low recharging temperature ($< 150°C$)
- High surface area and good mechanical strength
- High energy storage density
- Suitable heat and mass transfer properties for intended application
- Non-toxic
- Good thermal and cycling stability
- Low cost

The low recharging temperature limit of $150°C$ corresponds to the maximum temperature that can be delivered by a solar collector. This is particularly important as the efficiency of sorption TES systems in energy storage

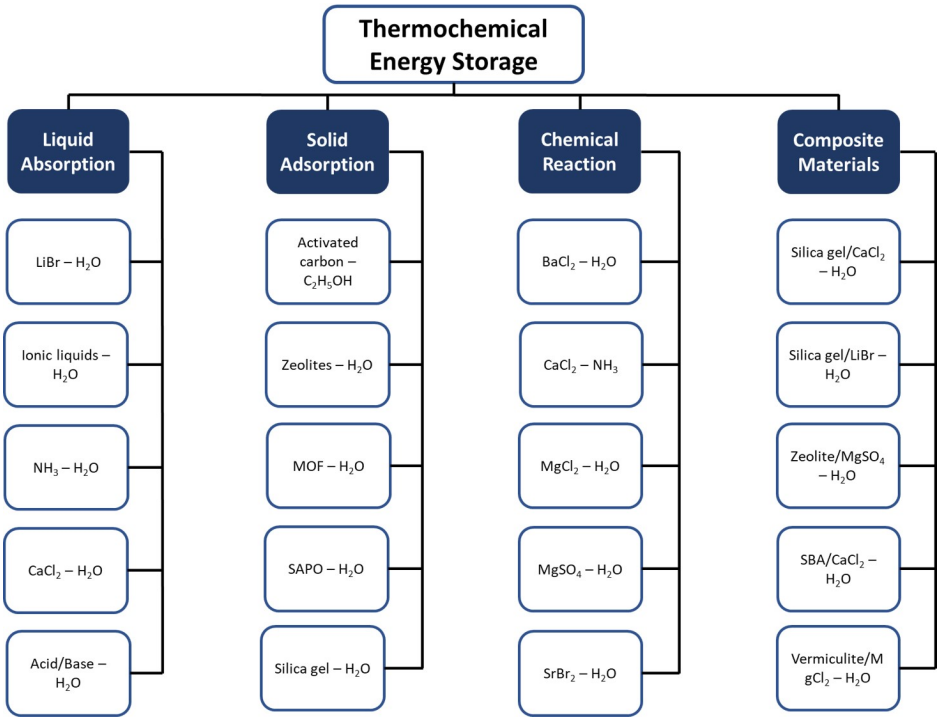

Figure 2.11: Classification of thermochemical materials adapted from Jarimi et al. (2018).

relies on the availability of a "free" heat source such as solar or waste heat to recharge the material (N'Tsoukpoe et al. 2014). The energy density depends on the sample size, reactor configuration, characterisation technique as well as the operating conditions (Solé et al. 2015). This presents a challenge in comparing similar works as there is no standardised approach to determining the material properties. For example, in closed systems, heat transfer is rate limiting and benefits most from improvements in the thermal conductivity whereas open systems are limited by mass transfer which directly affects the hydration rate (Cabeza et al. 2017).

Liquid absorption

One of the most common liquid absorption systems based on a hygroscopic salt solution is the $LiBr$/water system originally used in absorption refrigeration systems. This working pair alongside the ammonia/water working pair have been the most heavily utilized in refrigeration applications due to their favourable thermodynamics (working temperatures). $LiBr$ solution has a low vapour pressure and water vapour is absorbed by the concentrated solution to release heat. This system has been proposed for energy storage and N'Tsoukpoe et al. (2010) showed that the energy storage potential of such a system can be enhanced by the formation of salt crystals by concentration of the salt solution beyond the crystallisation point during charging. Hui et al. (2011) determined the storage capacity of seven absorption working pairs for use in domestic heating applications. The model results showed that crystallisation improved the energy storage capacity for all systems. They found the best performing working pair to be KOH/water based on cost and energy

storage capacity (2.618 $MJ\ kg^{-1}$, 95% energy efficiency), however, corrosion and safety considerations may prevent the practical implementation of such a system. Furthermore, as solutions require pumping in such systems, blockages due to crystallisation can lead to severe disruptions. This has motivated investigations into the use of ionic liquids (ILs) as liquid absorbents in energy storage applications. Ionic liquids are defined as salts composed of organic cations and either organic or inorganic anions (Narayanan et al. 2015). They are usually liquid below $100°C$ and have low vapour pressures. Wu et al. (2019) identified seven ILs for potential application as liquid absorbents for energy storage with water vapour as the absorbate. They found comparable energy storage density between the $LiBr$/water system (67.1 $kW\ h\ m^3$) and the [EMIM][Ac] IL at 67.7 $kW\ h\ m^3$ whilst avoiding crystallisation which limit the operating conditions of salt-based absorption systems.

Solid adsorption

Materials in this category are physisorption materials with high porosity and large surface areas for adsorption. Common examples include silica gels and zeolites which have amorphous and ordered porosity, respectively.

Silica gels are a low-cost adsorption material with low regeneration temperature requirements. They are formed by the sol-gel process (Schraml-Marth et al. 1992) with controllable porosity in the micro and meso range. However, this material has a relatively low heat storage capacity. Its tunable porosity has made it a suitable host matrix candidate in the preparation of composite sorbents.

Zeolites are a class of crystalline alumino-silicates with high specific sur-

face area and high microporosity (Vasta et al. 2018). Their hydrophilic nature makes them highly suitable for water sorption with typically higher discharge temperatures than silica gels. However, the common types of zeolites require high regeneration temperatures (above $150°C$) which limits their use to high temperature processes such as waste heat recovery. Development of zeolite-type materials such as aluminophosphates (AIPOs) and silico-aluminophosphates (SAPOs) promises the characteristic high absorption capacity of zeolites at low regeneration temperatures (Ristić et al. 2012). Other promising materials include metal organic frameworks (MOFs). These are adsorbent materials with very high specific surface areas composed of metal ions interconnected by organic macro-molecules. They currently suffer from poor hydrothermal stability and prohibitive costs.

Composite sorbents

Composite sorbent materials are formed by incorporating a selected salt into a porous host matrix. The salt interacts with the water vapour in the matrix sorbent to form crystalline hydrates or an aqueous solution depending on the psychrometric conditions. Preparation of composite sorbents involves drying the host matrix to remove absorbed water, salt is then incorporated into the dried matrix by filling the porous structure with a salt solution. This is achieved by soaking the porous material in the salt solution over several hours in order to allow the salt solution to penetrate the internal pores of the host material. The material is then filtered and dried resulting in the formation of salt crystals within the pore network of the matrix material. Selection of the right combination of host matrix and impregnated salt allows

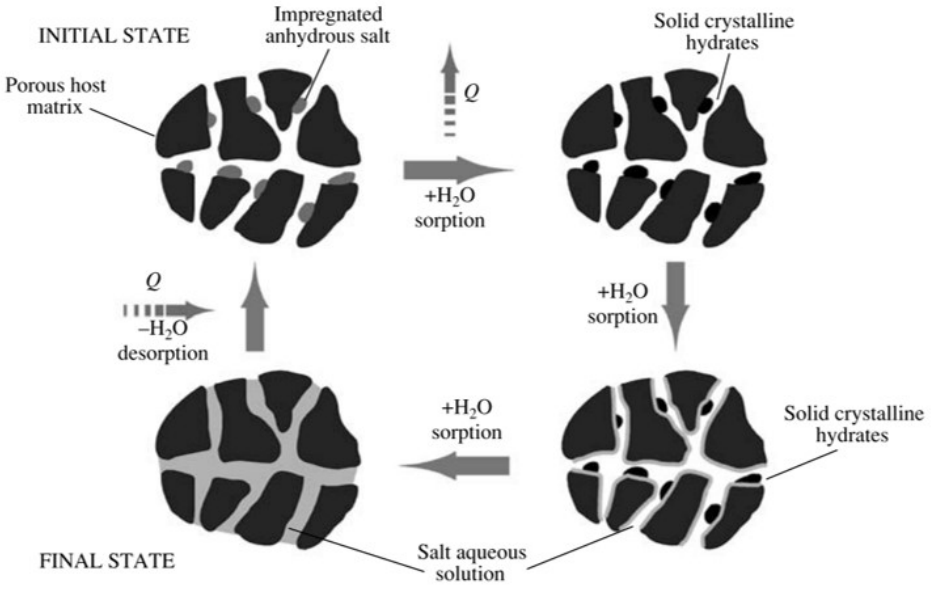

Figure 2.12: Schematic of the function of a composite sorbent as developed by Aristov (2007*a*).

for a targeted approach to composite development for a particular application (Aristov 2007*b*). A schematic of the function of the composite in an adsortpion cycle is shown in Figure 2.12 (Aristov 2007*a*).

The host matrix contributes to the overall sorption of the composite, it enhances the thermal conductivity of the salt and also retains any salt solution formed by deliquescence provided the material does not overhydrate to a point where the volume of absorbed water vapour exceeds the pore volume of the composite. The structure of the resulting composite depends on the interaction between the host matrix and the salt. For example, Jarimi et al. (2018) showed contrasting behaviour between $CaCl_2$ and $LiCl$ with vermiculite as a host material where $CaCl_2$ formed inter-lamellae crystals whereas the $LiCl$ was incorporated into the lamellae reducing their structural integrity. Addition of the salt into the pores results in a reduction in

the specific surface area and pore volume (Brancato, Vincenza et al. 2018). Impregnation of a salt into a porous host matrix can result in reduced sorption kinetics as evidenced by the work of Dawoud & Aristov (2003) where impregnation of silica gel and alumina resulted in increased water uptake relative to the unmodified host matrix but reduced uptake rate. The presence of the salt increases the equilibrium water loading relative to the bare porous matrix at a specific vapour pressure due to the combined chemisorption and physisorption processes. Dawoud & Aristov (2003) proposed two possible explanations for the reduction in kinetics: an increase in activation energy of desorption of sorbate molecules in the porous matrix wall due to the presence of the hygroscopic salt; or the formation of a solution film at the external pore openings creating a resistance to the diffusive flux towards the matrix interior, later termed the "blocking effect" by Gordeeva & Aristov (2011). Another composite based on silica-gel was developed by Courbon et al. (2017) with $SrBr_2$ as the imbedded salt with a high energy storage density of 203 $kWh\ m^{-3}$. This salt was identified in a broad study by N'Tsoukpoe et al. (2014) as having the most suitable properties for domestic heating applications with the requirement of a 60°C discharging temperature and charging temperature of 105°C. Table 2.4 summarises the properties of the most widely investigated matrix materials in thermochemical heat storage applications (Aydin et al. 2015).

Composite sorbents formed in this way suffer from the following issues: swelling as result of water uptake results in the reduction of structural integrity of the matrix; agglomeration and deliquescence as a result of overhydration during sorption cycling. Brancato et al. (2018) developed a composite

Table 2.4: Properties of a selection of host matrix materials under investigation in the scientific literature (Aydin et al. 2015).

Matrix material	Specific surface area $[m^2\ g^{-1}]$	Pore volume $[cm^3\ g^{-1}]$	Bulk density $[kg\ m^{-3}]$	Specific heat capacity $[kJkg^{-1}K^{-1}]$	Thermal conductivity $[kWm^{-1}K^{-1}]$
Vermiculite	8 – 10	2.8	64 - 160	0.84 - 1.08	0.064
Silica gel	750 - 850	1	480 - 720	1.13	0.174
Zeolite	550 - 600	0.17	1000 - 1120	1.08	0.07
Activated carbon	1500 - 1700	2	2000 - 2100	1.06	0.15 - 0.5
Expanded natural graphite	18 - 22	0.073	1200 - 1500	0.7	6 - 8
Activated alumina	150 - 300	44	750 - 1000	1	1.4 - 2.5

of a water-vapour permeable silicone foam with $MgSO_4 \cdot 7H_2O$ for sorption TES that could accommodate swelling of the composite due to the elasticity of the silicone.

2.5.2 Characterisation of composite thermochemical materials

The most common thermal analysis technique for measurement of the properties of TCM materials is the coupled thermogravimetry and differential scanning calorimetry (TG-DSC) technique. This technique allows for measurement of the sample mass changes under operating conditions similar to that of the practical system. The absorption and desorption energies, hydration states and temperatures as well as the specific heat of materials can be determined. Modification of the apparatus to include evacuation capability

(Frazzica et al. 2014) as well as controlled water vapour supply (Jabbari-Hichri et al. 2015) allows for the sorption dynamics of the material to also be determined in a wide range of working conditions (closed and open system applications). As the performance of the TCM is strongly influenced by heat and mass transfer effects, sample size and reactor size are important factors that cannot be fully investigated with this technique due to the limited sample size it can handle. Thus, lab-scale prototypes are often required in further analysis of performance of TCM materials which further limits the comparability of results. The hydrate state of TCM materials with salt hydrates is also aften studied by x-ray diffraction. The sorption isotherms are also important characteristic parameters especially since the composite sorbent has different sorption behaviour to the native host material. Bespoke devices have been developed by some researchers (Dawoud & Aristov 2003) for this purpose and some employ commercially available thermogravimetric devices with controllable humidity.

Morphological changes as a result of loading the matrix with salt or hydration/dehydration cycling can be investigated using scanning electron microscopy (SEM) which can also be coupled with energy-dispersive x-ray spectroscopy (EDX) for determining the distribution of the salt in the matrix (Ristić & Zabukovec Logar 2018).

2.5.3 Microcapsule property requirements for thermochemical energy storage

To gain insight on the possible requirements of microcapsules for sorption heat storage applications, it is useful to survey available gas-solid reactor configurations and their operating conditions. For sorption TES reactors, both the heat and mass transfer performance must be optimised. For a reactor to fully utilize its storage capacity, the sorbent must access the whole reactor mass.

According to Solé et al. (2015), there are three main reactor types that can be used with solid TCM adsorbents: the fixed bed, moving bed and fluidized bed reactors. In fixed-bed reactors, the solid adsorbent particles are packed in a stationary bed through which the sorbate fluid flows. In moving bed reactors, the bed is gradually moved within the reactor volume. The fluidized bed reactors ensure more efficient heat and mass transfer and reduced sorption times by suspending the bed particles by using a sufficiently high fluid velocity (above the minimum fluidisation velocity). Factors affecting the minimum fluidisation velocity are the particle size and density as well as the viscosity and density of the fluid (Darkwa et al. 2006). Uniform distribution of the sorbate throughout the sorbent can be attained through the use of moving reactors as in the work of Zettl et al. (2014). However, such designs have an associated energy cost and thus there is much investigation into ensuring a good distribution of the sorbate in fixed beds by the inclusion of internal channels for improved distribution. Another practical factor in vapour sorption systems is the condensation at the reaction front through

the reactive bed which can lead to increased mass transfer resistance and a reduction in achievable energy storage capacity. This could also disrupt the stability of composite sorbents that are sensitive to excess water content and lead to salt loss.

The use of fluidised bed reactors in TCM energy storage is mostly focused on high temperature applications such as in concentrated solar power due to their higher conversion efficiency. However, interest in their application in low-temperature TCM energy storage is growing and Bardy et al. (2020) developed a bench-top fluidized bed reactor to investigate its use for low-temperature TCM storage based on zeolite 13X as adsorbent material in comparison to a fixed-bed reactor. They showed that the two types of reactor had similar energy storage capacities per mass of zeolite, however, the larger volume required for a fluidized bed was highlighted as an issue in delivering compact reactors for domestic applications. In such systems compression of the microcapsules due to the fluidising gas flow is possible and may lead to enhanced solvent loss (Finn & Galvin 2018).

2.6 Summary

The benefits of encapsulating chemical sorbents have been reported in the literature, especially in the specific case of CO_2 sorbents. Encapsulation has been shown to successfully enhance the sorption performance of new CO_2 solvents whilst overcoming issues related with precipitates, undesirable side products and viscosity. Similar issues can arise in sorption thermochemical energy storage and the objective of this work was to formulate an encap-

sulated thermochemical sorbent for energy storage applications. The field of thermal energy storage was introduced with particular emphasis on sorption thermochemical energy storage. Composite materials for sorption thermochemical energy storage were also reviewed including their formulation, application and advantages and disadvantages. Thus criteria for a suitable composite sorbent were specified and followed in this work.

A collection of available encapsulation methods are summarised and their advantages and disadvantages highlighted. The technique of microencapsulation by microfluidics was shown to be highly suited for the development of novel encapsulated sorbents due to the precise control it offers over microcapsule size and morphology. However, practical challenges associated with glass microfluidic device fabrication and reproducibility were demonstrated whilst also noting the limited adoption of device fabrication techniques developed in the literature to specifically address this issue. As such, the development of a simplified method for the fabrication of glass microfluidic devices using readily available materials is one of the objectives of this work. The transparency of glass microfluidics is a useful property for use with photo-initiated reactions. The photopolymerization of double emulsion droplet templates generated in microfluidic devices is a rapid technique for the formation of encapsulated sorbents with a dense polymer shell. This technique, used in conjunction with thiol-ene chemistry, was demonstrated as a powerful method to produce tailored shell materials for a target absorptive solvent and application.

Mechanical properties beyond the rupture strength of microcapsules of encapsulated chemical sorbents have seldom been the main focus in the lit-

erature due to the primary challenge of demonstrating improved sorption performance. However, a few studies have demonstrated the importance of understanding and describing the deformation behaviour of encapsulated sorbents in future systems. Micromanipulation has been established as an important technique in the study of the large compression deformation of a broad range of microparticles including cells which can be considered as core-shell microcapsules with an ultrathin semipermeable shell. It is often the case in the literature, that the intrinsic material properties of the bulk shell material of such encapsulated systems is unknown with significant analytical and numerical work devoted to the determination of such parameters. Therefore, the intrinsic bulk properties, deformation and strength parameters of a class of thiol-ene-based microcapsules will be studied in this work.

CHAPTER 3

Materials and methodology

The materials and experimental techniques used in the preparation of microfluidics devices and microcapsules and their subsequent operation and characterisation are presented in this chapter. Firstly, the formulation process is introduced from microfluidic device fabrication followed by emulsion generation and microcapsule formation by photopolymerization. This is then followed by morphological characterisation and finally, the characterisation of the thermomechanical properties of the microcapsules.

3.1 Formulation process

3.1.1 Materials

Three thiol monomers: pentaerythritol tetrakis(3-mercaptopropionate) (95%), trimethylolpropane tris(3-mercaptopropionate) (95%), 2,2'-(Ethylenedioxy)

diethanethiol (95%); the alkene monomers 1,3,5,-tri-allyl-1,3,5-triazine-2,4,6 (1H,3H,5H)-trione (98%) and diallyl phthalate (97%), the photo-initiator 2-Hydroxy-2-methylpropiophenone (97%), surface modifier trimethoxyphenylsilane (98%) and the surfactant poly(vinyl alcohol) (average M_w 13000-23000, 98% hydrolyzed), poly(ethylene glycol) (average M_n 20000) and dye Rhodamine B were used as received from Sigma-Aldrich. Perfluoropolyether (PFPE)-urethane dimethacrylate (Fluorolink MD 700) was used as the fluorinated monomer and sourced from Solvay Solexis S.p.A (Bollate, Italy). Borosilicate glass capillaries of the dimensions shown in Table 3.1 were sourced from VitroCom Inc. (NJ, USA) with Tolerances ± 10%.

3.1.2 Microfluidic device fabrication

Flow-focusing microfluidic devices were fabricated by a combination of methods adopted from Utada et al. (2005) and Amato et al. (2017) with the additional modification of an introduction of prefabricated capillaries. This eliminates the need for precision pulled capillaries that require accurate control of several variables and are inherently difficult to reproduce. The borosilicate capillaries used are shown in Table 3.1 with the dimensions, cross-sectional geometry and function shown (dimensions sourced from VitroCom Inc. based in New Jersey, USA, tolerances ± 10%). The capillary functions are defined according to the diagram in Figure 3.2.

The outer diameter of the collector and injector alignment capillaries is 0.87 mm which allows them to fit neatly in the 0.9 mm square profile of the housing capillary and also ensures good alignment of the capillaries.

Table 3.1: Microfluidic device capillary dimensions and function.

Function	Geometry	Length $[mm]$	Inner size $[mm]$	Wall thickness $[mm]$
Collection	Round	600	0.70	0.085
Injection	Square	100	0.20	0.100
Injector alignment	Round	100	0.70	0.085
Housing	Square	100	0.90	0.180

This 'square-round fitting method' is also utilised to align the injector capillary inside the injector alignment capillary before securing with resin (Super Glue).

The collector capillary was used as received, taking care not to grease the tip. In some cases it is necessary to modify the surface of the collector capillary to make it hydrophilic, as done by Amato et al. (2017) using a hydrophilic silane such as 2-[methoxy(polyethylenoxy)propyl] trimethoxysilane, however this was not necessary in our system as the flows were controlled to limit contact between the middle phase and the collector capillary and for the cases where contact occurred, the use of the device was not inhibited for an extended duration. The surface of the injector capillary was modified with a hydrophobic layer by submersing it in trimethoxyphenylsilane for at least 20 min removing the excess surface modifier with pressurised air. Hess (2012) noted that, depending on the surface modifier used, polymerisation of the silane resulted in debris that could block narrow channels, in our case, we did not observe the networks with the silane used and the apertures are large enough such that blockages are less likely even from other debris. It is then inserted into the injector alignment capillary to form the 'injector assembly'.

The diameter of the collector capillary needs to be reduced from 0.7 mm to a low enough value for the formation of smaller emulsion droplets in the flow-focusing device. A method similar to that used by Utada et al. (2005) was employed. This was done by heating one end of the capillary with a butane flame whilst slowly rotating the capillary. It was determined heuristically that rotation reduces the likelihood of an asymmetric decrease in the diameter as the glass melts in the flame. The size of the final diameter depends on the exposure time to the flame. Diameters in the range 50 μm to 400 μm were obtained.

Settling times of syringe pumps can vary from a few minutes to several hours and a 30 min wait time was observed to be suitable before starting the encapsulation process (Mavrogiannis et al. 2016). The flexibility and diameter of the tubing plays an effect on the stability of the flow. PEEK tubing of 1.5 mm diameter and thickness 0.3 mm was selected in this respect as it is rigid but not to the extent that it prevents the microfluidic device from being moved easily during repositioning or assembly.

A challenging aspect of the microfluidic device assembly is forming the connections with the tubing. The narrow gaps between the nested square and round capillaries can get easily filled by securing resin due to capillary action. Trying to minimise this by increasing the connector volume increases the likelihood of trapped air which contributes to instability of the flow. In the earlier development of glass capillary microfluidics, authors used the most readily available objects such as luer-stubs (Hess 2012). However, the advent of 3D printing has allowed for the development of the bespoke connectors shown in Figure 3.1. The connectors were printed using a Form 2 3D printer

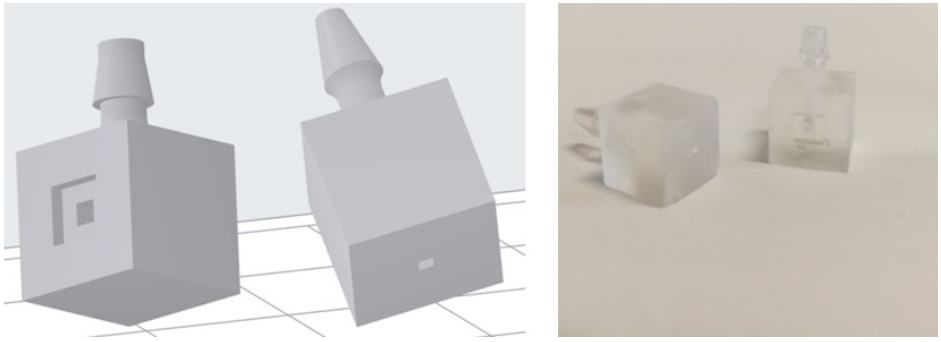

Figure 3.1: Microfluidic device connectors of the T-junction and "flow-through" type. The 3D design is presented on the left alongside the resulting printout on the right. Height of cube measures 1 mm.

(Formlabs, USA) and the Clear V2 resin. Clear V2 resin contains 55-75$wt\%$ urethane dimethacrylate and 15-25$wt\%$ methaclylate monomers (Formlabs, USA). The cured material shows good resistance to a wide range of solvents including water, hydrogen peroxide (3%), xylene and butyl acetate, showing a change in mass of less than 1% when a cube of 1 cm^3 of the material was exposed to the solvents for 24 hours. Similarly, no degradation was observed with the fluids used in the microfluidic system. The Clear V2 resin results in slightly transparent connectors which allows for an easier alignment of the capillaries within the connector before securing with resin. This ensures the right amount of resin is utilised, reducing the risk of resin blocking the microfluidic channels. Additionally, the cured Clear V2 resin has a greater thermal stability than the epoxy resin used to secure the glass capillaries which softens on heating gently with an air gun; this allows for the removal of a broken connector capillary without the need to discard the whole device if heat is applied at the damaged part with a hot air gun, improving the re-useability of the microfluidic devices.

Procedure: To form the injector assembly, two injector alignment capillaries are used to hold the square injector capillary in a stable, aligned position. These are also aligned within a short section of the square housing capillary. A small amount of Super Glue is then placed at one end of the shorter injector alignment capillary to fill the empty space by capillary flow. Care must be taken to ensure that the resin does not leak into the square housing capillary. This is allowed to cure over two hours.

The injector assembly is then inserted into a 33 mm long square housing capillary and this is inserted into two connectors of the T-junction type which sit at either end of the square housing capillary (marking the ends of the square capillary with black permanent marker makes their location within the connector more visible). This assembly is then carefully placed on a glass slide, ensuring that the ends of the square housing capillary do not pass the opening of the connector inlet, and the connector glued on to the slide with SuperGlue. The resin slightly dissolves the printed connectors and forms a strong bond with the glass on curing. It also allows for the channels to be visible through the glass slide. Once the two connectors are secured, the injector assembly is fixed in place using a small amount of epoxy resin. A third connector of the "flow-through" type is then passed at the end of the injector assembly and secured with SuperGlue. Once set, the capillary is secured within the connector with epoxy resin. The collector capillary can then be inserted and the alignment and distance to the injector assembly adjusted under a microscope. This can then be secured with a small amount of epoxy resin. Once cured, a excess amount of epoxy resin can be applied at the connection points to ensure a good seal without risk

of the resin leaking into the channels. A schematic of the microfluidic device and assembly procedure is shown in Figure 3.2.

3.1.3 Preparation of photopolymers

The thiol-ene photopolymers were prepared mixing the thiol and alkene monomers at 1:1 ratio of the thiol and ene functional groups. The photoinitiator (2-Hydroxy-2-methylpropiophenone) was then added to this mixture ($2wt\%$). The mixture was prepared in a glass vial covered with aluminium foil and within a fume cupboard with UV protective film to prevent unwanted photoinitiation events. The mixture was stirred gently to ensure complete mixing without the entrapment of air bubbles which can result in a porous cured resin if present. A similar procedure was followed with the preparation of the perfluoropolyether (PFPE)-urethane dimethacrylate photopolymer. However, as with other acrylate systems, the mixture suffers from oxygen inhibition and requires degassing before further use in the microfluidic device. The monomers used in this work are visualised in Figure 3.3 and Table 3.2 summarises the monomer combinations used in this work as well as the abbreviations that will be used in reference to them for the rest of this work.

As information on thiol-ene membranes for the selective transport of water from aqueous inorganic salt solutions is limited, selection of these monomer combinations was based on their commercial availability, hydrophobicity and thermal stability for the case of TT and PT materials. The onset of thermal decomposition temperatures of TT and PT materials are $352°C$ (Li et al. 2009*a*) and $371°C$ (Stovall et al. 2004), respectively, with corresponding

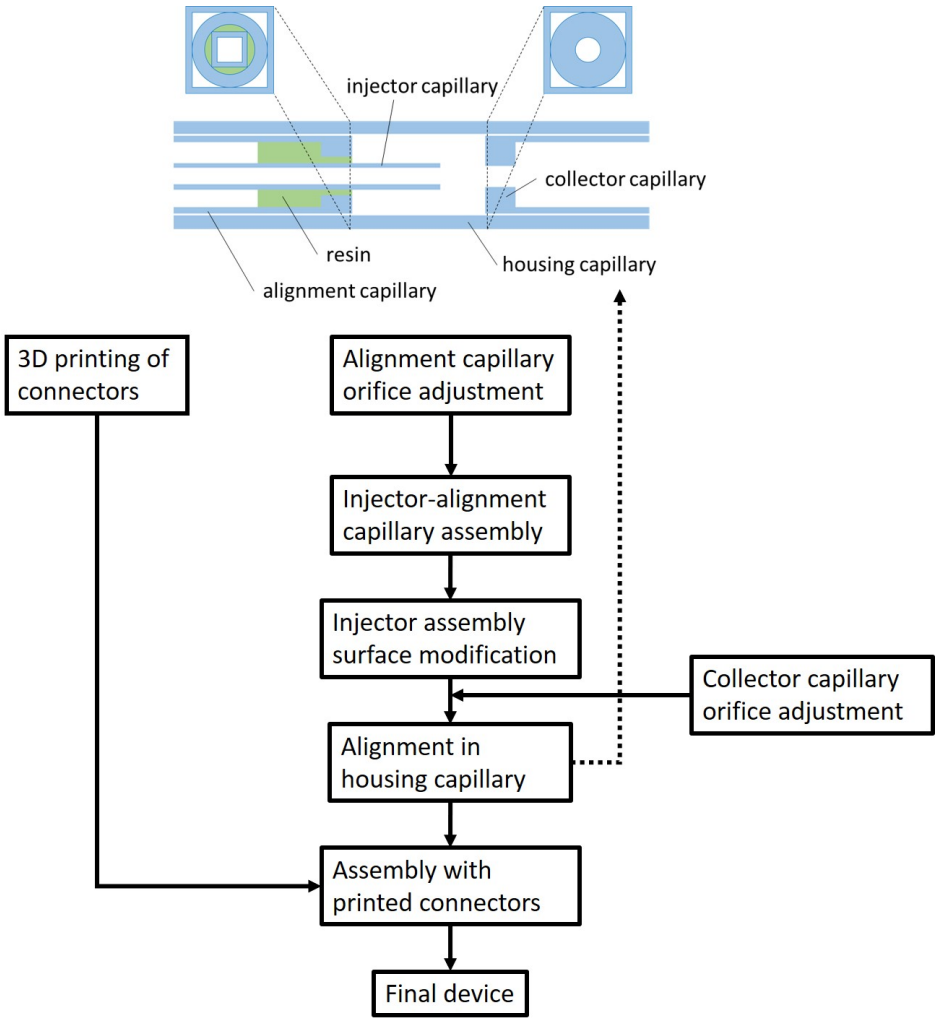

Figure 3.2: Schematic of flow-focusing microfluidic device (top) and fabrication procedure (bottom).

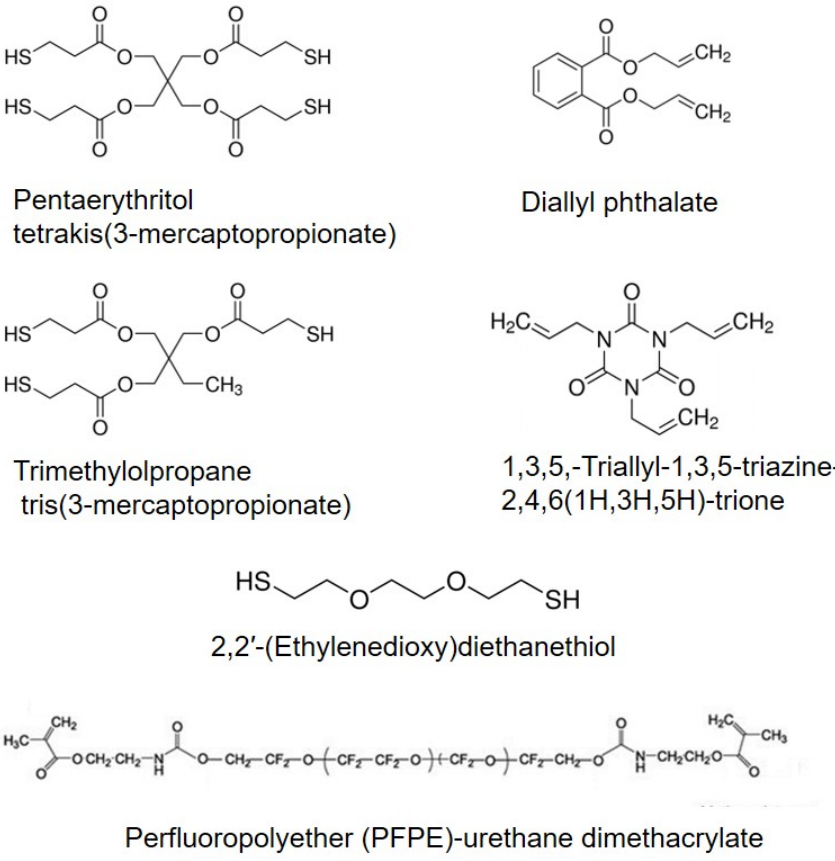

Figure 3.3: Chemical structure of monomers used in the formation of microcapsule polymer shells.

Table 3.2: Monomer combinations and polymer product names.

Thiol monomer	Alkene monomer	Product name
2,2'-(ethylenedioxy) diethanethiol	1,3,5,-tri-allyl-1,3,5-triazine-2,4,6(1H,3H,5H)-trione	DT
Trimethylolpropane tris(3-mercaptopropionate)	1,3,5,-tri-allyl-1,3,5-triazine-2,4,6(1H,3H,5H)-trione	PT
Pentaerythritol tetrakis(3-mercaptopropionate)	Diallyl phthalate	TP
Pentaerythritol tetrakis(3-mercaptopropionate)	1,3,5,-tri-allyl-1,3,5-triazine-2,4,6(1H,3H,5H)-trione	TT
Perfluoropolyether (PFPE)-urethane dimethacrylate	Perfluoropolyether (PFPE)-urethane dimethacrylate	F

water vapour permeability values (room temperature, RH = 100%) of 0.022 $g\ cm\ m^{-2}\ day^{-1}$ and 0.042 $g\ cm\ m^{-2}\ day^{-1}$, respectively (Hoyle et al. 2013). The water vapour permeabilities are comparable to those fo common barrier polymers such as polyethylene terephthalate (PET) at 0.070 $g\ cm\ m^{-2}\ day^{-1}$ and polyproylene (PP) at 0.025 $g\ cm\ m^{-2}\ day^{-1}$ measured at a relative humidity of 90% and a temperature of $38°C$ (DeLassus 2002).

Table 3.3 presents the values of the interfacial tension and viscosity of the photopolymers used in this work as well as the inner and continuous phase fluid properties. Density data for the PEG solutions were estimated from the work of Ninni et al. (2003) whereas the viscosity data for the PEG solutions were estimated from the work of Kirinčič & Klofutar (1999). The notation PEG20-15, denotes a $15wt\%$ aqueous polyethylene glycol solution of average $M_n = 20000$, for example.

Table 3.3: Measured interfacial tension with distilled water, density and viscosity values for the fluids used in the generation of emulsion droplets.

Substance	Interfacial tension $[mN\ m^{-1}]$	Density $[g\ cm^{-3}]$	Viscosity $[mPa\ s]$
Tetrakis-trione	12.449 ± 0.003	1.244	332.1
Tetrakis-phthalate	14.312 ± 0.004	1.244	50.0
Propane-trione	14.972 ± 0.001	1.190	143.9
Diethane-trione	12.288 ± 0.004	1.093	10.6
PFPE-urethane dimethacrylate	12	1.300	581
LiBr [1 $g\ cm^{-3}$]	-	1.550	4.1
CaCl2 [0.75 $g\ cm^{-3}$]	-	1.424	11.2
PEG20-5	-	1.005	4.3
PEG20-10	-	1.014	14.5
PEG20-15	-	1.023	39.4
PEG20-20	-	1.032	92.4

3.1.4 Microfluidic device operation and microcapsule formation

A w/o/w double emulsion was generated in the microfluidic device by pumping three fluids through the microfluidic device. Figure 3.4 is a schematic of the flow system used in the generation of the microcapsules. Three syringe pumps (Legato 200 Series, KDScientific; Pump 11 Elite and PHD Ultra 2000 from Harvard Apparatus) were used to drive the flow of the core, middle and continuous phases. The core and middle fluids were delivered through 1 ml syringes (BDPlastik) and that of the continuous phase in 10 ml syringes. A smaller syringe volume ensures a more stable flowrate from the syringe pump and the volumes used in this work represent the optimal syringe volume for the required flowrate and pumping time. Short tubing lengths delivering the fluids to the microfluidic device were used in order to minimise the pressure

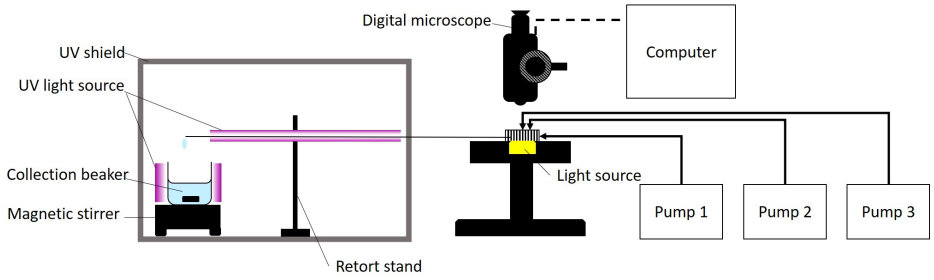

Figure 3.4: Schematic of syringe pumping system connected to microfluidic device and in-line UV photopolymerization set-up.

drop. Before connecting the tubing to the microfluidic device, they were first primed with the operating fluid to reduce the likelihood of air pockets and shorten the waiting time for flow to commence at the flow-focusing junction. The flowrates of the three fluids were independently adjusted to obtain double emulsions and the formation process observed with a digital microscope at a frame-rate of $\sim 30\ fps$.

The formed emulsion droplets were photopolymerised as they exited the microfluidic device by exposure to UV light (365 nm, 14.4 $W\ m^{-1}$) along the length of the collector capillary (circ. 600 mm) as illustrated in Figure 3.5. The particles were then allowed to drip into a stirred beaker and exposed to UV light for at least 30 min. This ensures complete curing of the shell as the curing time is affected by the thickness of the oil phase as well as the depth and opacity of the carrier phase.

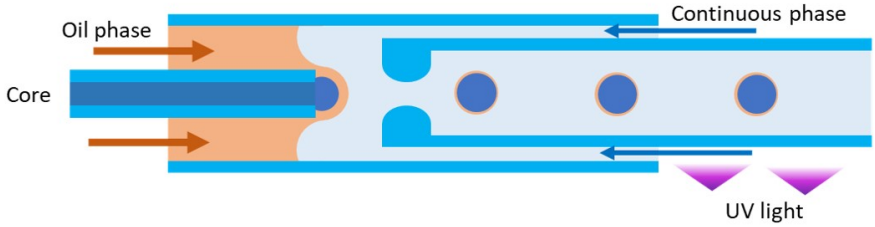

Figure 3.5: Schematic of emulsion generation and microcapsule curing with UV light (365 nm).

3.2 Microstructure and chemical characterisation

3.2.1 Microcapsule morphology and size distributions

The transparent nature of the shell material of the microcapsules make them particularly amenable to morphological studies by optical images. An optical microscope (Axioscope A1, Zeiss) was used to take a series of images of microcapsules collected from the microfluidic device. An aliquot of the suspended microcapsules was pipetted into a vial with distilled water in order to dilute the continuous phase for a better optical image quality. The microcapsules were then pipetted onto a glass slide and covered with a cover-slip for optical imaging. Although the images only provide a 2-dimensional cross-section of the particles, they allow for the estimation of the shell thickness in addition to the particle size distribution and loading capacity. This would not be possible with the more traditional light-scattering based techniques for the measurement of the particle size distribution as it would not be possible to measure the diameter of the core.

The particles from the microfluidic droplet generation process can lead to droplets with little to no core material or core-shell microcapsules with a

non-uniform shell thickness. The shape of the capsules is also not necessarily spherical. A non-traditional software that can deal with these differences is the AutoCAD software package that allows for the outline of capsules to be traced individually. Spherical capsules can be traced as spheres and elliptical capsules as ellipses. This was done for at least 100 microcapsules for statistically significant results. Figure 3.6 shows an example of a traced microcapsule with the core and shell represented by the white and red lines, respectively, as well as an oil droplet traced in green. The two-dimensional images used for the size measurements were taken at the plane at which the outer edge of the capsule was in focus. For cores that are not concentric with the microcapsule in three-dimensions (3D), the core radius at this focused plane may be different to the true (three-dimensional) radius of the core. For core-shell microcapsules with a high volume fraction of the core, as in this study, the error in the core radius measurement with this technique was relatively low at less than 10% for a volume fraction of $60vol\%$ and less than 5% for a volume fraction of $73vol\%$ (Appendix E). Thus, the relatively low error and facile measurement offered by the optical technique compared with 3D imaging techniques (e.g. micro-CT), make it a suitable technique for studying the transparent core-shell microcapsules. Information about the traced objects include the dimensions, object centres and colour. This allows the capsules to be discriminated from the oil droplets by colour and this information can be used to calculate the efficiency of the microcapsule generation process as well as the average thickness, $\overline{h}$, using Equation 3.1, derived in Appendix E.

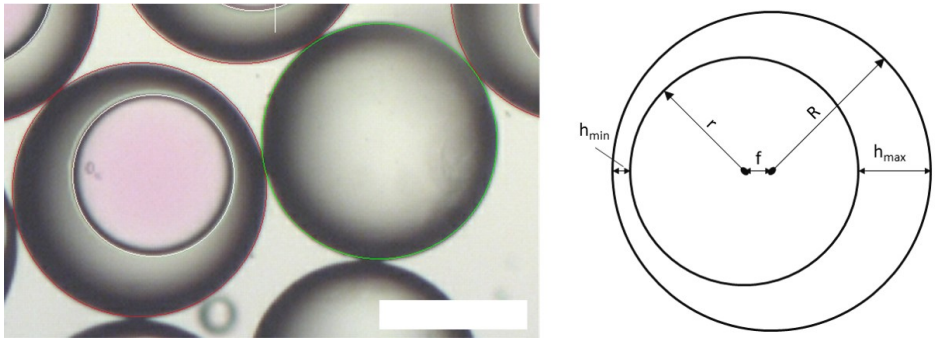

Figure 3.6: Example of microcapsule tracing method to obtain size characteristics (left) and illustration of parameters used for further calculation (right). Scale bar is 200 μm.

$$\overline{h} = \sqrt{R^2 + f^2} - r \tag{3.1}$$

The values of the microcapsule inner and outer diameters allow for the determination of size distributions and calculation of the volume-weighted mean diameter $d_{4,3}$ in Equation 3.2,

$$d_{4,3} = \frac{\sum_1^n {d_k}^4}{\sum_1^n {d_k}^3} \tag{3.2}$$

where d_k is the diameter of the kth particle.

The coefficient of variation (CV), in Equation 3.3 as well as the span, in Equation 3.4, describe the spread of the distribution data,

$$CV = \frac{\sigma}{\overline{\mu}} \tag{3.3}$$

$$s = \frac{d_{v0.9} - d_{v0.1}}{d_{v0.5}} \tag{3.4}$$

where σ and $\overline{\mu}$ are the standard deviation and mean of the distribu-

tion, respectively, and $d_{v0.9}$, $d_{v0.1}$ and $d_{v0.5}$ are the sizes below which $90vol\%$, $10vol\%$ and $50vol\%$ of the material is contained, respectively. For the type of microcapsule shown in Figure 3.6, the shell inhomogeneity can be described by the ratio h_{max}/h_{min} according to the schematic in the right of Figure 3.6.

3.2.2 Scanning electron microscopy (SEM)

SEM allows for the interrogation of the surface morphology and microstructure of a substance and has a significantly greater depth of field than an optical microscope. In a SEM, an electron beam, generated from an electron gun, is accelerated by an applied voltage and then focussed onto the surface of a specimen by electromagnetic lenses. The high-energy electrons striking the surface of the specimen can be scattered either elastically or inelastically by the atoms in the specimen. Back-scattered electrons (BSEs) are the result of elastic scattering and secondary electrons (SEs) are the result of inelastic scattering. SEs are used to generate images with high topographic contrast and have a higher spatial resolution than those formed from BSEs which are primarily used to provide information on compositional contrast (Leng 2013). Since electrons are charged particles, the image quality deteriorates with the charge of the specimen and it is thus important that the specimen to be conducting. For organic specimens, this is achieved by coating with a thin layer of an inert metal such as gold or silver.

The microcapsules were split open with a surgical scalpel and mounted on a conductive carbon pad. The salt-laden microcapsules were dried in a vacuum desiccator to remove as much moisture as possible to ensure that

water vapour does not affect the downstream sample preparation process which also occurs in vacuum conditions. The assembly was then coated with 5 nm gold in an argon atmosphere using a sputter coater (Q150R ES, Quorum, UK). The microcapsules were scanned in a TM3030Plus Hitachi SEM at a voltage of 5 kV for up to 20 min without any visible damage to the capsule surface. As the microcapsules are dried in vacuum conditions prior to testing in the SEM, it is expected that the vacuum conditions in the SEM will have little effect on the microcapsule morphology. However, smaller surface features may be affected by the coating process. The micrographs were used to verify the encapsulation of the salt and identify any larger internal and external surface features due to the presence of the salt.

3.2.3 Three-dimensional image characterisation

X-ray micro-computed tomography (micro-CT) is a non-destructive technique used to investigate the internal structure of a sample in three dimensions. X-rays are used to take multiple two-dimensional projections of the sample at different angles of rotation and these projections are used to construct a three-dimensional image of the sample (O'Sullivan et al. 2018). Differences in attenuation and penetration of the x-rays through the different constituent components within the sample give rise to contrast in the image allowing for the different constituent components to be identified.

MicoCT was used to investigate the three-dimensional structure of salt-laden microcapsules (SkyScan-2211, Bruker). The sample is rotated between the x-ray source and detector. The method of magnification depends on

the device used. Some devices use optical magnification of the signal from the scintillator before passing to the detector whilst other devices use the natural propagation of the x-rays from a point source to an x-ray camera to achieve magnification. The SkyScan-2211 is equipped with an 11 $Mpixel$ CCD camera. The sample is mounted on to a high-precision air bearing rotation stage to allow for precise small angle rotations of the sample during measurement. The sample is moved between the CCD camera and the source to obtain the required magnification. The transmission through a sample is optimised by adjusting the filter and voltage settings to ensure a maximum signal-to-noise ratio whilst minimising reconstruction artefacts. Increasing the voltage increases the average energy of the x-ray beam and thus the transmission and vice versa. A filter can also be used to improve the average energy of the x-ray beam passing through the sample by filtering out the x-ray photons at the lower end of the energy spectrum which has the effect of improving the signal-to-noise ratio.

Sample size and stability are important factors that affect the quality of the X-ray scan. The sub-millimetre scale of the microcapsules necessitates the need for a small distance between the x-ray source and the sample in-order-to capture the minute details. Thus, a thin, rigid, low-density structure is required to secure the microcapsules for the duration of the scans. A cylindrical sample holder fashioned from a cocktail straw with an external diameter of circa 3 mm was found to be reasonably rigid with a low enough density so as not to greatly influence the scanning parameters. A single layer of double-sided tape was applied to the outer surface of the sample holder to ensure that capsules were securely fixed. For the much larger magnifica-

tion required for examining individual microcapsules, the cylindrical sample holder was sectioned using a scalpel and the double-sided tape applied as before. This allowed for an even closer approach towards the sample by the x-ray source resulting in higher magnification.

In this work, the x-ray source current and voltage were set at 80 μA and 60 kV, respectively. An exposure time of 350 ms per frame was used with a sample rotation step of 0.4°. Finally, the number of averaged frames during the acquisition was set at four.

3.3 Thermal and mechanical characterisation

3.3.1 Microcapsule mechanical properties by micromanipulation

The mechanical properties of the microcapsules were characterised using the micromanipulation technique involving compression between two flat surfaces as detailed by Zhang et al. (1992). An image and schematic of the micromanipulation rig is shown in Figure 3.7. Microcapsules with the dye Rhodamine B in the core were pipetted onto the glass stage. The pink microcapsules were readily distinguishable from colourless polymer particles that may be present in the aliquot. Excess water on the glass stage is then carefully absorbed with tissue paper folded into a point. Compression was commenced immediately to minimise the effects of the loss of the water core due to evaporation. Only isolated microcapsules were compressed to ensure that the force was applied on a single particle each time. A glass probe, 1 mm in diameter, was used to

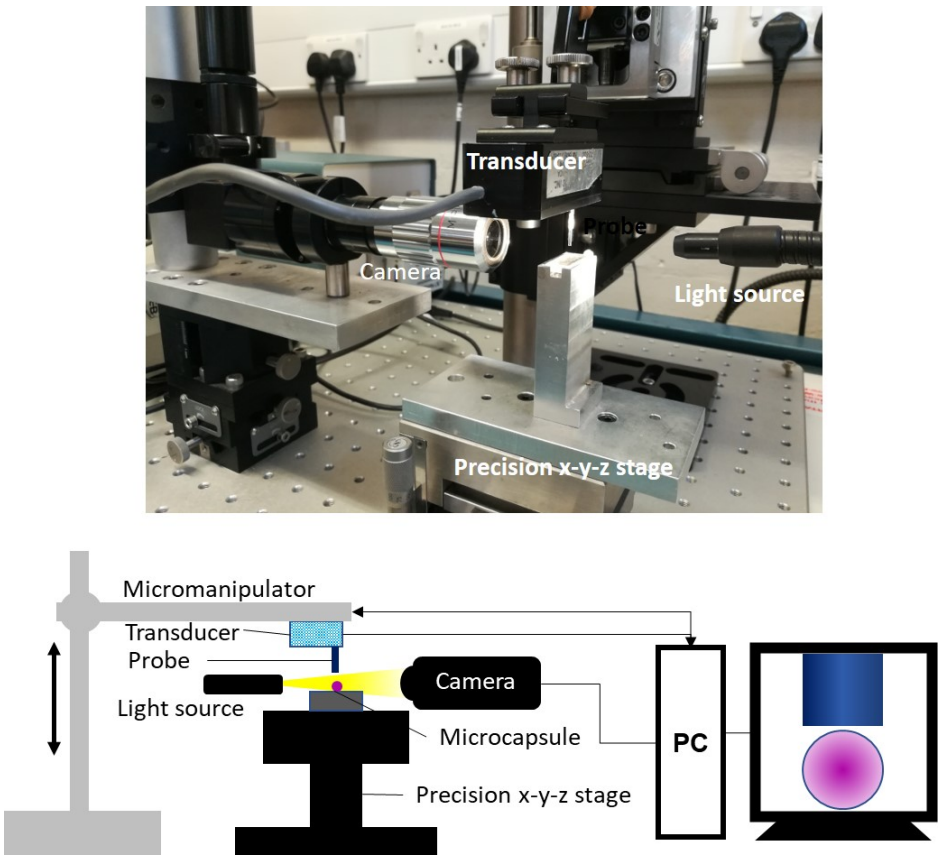

Figure 3.7: Micromanipulation set-up image (above) and schematic of micromanipulation rig modified from the work of Zhang Z. (2001) (below).

compress the microcapsules. The probe was attached to a force transducer (Model 407A, Aurora Scientific Inc., Canada) which was calibrated prior to use following the protocol of Zhang et al. (1992). The set-up is mounted on a precision-controlled stage and the compression observed via a microscopic optical set-up using the side-view camera. The microcapsules were compressed at a speed of 8 $\mu m\ s^{-1}$ whilst measuring the force via the voltage signal from the force transducer. With this set-up, the smallest recordable force was 0.49 mN.

Measurement uncertainty in this technique arises from the force trans-

ducer resolution as well as identification of the moment contact is established between the probe and particle. For non-spherical particles an additional contributing factor to the error is the determination of the diameter. In this study, microcapsule diameters were measured from the image using the width of the probe as a reference. Liu et al. (1998) found a significant contribution to the uncertainty of the measured force below deformations of 5% and thus limited their estimation of the Young's modulus to deformations in the range of 5 – 10%.

The probes used for compression of the microcapsules were prepared from borosilicate glass rods 1 mm in diameter. Tapering of the glass probes was not necessary as the 1 mm diameter was approximately three times the diameter of the largest microcapsule and would thus ensure that the compressed microcapsule is constantly underneath the probe. The glass rods were cut to the required length using a diamond-tip glass cutter and then ground to a smooth, flat surface. Sufficiently flat probes were then attached to the transducer using SuperGlue.

Prior to the compression measurements of the microcapsules, the compliance of the micromanipulation probe was determined to ensure accuracy of the force-displacement data. As the force transducer consists of a cantilever on which the probe is attached, bending of the cantilever upon compression results in a small displacement error which is proportional to the compressive force. The compliance was measured by contacting the probe directly against the glass base at the experiment compression speed u_c and calculated according to Equation 3.5.

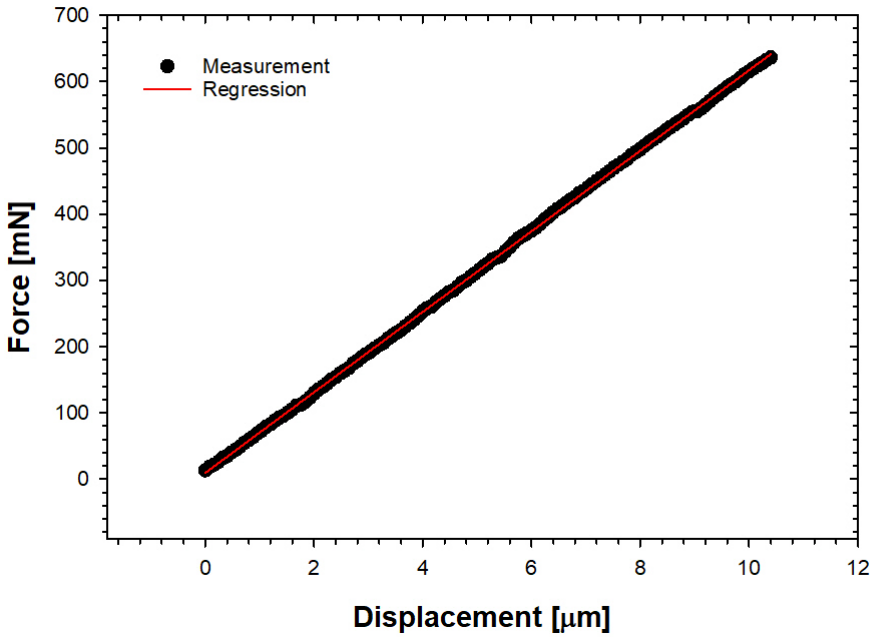

Figure 3.8: Experimental measurement data and regression fitting of compliance plot (R-squared = 0.998). Gradient represents the compliance.

$$C = \frac{u_c t}{m\kappa} \tag{3.5}$$

Where t is the acquisition time, κ is the transducer sensitivity and m is the mean gradient of three compliance measurements determined from the compression measurement data as shown in the example measurement result in Figure 3.8. The displacement error d_ϵ from an applied load F_c is subsequently computed according to Equation 3.6 for the microcapsule compression measurements.

$$d_\epsilon = u_c t - F_c C \tag{3.6}$$

3.3.2 Glass transition temperature of the shell material by DSC

The glass transition temperature of the thiol-ene polymers were measured by a differential scanning calorimeter (DSC) (DSC3+, Mettler Toledo). Samples were prepared in 40 μL aluminium crucibles by pipetting the uncured thiol-ene resin into the pan to ensure complete contact with the base of the pan and exposing the resin to a panel of UV LED strips (365 nm, 14.4 $W\ m^{-1}$) for $> 30\ min$. The heating rate was $10°C\ min^{-1}$ and the second scan data used to determine the glass transition temperature.

3.3.3 Absorption and desorption properties of the microcapsules

Operating principle and set-up

The heat flux and sample mass variation during sorption and desorption experiments were analysed using a simultaneous thermal analyser (STA) (STA PT 1600, Linseis). The technique is a combination of differential scanning calorimetry (DSC) where the differential heat-flow between a sample and reference is measured, and thermogravimetry (TG), where the mass change with temperature is recorded. The mass change and heat transfer to or from a sample with respect to temperature are measured simultaneously in a thermobalance. A thermobalance consists of a sensitive microbalance and computer controlled furnace used to record the mass and temperature of a sample under controlled heating in a regulated atmosphere (Brown 2001). A

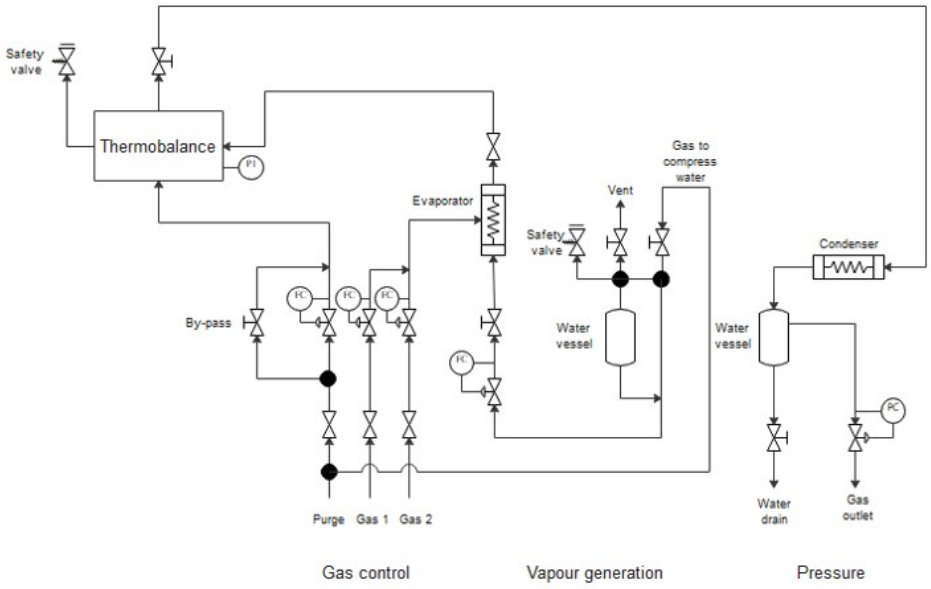

Figure 3.9: STA set-up showing water vapour generation module.

schematic of the STA is presented in Figure 3.9.

During operation, a sample and reference are mounted adjacent to each other on a sample holder with platinum conducting bases, the sample holder is itself, mounted on the balance (Figure 3.9). A thermocouple junction is connected at each conducting base to measure the temperature of the sample and the reference as well as the temperature difference between the two which is the DSC signal. In a simplified form, the temperature difference (ΔT) can be related to the heat flow rate (ΔQ), provided the thermal resistance (R_θ) is known, according to $\Delta Q = \Delta T / R_\theta$. This is the operation principle for heat flux DSC as opposed to an alternative technique that measures the enthalpy change directly known as power-compensated DSC (Tanaka 1992). A purge gas flows through the balance chamber and into the furnace where it mixes with the reaction gas as shown in Figure 3.9.

A sample reaction such as melting or sorption appears as a peak in the

differential signal between the sample and reference temperature profiles. The integral of the peak can be correlated with the enthalpy of the reaction/transition by a calibration factor. The calibration factor can be determined by measuring the peak area of the melting transition of standard samples that have transitions in the temperature range of interest (Leng 2013). Normally three standard materials are used under the same atmosphere and gas-flow conditions as in the experiment with at least two heating and cooling rates in the interest of reliability. For the TG part of the device, the sample is weighed externally on a microbalance and the thermobalance is tared before an experimental run, therefore both the relative and absolute mass changes can be determined.

Possible variations in the conditions of the sample and the reference that can lead to errors can arise from buoyancy and thermal shielding effects can also affect the gravimetric measurements (Leng 2013). This is more-so when the case the sample is placed in a hanging balance and the thermocouple is not in direct contact with the base of the sample as in certain devices. In addition, a key assumption with regards to the DSC set-up is that the environmental conditions of both the sample and the reference are indistinguishable. In order to account for these issues, a "blank" run is performed under the same conditions with the reference and empty sample crucible, the TG and DSC signals from this run are then subtracted from the sample runs.

The STA used in the experiments was configured with a steam generator as shown in Figure 3.9. The gas flowrates are controlled using mass flow controllers through the system software. The system was set-up for the delivery of moisture in the furnace at temperatures above $150°C$ using a steam gener-

ator. Water at a set flowrate is mixed with a nitrogen gas stream in the steam generator which produces a mixture of nitrogen and water vapour at $150°C$. The stream then passes into the furnace where it mixes with the purge gas. The relative humidity (RH) in the furnace chamber was calculated from the water mass flow rate and total gas flowrate according to Equations 3.7 and 3.8.

$$RH = \frac{C_\nu p_{sat}}{P} \tag{3.7}$$

Where C_ν is the volumetric concentration of water vapour in the gas stream calculated from Equation 3.8, p_{sat} is the saturated vapour pressure of water calculated according to Equations 3.9 and 3.10 and P is the furnace pressure.

$$C_\nu = \frac{22.4\dot{m}TP}{M_R Q_g} \tag{3.8}$$

where $\dot{m}$ is the water mass flow rate, M_R is the relative molar mass of water, Q_g is the total gas flowrate and the ideal gas molar volume is 22.4 dm^3.

The saturated vapour pressure of water is calculated using the Magnus formula (Bell 1996) (Equation 3.9) based on the furnace temperature.

$$\ln p_{sat} = \ln 611.2 + \frac{17.62T}{243.12 + T} \tag{3.9}$$

The actual vapour pressure p_c in the presence of other gases is given by Equation 3.10 where the vapour pressure p_{sat} is multiplied by an enhancement factor f_ϵ to account for the presence of other non-ideal gases (Bell 1996).

$$p_c = f_\epsilon p_{sat} \tag{3.10}$$

Water vapour loss of microcapsules

A small volume of microcapsules suspended in water were collected in a 3 ml disposable pipette. A piece of tissue paper was then used as a filter by placing it at the opening of the pipette and gently squeezing out the water. It was assumed that the remaining capsules only had a thin layer of capillary water on the surface. The capsules were then gently deposited into a 40 μL platinum crucible by squeezing the pipette and weighed before placing immediately in the thermobalance for measurement. Three sample measurements were carried out for each capsule type at a temperature of $30°C$ under a nitrogen flowrate of 550 $sccm$ at atmospheric pressure until a final equilibrium mass was reached.

Sorption measurements of salt-laden microcapsules

Absorption-desorption measurements were performed on microcapsules with a salt core in order to determine the sorption dynamics and heat storage capacity. Microcapsules are loaded into a 40 μL platinum crucible and the sample weight determined by weighing on a microbalance. The sample is then subjected to a sorption and desorption cycle involving an isothermal ($30°C$) hydration step for 120 min followed by dehydration as a result of heating to a set-point temperature of $150°C$ at a heating rate of $5°C\ min^{-1}$. A settling time of 5 min was allowed before the hydration step commenced by controlling the mass flow rate of water into the furnace. The minimum

flowrate that could be set in the water mass flow controller was 0.1 $g\ hr^{-1}$, however, in practice, it was found that this flowrate could not be maintained over the long periods required for sorption experiments and the actual minimum stable flowrate was 0.3 $g\ hr^{-1}$. This value corresponds to a relative humidity value of 23% at 30°C. Higher water mass flow rates required a higher carrier gas flowrate to ensure that water did not condense in the transfer tubing. This introduces greater turbulence in the furnace which can lead to heat losses and inaccuracies in the measurement of the heat fluxes. Furthermore, high carrier gas flow rates lead to practical complications related with the frequent replacement of gas cylinders. A schematic of the hydration and dehydration steps is presented in Figure 3.10. The cycle was repeated three times per sample. The microcapsules in the initial cycle are used directly after production from the microfluidic device and are thus partially hydrated. This final mass after dehydration in the first cycle is thus used as the dry mass of the microcapsules in subsequent calculations.

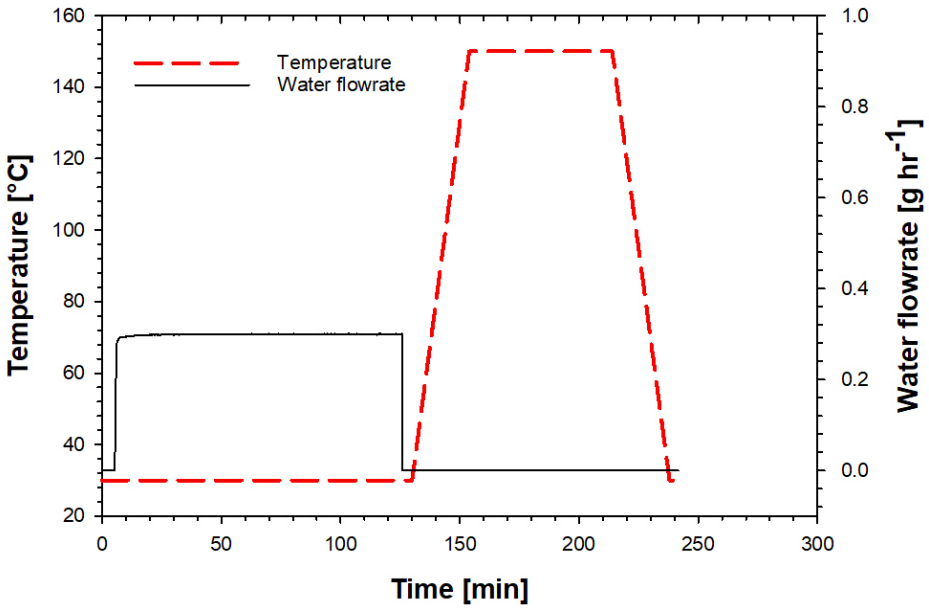

Figure 3.10: Hydration-dehydration cycle set-up for STA measurements.

CHAPTER 4

Results and Discussion I: Microfluidic device operation and microcapsule generation

Glass microfluidic devices offer a 3D alternative to the ubiquitous 2D devices produced by lithography. They are an inert, rigid and transparent platform that presents opportunities for the development of new material composites that would otherwise not be possible with PDMS-based devices which are susceptible to swelling and leaking by certain solvents. Simplifications to the design and assembly of glass microfluidics have reduced the cost and need for expensive fabrication equipment and allowed for their growth in use over the years (Li et al. 2013).

The general glass MFD consists of a tapered inlet and collector glass capillaries within a square capillary for alignment. The capillaries are tapered using a glass capillary puller and are then subsequently ground to the desired diameter. This can be a time-consuming process due to the inefficiency

in producing axis-symmetric, pulled capillaries and also on account of the long hours required to grind a single capillary to the required tip diameter. Connection of the glass capillaries to the tubing is usually achieved by using disposable syringe needle tips secured by epoxy resin or by sticking the tubes directly to the capillaries (Vladisavljević et al. 2014). The syringe needle tips increase the total volume of the device and project vertically upwards which is not suitable for all microscope optical configurations. Additionally, the small surface area available for sticking the needles increases the likelihood of leaks. These factors affect the properties of produced emulsions such as the monodisperisty as well as the range of flowrates where emulsions are formed. There is therefore a need for the development of a reproducible MFD such that the device geometry can be fixed.

In this chapter, a simple design of an MFD assembled from capillaries of a predetermined size connected with specially designed 3D-printed connectors is presented. Double and multicore emulsions were produced in the MFDs with an aqueous inner phase and a middle phase of photopolymers of varying density and viscosity in an aqueous carrier phase. The influence of flow conditions on the emulsion droplet size, distribution, morphology and droplet formation mode is presented. The relationship of the middle phase density and viscosity on the capsule shell thickness and homogeneity is also discussed.

4.1 Microfluidic device fabrication and durability

4.1.1 Fabricated microfluidic devices

Fourteen flow-focusing MFDs were produced with an inlet square glass capillary with an inner width of 200 μm. Figure 4.1 shows a typical assembled microfluidic device with the 3D-printed connectors and flow directions of the fluid phases. A complementary image and schematic of the flow-focusing point of the device is shown in Figure 4.2 illustrating the internal arrangement of capillaries and flow directions. The height of the device is low enough to allow easy access of the optical set-up of most laboratory microscopes and it also fits onto a single glass slide which allows it to be secured on the microscope stage.

Table 4.1 shows the dimensions of the diameter of the inlet of the collector capillary as well as the distance between the injection and the collection capillaries in the microfluidic device. Variation in the diameter arises from the variation in exposure time of the capillary tip to the butane flame ($> 1300°C$) during the the melting process of narrowing the collector capillary opening. However, this process is significantly faster than that of pulling and grinding the capillary tips to the required diameter which often results in breakage and waste of the glass capillaries. The length of the spacing between the injector and collector capillaries (l) is also variable as a result of human error, however, the ratio of this length to the collector capillary orifice diameter d_c shows good reproducibility. The value of l/d_c was shown by Nabavi et al. (2017) to affect both the morphology and size of emulsion droplets.

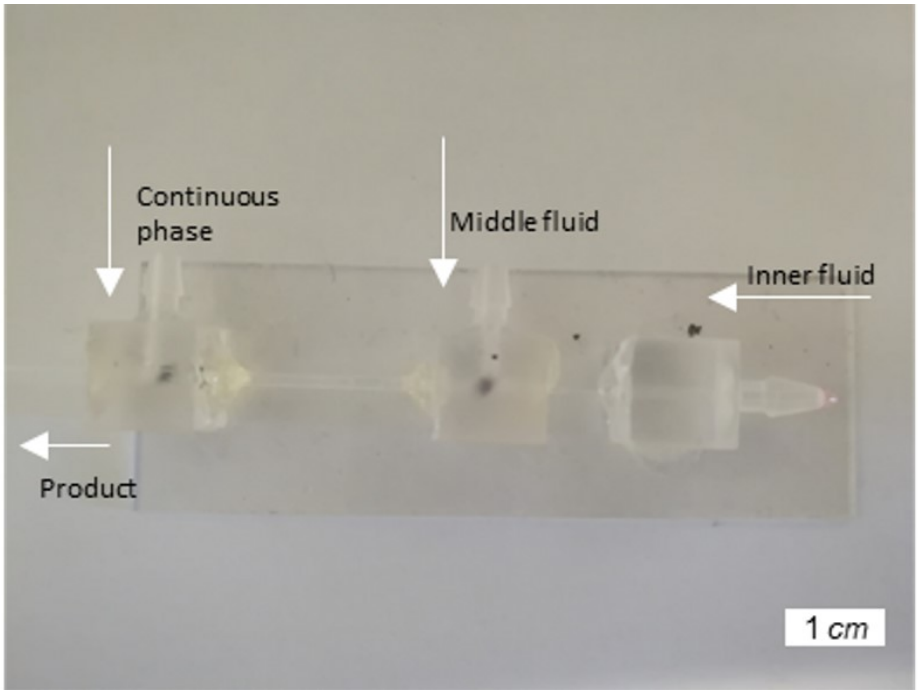

Figure 4.1: Assembled microfluidic device showing 3D-printed connectors and flow direction of fluid phases.

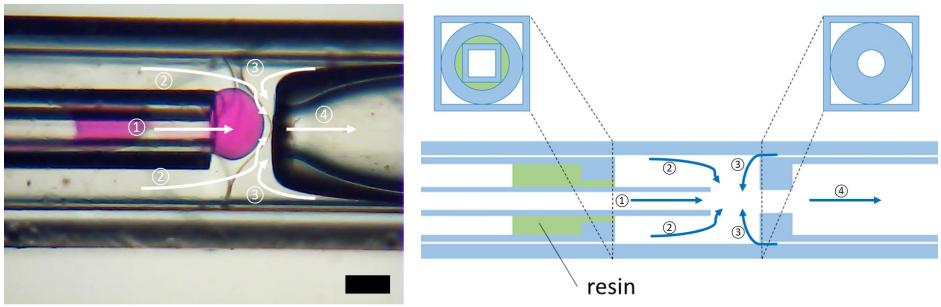

Figure 4.2: Assembled microfluidic device (left) with schematic (right) showing cross-section of injector nozzle assembly and collector capillary. Arrows indicate the flow direction and are numbered 1 to 4, indicating the flow direction of the internal, middle, continuous and total fluids. Scale bar is 200 μm.

Table 4.1: Flow-focusing glass capillary microfluidic devices and their dimensions.

Number	Collector inlet $[\mu m]$	Inlet-to-collector distance $[\mu m]$	Error $[\mu m]$	Ratio [-]
MFD1	198.8	500.3	1.1	0.4
MFD2	204.1	485.9	1.2	0.4
MFD3	199.8	363.5	0.7	0.5
MFD4	269.2	485.5	0.7	0.6
MFD5	278.9	486.6	1.1	0.6
MFD6	231.7	388.4	1.1	0.6
MFD7	272.2	448.8	1.7	0.6
MFD8	260.1	408.5	1.5	0.6
MFD9	244.1	380.7	0.6	0.6
MFD10	240.6	351.6	1.3	0.7
MFD11	267.5	359.2	0.9	0.7
MFD12	369.2	465.0	2.1	0.8
MFD13	285.1	353.5	1.7	0.8
MFD14	380.1	452.9	1.9	0.8

As $l/d_c \rightarrow -1$, when the injector tip is inserted into the collector capillary, emulsion droplets transition from single-core to double-core droplets and as $l/d_c \rightarrow 1$, when the injector tip is drawn away from the collector capillary, emulsion droplets are enlarged. This is explained by the fact that, the closer the injector capillary tip is to the collector capillary orifice, the higher the shear force exerted on the droplets at the same average flowrates. The values in Table 4.1 indicate the suitability of this fabrication technique in setting the value of l/d_c as well as fixing the injector capillary orifice diameter.

4.1.2 Surface modification and device durability

The wetting properties of the capillary walls in the MFD facilitate the formation of the double emulsion. In-order-to generate water-in-oil-water dou-

ble emulsion drops, the walls of the injector capillary were made hydrophobic. The injector capillary surface was modified with trimethoxyphenylsilane. Treatment of a glass slide with this silane resulted in a measured contact angle of 108° (a change of 85° compared with a typical, clean glass surface (Schoukens 2009)) indicating successful surface modification with this technique. However, the surface of the collector capillary was not modified which necessitated an assessment of its impact on the droplet formation process over time. This was done qualitatively by assessing the time required to record noticeable discoloration of the MFD during operation. Figure 4.3 shows the change in the surface from the first use of the microfluidic device to a stained surface after 32 hours of use. Discoloration arises from the deposition of debris and occasional contact with the oil phase which sticks and leaves a thin layer on the collector capillary. Over time (Figure 4.3b) this leads to an alteration of the surface properties such that flow of the oil permanently contacts the collector capillary surface and interrupts the double emulsion formation process. Droplet production rates were typically in the order of 10 - 100 Hz and thus operation over 3 hours was sufficient for the adequate production of the sample for characterisation. Thus surface modification of only the injector capillary was shown to be sufficient for the reliable generation of w/o/w double emulsion droplets over moderate timescales. However, it is important to note the relatively low flowrates of the continuous phase and low droplet production frequency compared with other works which can be in the of 1000 Hz (Zhu & Wang 2017). Such a difference in flow conditions may result in a reduced rate of surface degradation.

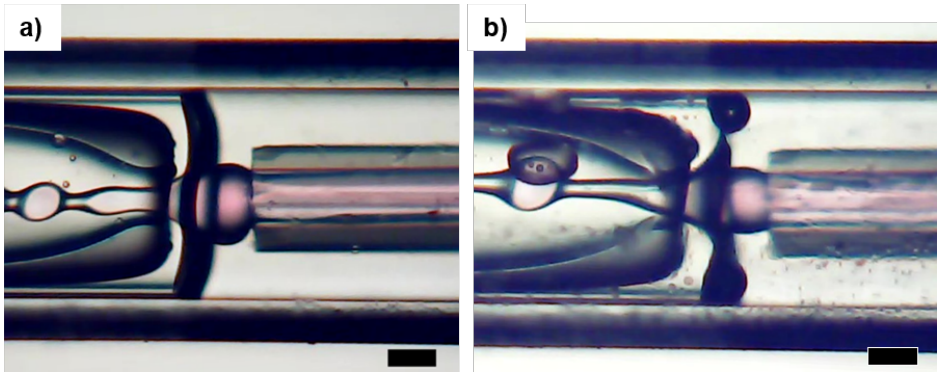

Figure 4.3: a) Flow focusing microfluidic device appearance on first operation after assembly, b) device after approximately 32 hours of operation showing staining on the internal glass surface. The scale-bar is 200 μm in both sub-figures.

4.2 Impact of pumping system on emulsion formation

Control of the droplet formation mode (dripping or jetting) and the droplet morphology (single, double or multi-emulsions) depends on the ability to control the fluid flowrates in the microfluidic system. Defects in the microfluidic pumping system due either to normal wear and tear or low precision mechanics have an impact on the flow control. It is therefore important to characterise the flow behaviour in the microfluidic system as a result of such pumping system limitations.

4.2.1 Inner and middle fluid flow

The pumping system of the microfluidic device consists of three separate syringe pumps running simultaneously (Figure 3.4). Syringe pumps allow for the delivery of a constant flowrate irrespective of the hydrodynamic re-

sistance of the MFD provided the pump pressure rating is sufficiently high. A motor and screw are used to provide the linear motion that drives the syringe piston inwards to generate flow. At low flowrates, the motor step becomes noticeable, manifesting as a pulsed flow in the microfluidic system. The pulsed flow impacts the continuous production of monodisperse emulsion droplets and lowering the system volume was adopted to minimise this effect. However, contribution to pulsing cannot exclusively be attributed to the action of the pump as flexibility of the tubing allows for expansion of the tubing as the pressure rises in the system. The pressure in microfluidic systems can be as high as 500 *bar* (Gothsch et al. 2015) and syringe pumps used in this work can deliver a pressures in excess of 6000 *bar* (PHD Ultra 22/2000, Harvard Apparatus, USA) depending on the capillary dimensions and flowrates used. The PEEK tubing used in this work had a Young's modulus of approximately 3.6 GPa and a variation in the volume of of the tubing with such high deliverable pressures of approximately 0.05% MPa^{-1} can be expected. Thus it was assumed that the tubing elasticity had little effect on the flow variability. Nevertheless, pulsed flow was still observed in the microfluidic flow system indicating that the set pump flowrate was not equivalent to the actual flowrate during droplet production under normal conditions. In addition, observation of the flow during droplet production indicated a periodic disruption of the flow as shown in Figure 4.4 where the middle phase fluid periodically stops flowing followed by the re-establishment of droplet production between these periods.

The pulsed flow can be represented graphically as shown in Figure 4.5 which was obtained by image processing using the Matlab image processing

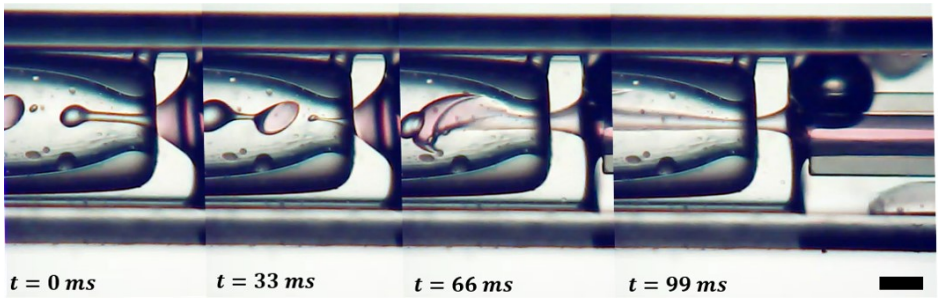

Figure 4.4: Time-lapse images of the variation of the middle fluid flowrate with time in a flow-focusing microfluidic device (frame rate, 30 fps). The inner, middle and outer fluids were LiBr solution (1 $g\ cm^{-3}$), diethane-trione and PEG solution (15$wt\%$, M_n = 20000), respectively with flowrates of 300, 600 and 8000 $\mu L\ hr^{-1}$, respectively. Scale-bar measures 200 μm.

toolbox to determine the number of pixels associated with the middle phase per frame from a recording of the flow process. The pixel area is proportional to the volume of oil and thus represents the flow delivered by the pump. In Figure 4.5, an abrupt drop in the oil flowrate, represented by steep troughs, can be observed associated with a drop in the pump pressure, thus a jet of the inner fluid flows with no capsule formation until the flow of the middle fluid is re-established. Each point in the figure represents a single frame and the average was determined by smoothing with a local regression function (rloess) in Matlab. The duration of droplet production shown in Figure 4.5 is much longer than that of flow disruption and double emulsion droplet production could still be maintained with the production of small oil droplets intermittently.

At higher flowrates of the continuous phase with PFPE-urethane dimethacrylate as the shell phase, a different flow behaviour was observed under droplet-forming conditions as shown in Figure 4.6. During droplet production there is a periodic backflow of the inner fluid into the flow region of the middle

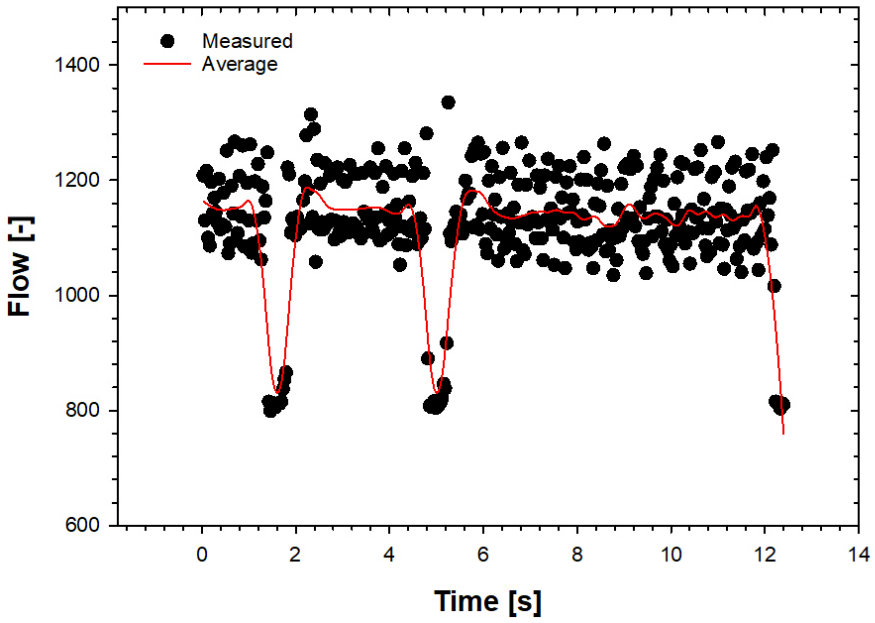

Figure 4.5: Variation of the middle fluid flowrate with time in a flow-focusing microfluidic device. The inner, middle and outer fluids were LiBr solution (1 $g\ cm^{-3}$), DT and PEG solution (15$wt\%$, $M_n = 20000$), respectively with flowrates of 300, 600 and 8000 $\mu L\ hr^{-1}$, respectively.

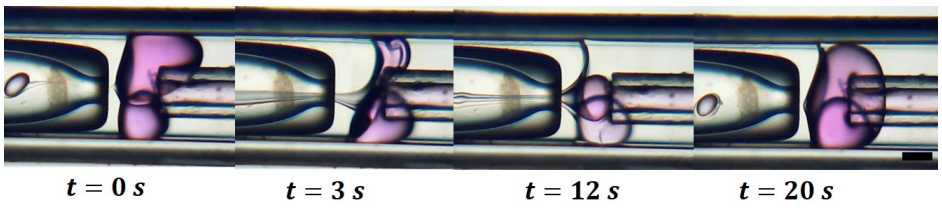

Figure 4.6: Time-lapse images of the variation of the middle fluid flowrate with time in a flow-focusing microfluidic device. The inner, middle and outer fluids were LiBr solution (1 $g\ cm^{-3}$), PFPE-urethane dimethacrylate and PEG solution ($5wt\%$, $M_n = 20000$), respectively with flowrates of 200, 100 and 20000 $\mu L\ hr^{-1}$, respectively. Scale-bar measures 200 μm.

fluid as shown. Backflow results from a pressure difference between the fluid inlets which induces flow from the inner fluid channel to the middle fluid channel. The bulb of inner fluid grows to some maximum value before a jet of the inner fluid breaks through the middle phase. Droplet production is maintained with the middle fluid flowing in the thin boundary layer between the inner fluid and the capillary wall until the jet of inner fluid is formed. For a fluid with a sufficiently low viscosity and low flowrate, such recirculation of the fluid in the region between the injector and collector capillaries was observed for the tip-multi-breaking droplet formation mode (Zhu et al. 2015). However, in this system, larger emulsion droplets are formed in contrast to the much smaller droplets produced in tip-multi-breaking mode.

Figure 4.7 is a graphical representation of the flow behaviour during the bulb growth phase. The figure was obtained in a similar way to that of Figure 4.4. It can be observed that during the bulb growth phase, droplet production is maintained at a steady average value and similar behaviour is shown in Figure 4.4 where the droplet production between troughs is relatively stable. The two examples of flow disruption discussed indicate that droplet produc-

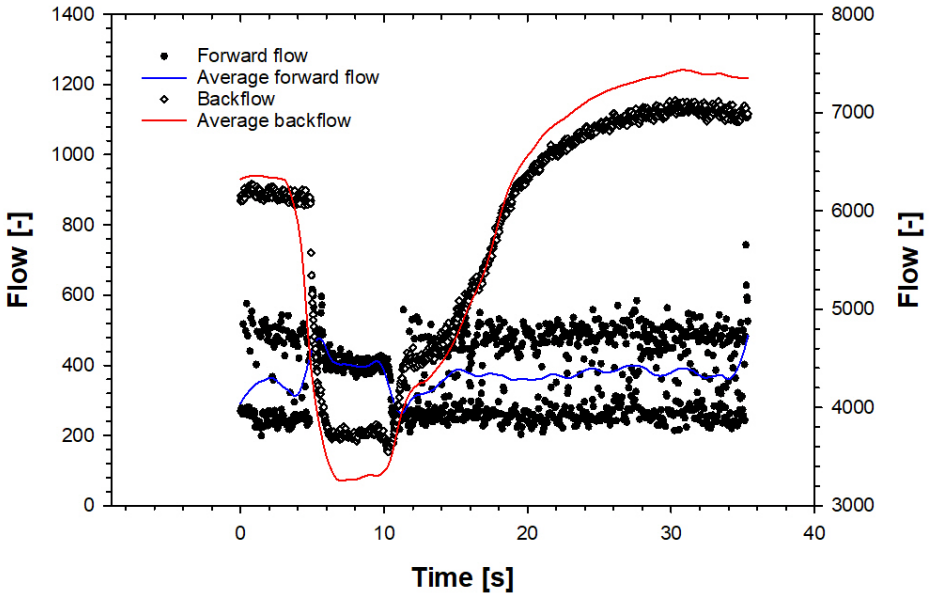

Figure 4.7: Variation of the forward flow and backflow of the middle fluid flowrate with time in a flow-focusing microfluidic device. The inner, middle and outer fluids were LiBr solution (1 $g\ cm^{-3}$), PFPE-urethane dimethacrylate and PEG solution ($5wt\%$, $M_n = 20000$), respectively with flowrates of 200, 100 and 20000 $\mu L\ hr^{-1}$, respectively.

tion was not severely affected affected by the pumping systems. However, the results show that the true flowrate in the system is different to that set in the syringe pumps. Since an adequate description of the phase diagram of the microfluidic devices in this study requires knowledge of the true fluid flowrates, a flow correction method based on image analysis was utilised to estimate the true fluid flowrates (Section 4.2.2).

4.2.2 Flow correction method

Given the uncertainty in the average flowrate of the middle and inner fluids due to the observed flow behaviour (Figure 4.4 - 4.7), an image-based method

was used to estimate the flowrates of the inner and middle fluids from videos of the encapsulation process in the dripping regime. An average droplet size and frequency were determined by analysing each frame. Average size data obtained from optical micrographs allowed the volume of the middle (V_{oil}) and inner (V_{core}) fluid phases to be determined per emulsion droplet to determine the flowrate of the inner and middle fluids from the products $V_{core} \times F$ and $V_{oil} \times F$,respectively, where F is the frequency of droplet generation. The average difference between the calculated and set flowrates of the inner and middle fluids were 28% and 31%, respectively, with minimum to maximum ranges of 3 - 62% and 2 - 65%, respectively (See Appendix for complete values). The calculated flowrates show good agreement with observed droplet formation modes and empirical model predictions by Nabavi & Vladisavljević (2017) as detailed in Section 4.3.

4.3 Droplet formation modes

The generation of a microfluidic device phase diagram was introduced as a useful method for describing the different regions of droplet formation modes based on device geometry, fluid flow and properties in Chapter 2. In this section, a similar phase diagram is presented and observed dripping-to-jetting transition data compared with literature models.

4.3.1 Predictable dripping and jetting

In-order-to obtain emulsion droplets with a uniform size distribution, droplet production in the dripping regime is required. This is the condition where

the capillary number of the continuous phase and the Weber number of the dispersed phase or the sum of the two, are less than one (Utada et al. 2007). Alternatively, this is when the empirical parameter $log\zeta > 5.7$ (see Equation 4.8 later)as defined in the work of Nabavi & Vladisavljević (2017). By varying the flowrate of the three fluids, the conditions of operation of a particular MFD can be determined for the dripping and jetting regimes as well as for double and multi-core emulsion production. Variation of the ratio of the inner and outer fluids also determines the shell thickness of the final microcapsule product.

In this study, the capillary numbers (Ca) used for the three phases were calculated according to Equations 4.1 - 4.3 as in the work of Nabavi & Vladisavljević (2017) due to the similar device geometry to that used in this work (Figure 4.8).

$$Ca_1 = \frac{\mu_1 \overline{u}_1}{\gamma_{12}} \tag{4.1}$$

$$Ca_2 = \frac{\mu_2 \overline{u}_2}{\gamma_{23}} \tag{4.2}$$

$$Ca_3 = \frac{\mu_3 \overline{u}_3}{\gamma_{23}} \tag{4.3}$$

In Equations 4.1 - 4.3 the subscripts 1, 2 and 3 three refer to the inner, middle and outer fluids, respectively, μ is the dynamic viscosity and γ is the interfacial tension at the interface of the two phases indicated by the subscript. The corresponding average velocities ($\overline{u}$) are defined in Equations

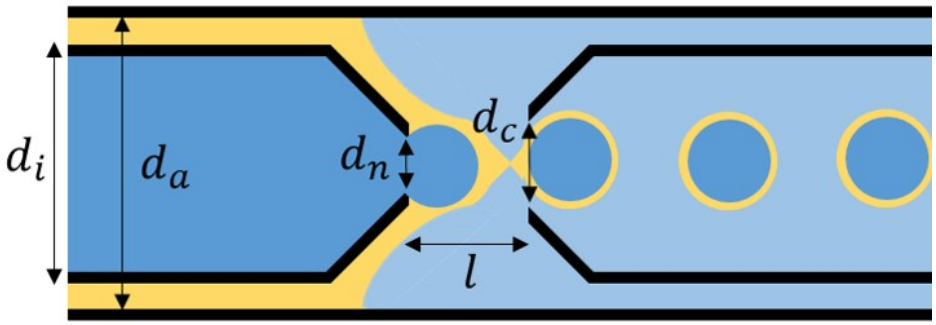

Figure 4.8: Schematic of microfluidic device showing model parameters, adapted from Nabavi & Vladisavljević (2017)

4.4 - 4.6,

$$\overline{u}_1 = \frac{4Q_1}{\pi {d_n}^2} \tag{4.4}$$

$$\overline{u}_2 = \frac{Q_2}{{d_a}^2 - {d_i}^2} \tag{4.5}$$

$$\overline{u}_3 = \frac{Q_3}{{d_a}^2 - {d_i}^2} \tag{4.6}$$

where Q is the volumetric flowrate, d_n and d_i are the inner and outer width of the injector capillary, respectively and d_a is the internal width of the alignment capillary, as illustrated in Figure 4.8.

As previously mentioned in Chapter 2 dripping to jetting transition can be described by the Capillary number or the Weber number depending on the governing mechanism. When the viscous drag of the outer fluid is large with

respect to the interfacial tension, the capillary number is a useful descriptor. On the other hand, when the inertial forces of the inner fluid are large with respect to the interfacial forces, the Weber number is a more useful descriptor. Figure 4.9 shows the dripping and jetting regimes in relation to the capillary number of the continuous phase and the Weber number of the internal phases. This figure represents the working region of the microfluidic devices used in this work. It can be seen that above a capillary number of 0.005 and a Weber number of 0.001, double emulsion formation occurred in the jetting regime. The Weber number (Table 2.2) of the compound jet is calculated assuming a volume weighted density of the inner and middle phases. The characteristic length is taken as the thread thickness d_{thread} of the compound jet given by Equation 4.7 as in the work of Erb et al. (2011),

$$d_{thread} = d_c \sqrt{\frac{Q_1 + Q_2}{Q_1 + Q_2 + Q_3}} \tag{4.7}$$

where the nomenclature is as previously described. Figure 4.9 shows that jetting was observed in the region where $Ca + We < 1$, in contrast to observations by Utada et al. (2007). However, this could be explained by the low accuracy in determining the fluid velocities in the jetting regime.

Alternatively, the flow phase diagram can be represented in terms of the empirical parameter ζ (Equation 4.8) developed in the numerical study by Nabavi & Vladisavljević (2017) and was demonstrated to be applicable to a wide range of flow conditions and fluid properties. This empirical parameter ζ is defined as in Equation 4.8,

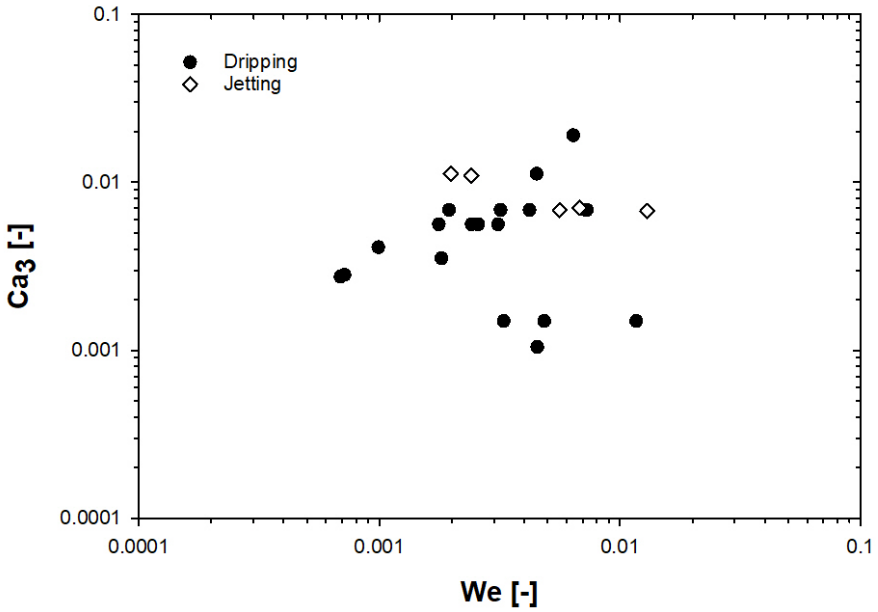

Figure 4.9: Dripping and jetting regimes of droplet production as a function of the continuous phase Capillary number and the Weber number of the combined middle and inner phases.

$$\zeta = \frac{Ca_1^{0.254}}{Ca_2^{0.567} Ca_3^{1.12}} (\frac{d_c}{d_n}) \tag{4.8}$$

where d_c, is the inlet diameter of the collector capillary and all other terms were previously defined.

Values of $log\zeta > 5.7$ fall in the dripping regime as described by Nabavi & Vladisavljević (2017) and are also consistent with observations as in Figure 4.10. This validates the method of estimation of the flowrates by image processing. Using the set flows for the syringe pumps would predict much lower values of $log\zeta$, incorrectly implying that droplet formation occurred in the dripping regime for the majority of samples. There are a few outlying values observed to be in the dripping regime but falling in the jetting region of the graph and this is related to the difficulty in determining the true fluid flowrate in the jetting regime when using the imaging technique.

4.3.2 The decussate droplet formation regime

At low or comparable flowrates of the inner fluid with respect to the middle fluid, a situation arises where single droplets of the middle phase are formed periodically in alternation with double emulsion droplets. This regime of emulsion droplet formation is observed at low Weber numbers and was termed the "decussate" regime by Azarmanesh et al. (2016). This provides a useful method to produce "binary particles" under the same flow conditions. The formed single and double emulsion droplets can be polymerised to form microcapsules and polymer particles of the shell material. This is an advantageous process in studying the mechanical properties of the microcapsule

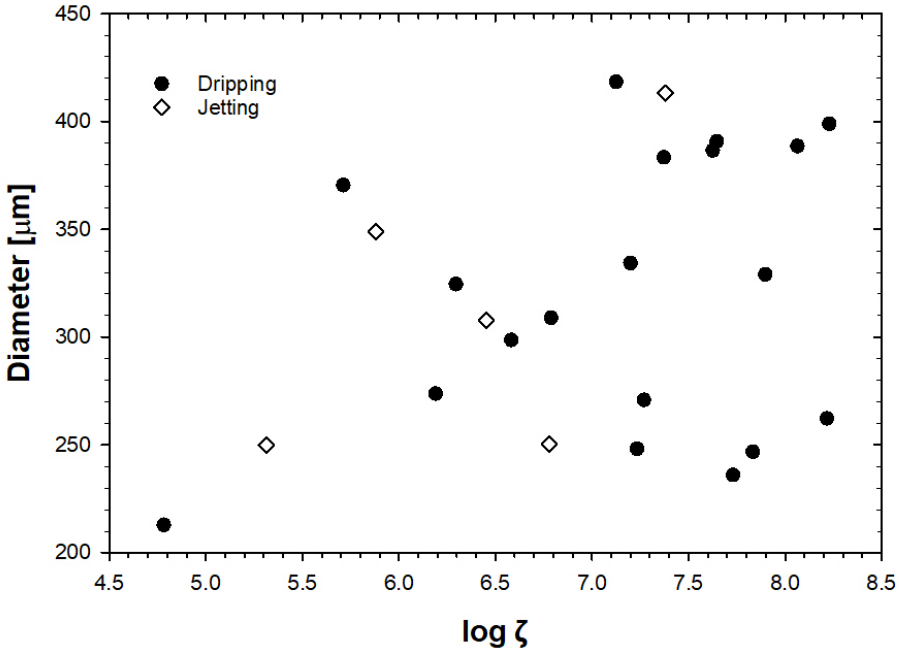

Figure 4.10: Microcapsule diameter versus *log* ζ.

shell by micromanipulation as the polymer particles and microcapsules are exposed to the same conditions (continuous phase, UV exposure time and work-up) and can be investigated separately. Thus, an investigation into the influence of the flow parameters, in terms of the Capillary numbers, on the decussate regime is presented in this section.

The decussate droplet formation process is shown sequentially in Figure 4.11. A leading tip of the compound jet of the middle and inner fluids first enters the collector capillary. The tip consists only of the middle fluid and extends further into the collector capillary whilst the inner fluid trails behind in a jet surrounded by a thin film of the middle fluid. The tip of middle fluid forms a bulbous end of increasing surface area. Necking occurs on the leading edge and a droplet of the middle fluid detaches from the compound jet followed by the detachment of the larger double emulsion drop. The inner fluid droplets grows into a large size before breakage due to low shear from the middle fluid. The formed double emulsion drop is not symmetric and the middle fluid is concentrated at the leading edge of the droplet.

Figure 4.11 shows the changes in the decussate regime as the value of Ca_2 is increased at a fixed value of $Ca_3 = 6.9 \times 10^{-3}$. The value of Ca_2 was increased from 1.0×10^{-4} to 3.1×10^{-4} by increasing the volumetric flowrate of the middle phase. The flowrate of the inner phase had a We_1 less than 0.001 in all cases. For all cases $log\zeta > 5.7$, indicating dripping, as verified by the images in right of Figure 4.11.

In Figure 4.11(a), a single oil droplet is formed in the decussate mode. The oil droplets had an average diameter of 272 μm whereas the double emulsion droplets were larger, with an average diameter of 463 μm. At a

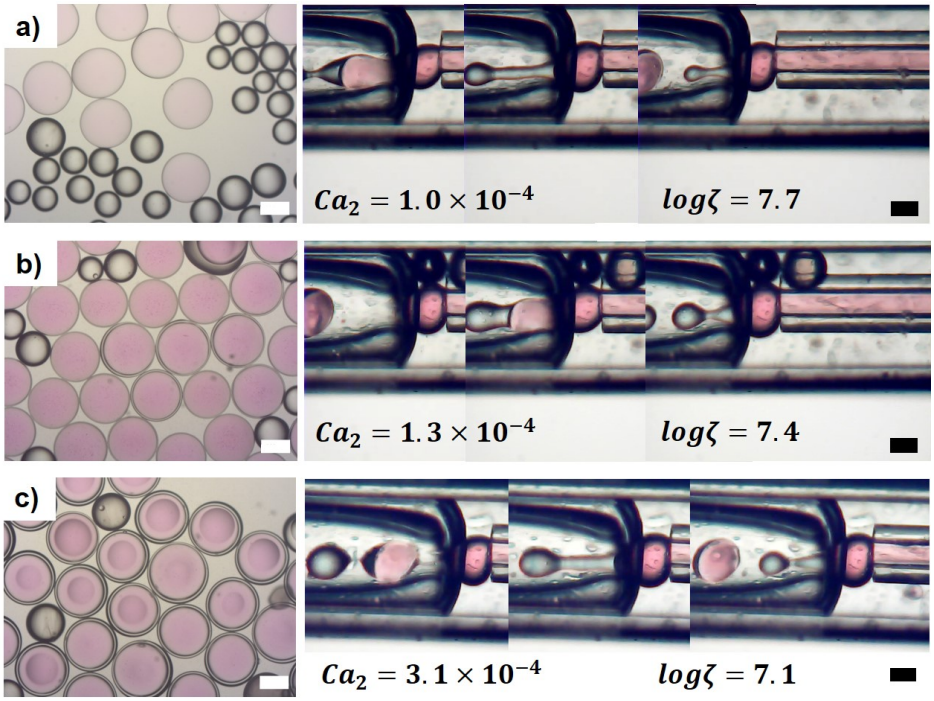

Figure 4.11: Variation in the size of oil droplets of DT in the decussate regime with the capillary number of the middle fluid. Scale bar is 200 μm.

Ca_2 value of 1.3×10^{-4}, two oil droplets of comparable size are formed by breaking off, one after the other, at the orifice followed by a double emulsion droplet of approximately twice the average diameter of the oil droplets at 383 μm (Figure 4.11(b). This trend has been observed in the numerical work of Azarmanesh et al. (2016) which the results show can be achieved by increasing the value of Ca_2.

In Figure 4.11(c), at the higher value of $Ca_2 = 3.1 \times 10^{-4}$, a section of the middle fluid with a tail consisting of the inner fluid detaches from the inlet capillary, breaking at two points simultaneously; this occurs at both ends of the double emulsion drop and an oil droplet and a double emulsion droplet are formed. A higher value of Ca_2 indicates a lower velocity difference between the middle and outer phases, which gives rise to a lower viscous force exerted on the middle phase, this increases the pinch-off time of the middle fluid, thus, as shown Figure 4.11(c), the pinch-off times of the oil droplet and double emulsion are approximately equal and only a single oil droplet is formed at a time. Similar observations were made in the work of Wang et al. (2020) where the two droplets were formed from the breakup of a larger detached filament resulting in two droplets of discernibly different sizes. The results show that the oil droplet number and size can be controlled by adjusting the value of Ca_2 whilst maintaining constant values of Ca_1 and Ca_3.

At inner, middle and outer fluid flowrates of 500, 500 and 5000 $\mu L\ hr^{-1}$, respectively, the resulting oil droplet decelerated in the collector capillary tube which allowed them to catch-up and coalesce with the double emulsion drops to form multi-core rods as shown in Figure 4.12. Such rod-like

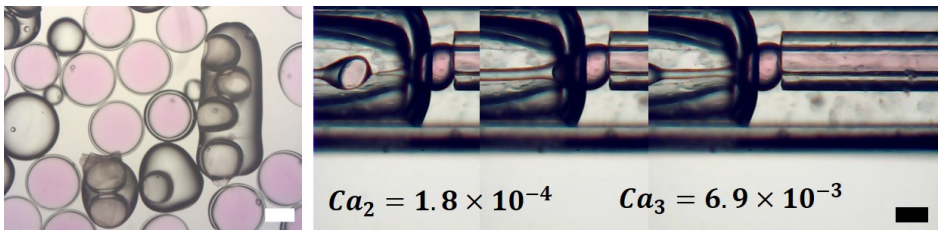

Figure 4.12: Formation of polymerised rods due to double emulsion droplet coalescence at flowrates of 500, 500 and 5000 $\mu L\ hr_{-1}$ for the inner, middle and outer fluid flowrates, respectively. Scale bar is 200 μm.

structures produced by microfluidics were demonstrated by Gokmen et al. (2009) using high internal phase emulsions (HIPEs) with envisaged potential for applications in separation and catalysis processes.

Figure 4.13 shows changes in the droplet production behaviour in the decussate mode when both Ca_2 and Ca_3 are varied. The values of Ca_2 and Ca_3 were varied in the range 1.0×10^{-4} to 3.1×10^{-4} and from 1.0×10^{-4} to 3.1×10^{-4}, respectively. The flowrate of the inner phase had a We_1 less than 0.001 and the $log\zeta > 5.7$ in all cases. Figure 4.13(a) shows the droplet formation at $Ca_2 = 1.2 \times 10^{-4}$ and $Ca_3 = 2.7 \times 10^{-3}$. Pinch-off of the oil and double emulsion droplets occurs in a similar manner to that observed in Figure 4.11. The oil droplet had a diameter of 317 $\mu\ m$ and the double emulsion droplet was 399 $\mu\ m$ in diameter. At a low Ca_3, the difference in velocities of the middle and outer phases is reduced leading to a reduction in the shear stress allowing droplets to grow to a larger size before break-off. Additionally, in these conditions, a single oil droplet is formed of equivalent size to the double emulsion droplet. This is in contrast to droplets formed in Figure 4.13(b) where the oil droplets are of a smaller size compared to the double emulsion droplets. Commonly, up to two oil droplets have been

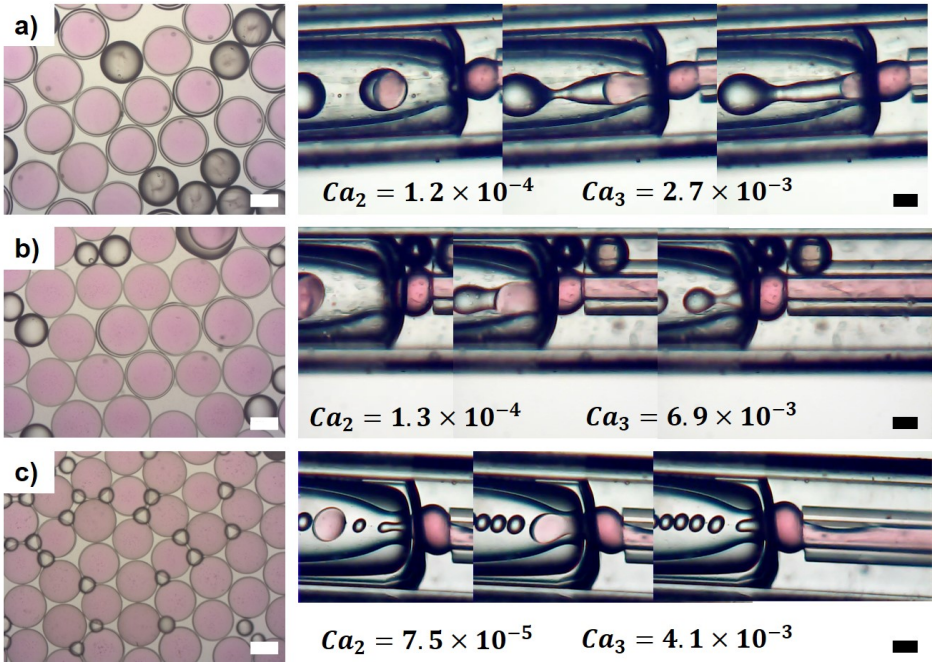

Figure 4.13: Changes in the decussate droplet production behaviour with the variation of Ca_2 and Ca_3. Scale bar is 200 μm.

reported in the decussate regime, however, at a much lower Ca_2 value of 7.5×10^{-5} and with $Ca_3 = 4.1 \times 10^{-3}$, five oil droplets break off before a larger double emulsion droplet is formed as shown in Figure 4.13(c). The oil droplets have a diameter size of 118 μm and double emulsion drop size of 329 μm. A low Ca_2 value corresponding to a low middle phase velocity, implies a higher shear by the continuous phase which leads to a smaller droplet size of the oil drops, however, total oil volume between compound drops is 4.3×10^{-3} μL, with an equivalent volume diameter of 202 μm. Thus the volume of the large oil droplet in Figure 4.13(a) is not conserved in Figure 4.13(c).

The larger oil phase diameter at higher values of Ca_2 can be explained by increased filling of the oil droplet prior to pinch-off due to higher inertia

of the middle phase. Another case is where the middle fluid flows at a lower flowrate relative to the inner fluid. The droplet size of the oil droplets is smaller than that of the double emulsion droplets and thus a different shearing area governs the droplet break-up in each case. The results show that combining high values of Ca_3 and low values Ca_2 smaller oil droplets can be formed compared with the double emulsion droplets which allows for simple separation downstream on the basis of size.

Accounting for mismatch between diameter ratios and flow ratios

Provided droplet production occurs in the dripping or decussate regime of a microfluidic phase diagram, it may be desirable to adjust the fluid flows to optimise rate of production of double emulsion droplets of a specific diameter. In the dripping regime, for a known droplet diameter and middle phase thickness, this can be determined from as mass balance as in the work of Erb et al. (2011).

For the case where there is a simultaneous production of double emulsion droplets of diameter D_{cap} and oil droplets of diameter D_{oil}, the relationship between the droplet diameters and the flowrates can be expressed according to Equation 4.9,

$$\frac{\frac{F_{oil}}{F_{cap}}{D_{oil}}^3 + {D_{cap}}^3}{{D_{core}}^3} = \frac{Q_1 + Q_2}{Q_1} \tag{4.9}$$

where D_{core} is the double emulsion core diameter, F_{oil} and F_{cap} are the frequencies of oil and double emulsion droplet generation, respectively.

In the particular case where the frequency is lower than the frame rate,

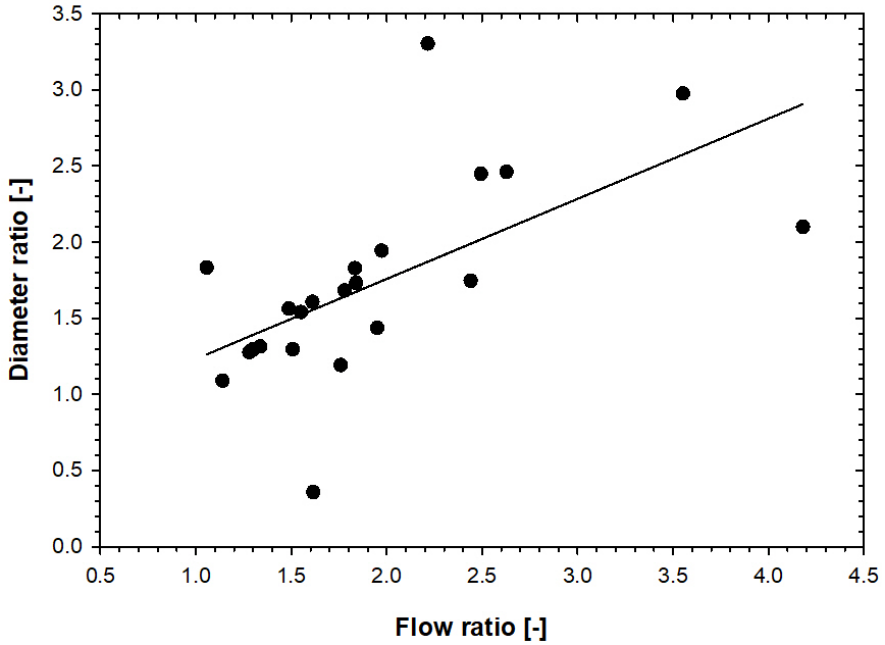

Figure 4.14: Comparison of diameter ratio to flow ratio of middle phases in microfluidic device.

the droplet production frequency can be determined via image processing. The relationship between the ratio of diameters and the ratio of the middle and inner fluid flowrates as expressed in Equation 4.9 is shown graphically in Figure 4.14. This equation accounts for the excess oil drops but still assumes that the inner and middle phases are pinched at the same time to form the double emulsion droplet. This difference in formation time can lead to discrepancies with the prediction as represented by outliers. Greater agreement with the mass balance line is obtained at lower flow-ratios, however, at higher flow-ratios, formation time and instabilities on transition to jetting affect the measurement accuracy as reflected by the greater discrepancy in the figure.

4.3.3 Control of droplet size and morphology

A key advantage of producing emulsion droplets with microfluidics is that it allows for greater control of emulsion droplet size compared with other techniques summarized in Chapter 2. Varying the flowrate of the continuous phase varies the viscous drag on the forming double emulsion droplets. This leads to a reduction in the pinch-off time of the compound jet of the middle and inner phases and consequently, a reduction in the droplet size. As shown in Figure 4.15, a general reduction in the droplet size with an increase in the continuous phase flowrate is observed irrespective of the fluid combinations used. This is in agreement with the experimental and theoretical work of Utada et al. (2005). Results indicate large emulsion droplet formation at flow ratio values below 10 and a reduction to a size comparable to the collector capillary orifice diameter at higher values of the flow ratio. Further reduction of the droplet size in the dripping mode can be attained by increasing the viscosity of the outer phase relative to the middle phase. This increases the viscous drag on the emulsion droplets leading to the break-off of smaller emulsion droplets (Chen et al. 2015). However, in the current system, droplet production would occur at higher frequencies which require an optical set-up that can operate at higher frame speeds. At higher flowrates of the continuous phase with respect to the dispersed phases, droplet formation occurs in the jetting regime. The sporadic droplet formation in the jetting regime leads to significant polydispersity in the droplet size distribution.

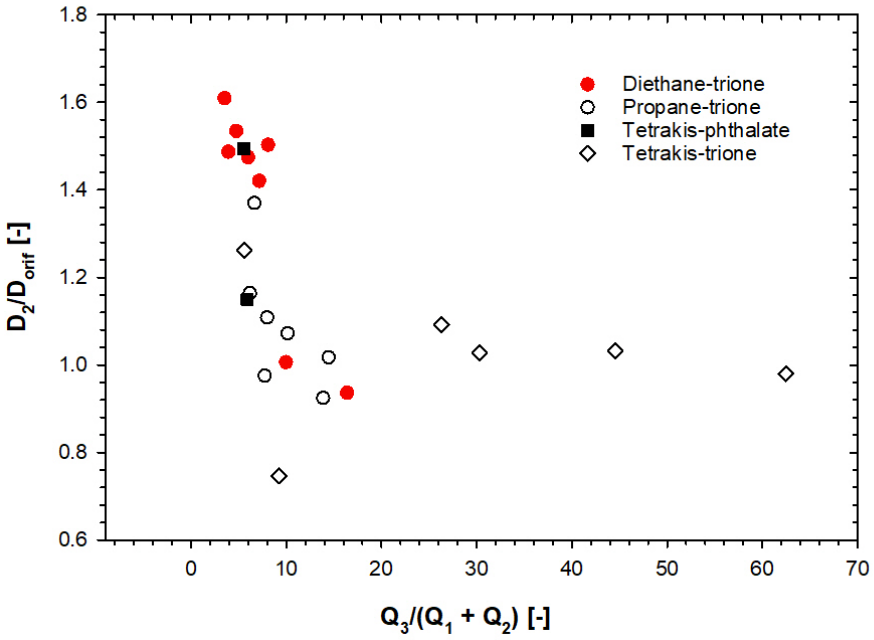

Figure 4.15: Variation of the normalised droplet diameter with the normalised continuous phase flowrate.

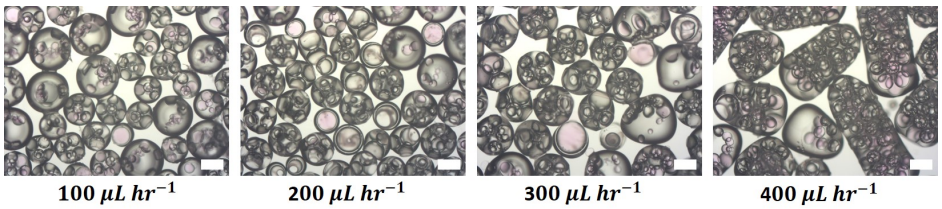

Figure 4.16: Multi-core droplets produced at varying middle phase (TT) flowrates (shown) and inner (aqueous LiBr) and outer fluid ($5wt\%$, M_n = 20000) flowrates of 200 $\mu L\ hr^{-1}$ and 5000 $\mu L\ hr^{-1}$, respectively.

Multicore microcapsules

The main focus of this work is on the production of microcapsules with the core-shell geometry. However, the multi-core geometry can be important in cases where higher strength is desired even though such microcapsules generally have lower loading capacities compared with core-shell microcapsules. Thus, multi-core droplet formation was also investigated with the device and different multi-core geometries were obtained by varying the flowrate of the oil phase whilst maintaining the inner and outer fluid flowrates constant, as shown in Figure 4.16. As the oil phase is increased from 100 $\mu L\ hr^{-1}$ to 400 $\mu L\ hr^{-1}$, the size of droplets increases until rod-like structures are formed. A lower outer fluid flowrate compared with earlier results ensured a delayed break-up of the middle phase fluid compared with the inner fluid phase. Thus multiple droplets of the inner fluid are formed within the middle phase droplet.

Microcapsules with a heterogeneous shell

An additional morphological property of microcapsules that is affected by the device flow conditions is the shell homogeneity/heterogeneity. Spatial varia-

tion of the shell thickness can occur in core-shell microcapsules as a result of the density difference between the core and shell phases of double emulsion droplets prior to polymerisation of the shell. The lighter phase gradually rises causing a thinning and thickening of the shell phase at opposite ends of the emulsion droplet under gravity. This phenomenon was employed by Datta et al. (2012) to control the degree of shell heterogeneity by varying the time double emulsion drops were allowed to settle before polymerisation. Alternatively, Zhang et al. (2019) varied the flow ratio of the inner and middle phases in a flow focussing MFD to control the degree of heterogeneity in the microcapsule shell. Considering that the density-driven effects in the shell can be represented the gravitational force given by $\Delta\rho gL$ (where $\Delta\rho$ is the fluid density difference, g is the acceleration due to gravity and L is the characteristic length) and the hydraulic resistance can be approximated by that of a planar geometry, infinitesimally extended as $12\eta/L^3$ (Rapp 2017*b*), (where η is the fluid viscosity) the ratio of these forces is $\sim \mathcal{O}(L^4)$. Thus, for the case where the double emulsion drops produced are immediately polymerised whilst flowing in the collector capillary, the contribution of the density difference to the degree of inhomogeneity is expected to be minimal. The timescale for photopolymerization of the shell (in the order of milliseconds) is much smaller than the time to flow through the collector capillary. Thus a more suitable explanation for the heterogeneous shells observed in microcapsules produced in this work is that the thicker leading edge of the middle fluid described in Section 4.3.2 (Figure 4.11) is polymerised, fixing the geometry and preventing any middle phase fluid rearrangement as shown in Figure 4.17(a). However, for thin-shelled microcapsules, the heterogeneity is min-

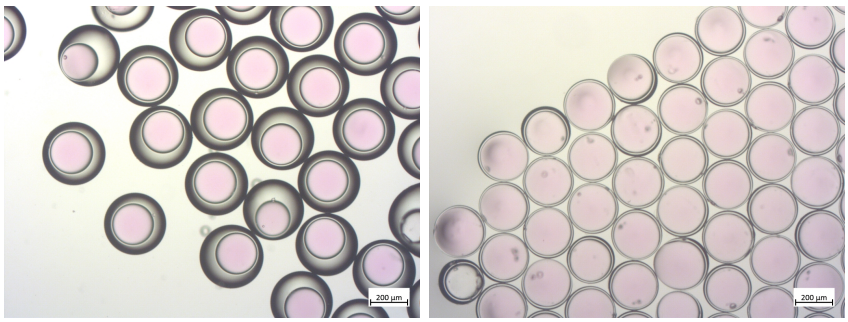

(a) PT microcapsules with heterogeneous shell. The inner, middle and outer fluids were LiBr solution (1 $g\ cm^{-3}$), PT and PEG solution (15$wt\%$, M_n = 20000), respectively with flowrates of 300, 250 and 2500 $\mu L\ hr^{-1}$, respectively.

(b) PT microcapsules with uniform shell. The inner, middle and outer fluids were LiBr solution (1 $g\ cm^{-3}$), PT and PEG solution (15$wt\%$, M_n = 20000), respectively with flowrates of 300, 300 and 5000 $\mu L\ hr^{-1}$, respectively.

Figure 4.17: PT microcapsules with a heterogeneous (a) and uniform (b) shell.

imised as shown in Figure 4.17(b). Microcapsules with a heterogeneous shell have regions with low mechanical strength and as the mechanical strength is governed by the weakest point, this can have a significant impact on the overal microcapsule performance. Therefore possible mitigation steps to be considered on the basis of the results would be to delay the polymerisation to allow for fluid re-distribution.

4.4 Summary

The design of a glass capillary, flow-focusing microfluidic device using prefabricated glass capillaries and 3D-printed connectors was presented. The design was shown to reduce fabrication times and improve reproducibility of the microfluidic devices. This was achieved by eliminating the time-consuming and

laborious step of glass capillary pulling and grinding required with conventional glass capillary microfluidics. The devices were tested under a range of flow conditions with a variety of fluids to generate w/o/w double emulsions with a photopolymerisable oil phase. Successful emulsion droplet formation was demonstrated with various droplet morphologies such as core-shell, multi-core and rod-like structures obtained by varying the flowrate.

Image analysis techniques were used to characterise the flow system used to generate emulsion droplets. It was found that variation in the delivered flow by the syringe pumps system led to differences between the set and actual flowrates of the middle and inner fluids of an average of 30%. However, droplet production was maintained and allowed for the microfluidic device phase diagram to be determined based on values of the estimated true flowrate determined by image analysis. Furthermore, the dripping and jetting droplet formation modes in the microfluidic device were shown to be in good agreement with the semi-emipirical predictions of Nabavi & Vladisavljević (2017). The emulsion droplet size was also shown to be controlled by the flow ratio of the outer fluid flowrate to the sum of the inner and middle fluid flowrates. The results were in agreement with findings by Utada et al. (2005) where the droplet size reduced with an increase in the flow ratio.

The decussate droplet formation mode was introduced as a method for producing double emulsion and single emulsion droplets simultaneously. These emulsion droplets can then be polymerised to form microcapsules and solid sphere particles. By varying the Capillary number of the middle fluid (Ca_2) whilst holding Ca_1 and Ca_3 constant, it was shown that the frequency of the single emulsion droplets could be controlled. Increasing values of Ca_2

changed the number of oil droplets produced from one to two droplets per double emulsion droplet. A further increase in Ca_2 from 1.3×10^{-4} to 3.1×10^{-4} lead to the formation of single and larger double emulsion droplets, once again, however, with pinch-off of both the single and double emulsion droplets occurring simultaneously. It was suggested that this was due to reduced viscous effects of the outer fluid at higher Ca_2 resulting in similar pinch-off times for both emulsion drops. Further variation of Ca_2 and Ca_3 showed that the size and number of single emulsion droplets could be reduced and increased, respectively, for the cases where Ca_3 is approximately an order of magnitude greater than Ca_2. These findings are useful for the study of the mechanical properties of microcapsules by compression as the bulk properties of the shell can be determined separately from the polymer particles.

Finally, it was observed that some of the formed microcapsules displayed significant shell heterogeneity due to an off-centre core. Analysis of the droplet formation process was used to show that this property arose from a thicker leading edge of the middle phase in the double emulsion droplet during flow which is rapidly polymerised on exiting the microfluidic device. Additionally, it was shown that this effect was minimised in cases where the middle fluid volume was much smaller than the core fluid volume. Thus, shell heterogeneity may be reduced by lowering the middle phase flowrate for the case where thin-walled core-shell microcapsules are desired or the photopolymerization step delayed to allow for fluid re-distribution.

CHAPTER 5

Results and Discussions II: Water vapour transport and mechanical properties of thiol-ene microcapsules

In this chapter, the size and wall thickness distribution of thiol-ene microcapsules with a water core are characterised using optical microscopy. Additionally, a combination of time-lapse microscopy and thermogravimetric analysis was used to study the water vapour transport properties and buckling of microcapsules under isothermal conditions. Micromanipulation was utilized to perform compression tests and compression to rupture tests on the microcapsules and polymer particles of the corresponding shell materials. Their mechanical strength parameters were subsequently characterised and the applicability of existing models to describe the deformation and intrinsic material properties discussed. Three thiol-ene shell materials formed of di-, tri- and tetrafunctional thiol monomers with a trifunctional alkene were used in this study to investigate the influence of polymer permeability and

glass transition temperature on the mechanical deformation of solvent-filled microcapsules. The glass transition temperature of the three shell material types, produced as thin films, were characterised by differential scanning calorimetry.

5.1 Morphology and size distribution

5.1.1 Microcapsule size and shell thickness distribution

Microcapsules of three types of shell material were produced from the photopolymerization of the thiol-ene resins of the thiols pentaerythritol tetrakis(3-mercaptopropionate), trimethylolpropane tris(3-mercaptopropionate), 2,2'-(Ethylenedioxy)diethanethiol in combination with the alkene 1,3,5-tri-allyl-1,3,5-triazine-2,4,6(1H,3H,5H)-trione to form the shell material TT, PT and DT in this work (Section 3.1.3). Four batches of microcapsule were produced, two of which had shell material TT and named TT1 and TT2. As discussed in Chapter 4, variation of the flowrate in the microfluidic device leads to a variation in the size distribution of the microcapsules produced as well as the shell thickness. Figure 5.1 to Figure 5.4 show the size distribution data and optical images of the microcapsules studied in this work. Size data are presented on a mass fraction basis by determining the volume of the core and shell (known density) of each capsule from optical images and the corresponding average shell thickness ratio (h/R) for each bin size is calculated using Equation 3.1. Pulsed flow in the syringe pump system led to unsteady flows in the microfluidic device giving rise to broader size

distributions highlighted by the span values, however, the CV values for all capsules fall under 10%, accepted as the criterion for monodispersity for most microparticles (De La Vega et al. 2013) and indicate that the flow variation in the microfluidic system had only a minor impact on the microcapsule monodispersity. The values of the coefficient of variance (CV) and span of DT and PT microcapsules show the greatest distribution spread with CV and span values of 9.4% and 22.8% for DT microcapsules, respectively and 8.5% and 27.5% for PT microcapsules, respectively. TT microcapsules were more monodisperse with CV and span values of 3.0% and 6.5%, respectively for TT1 microcapsules and 3.2% and 7.9%, respectively for TT2 microcapsules. Different bin sizes were used for the different microcapsule size distributions in order to more effectively reveal the skewness of the distributions. This was primarily due to variation in the spread of the size distribution data as reflected in the CV values and minimum-maximum ranges for each microcapsule type. As such a binning algorithm (SigmaPlot®) which minimises the differences in available binning methods such as those by Scott (1979) and Sturges (1926) was employed. Figure 5.1 shows that DT microcapsules with the highest mass fraction also have the lowest values of thickness ratios of around 0.1 whilst Figure 5.2 and Figure 5.3 show a decrease in the relative shell thickness with an increase in the diameter of the PT and TT1 microcapsules, respectively. The thickness ratio results demonstrate that the impact of flow variation in the microfluidic system has a greater impact on the shell thickness uniformity and distribution with particle size. However, in Figure 5.4, the relative shell thickness of the TT2 is shown to have little dependence on the microcapsule size, this indicates that the ratio of the flowrates of the

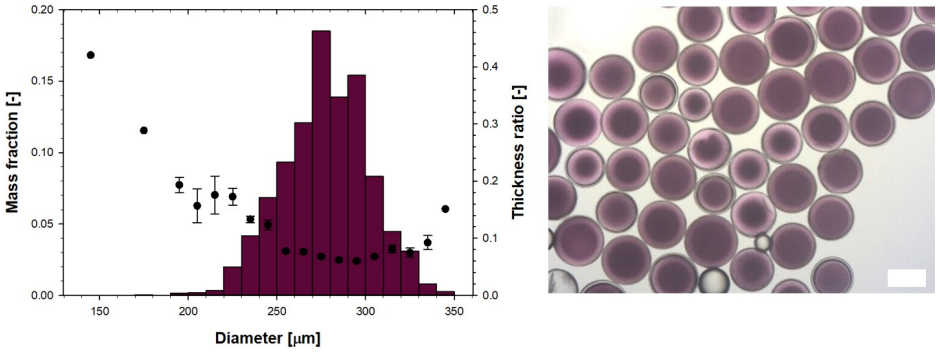

Figure 5.1: DT microcapsule size and thickness ratio distribution (left) with an optical micrograph of the microcapsules in water (right). Microcapsules were formed at flows of 300, 300 and 5000 $\mu L\ hr^{-1}$ of the inner, middle and outer fluids, respectively. The scale bar represents a length of 200 μm.

inner and outer fluids was relatively constant during the emulsification step in the microfluidic device. The PT microcapsules had the largest average diameter 332.3 $\pm$ 1.3 μm followed by the DT, TT1 and TT2 microcapsules with $d_{4,3}$ values of 277.8 $\pm$ 1.0 μm, 260.1 $\pm$ 0.5 μm and 231.3 $\pm$ 0.4 μm, respectively.

Another important property in relation to the shell-thickness, is the shell inhomogeneity which affects the mechanical properties of the microcapsule in that a microcapsule under compression is most likely to fail by rupture at the thinnest part. Shell inhomogeneity has been quantified in this work as the ratio of the maximum thickness to the minimum thickness as illustrated in Figure 3.6. The variation of the shell inhomogeneity with the microcapsule diameter is presented in Figure 5.5 for the microcapsules in this study. The bimodality in the PT microcapsule size distribution observed in Figure 5.2 is also evident in the thickness inhomogeneity values as the larger microcapsules in the batch had similar degree of shell inhomogeneity whilst microcapsules

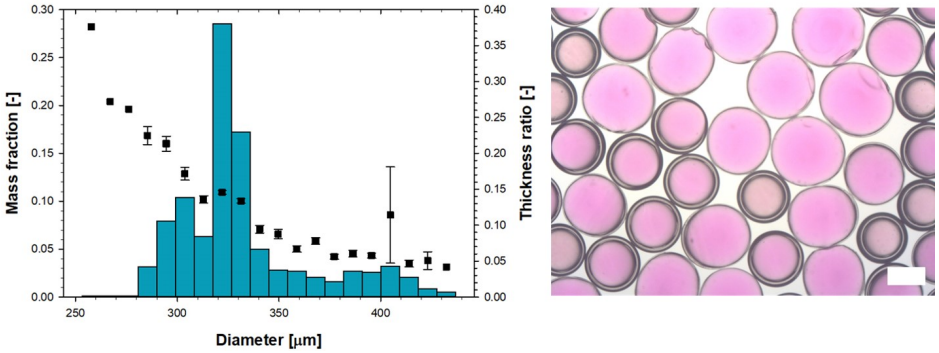

Figure 5.2: PT microcapsule size and thickness ratio distribution (left) with an optical micrograph of the microcapsules in water (right). Microcapsules were formed at flows of 400, 300 and 5000 $\mu L\ hr^{-1}$ of the inner, middle and outer fluids, respectively. The scale bar represents a length of 200 μm.

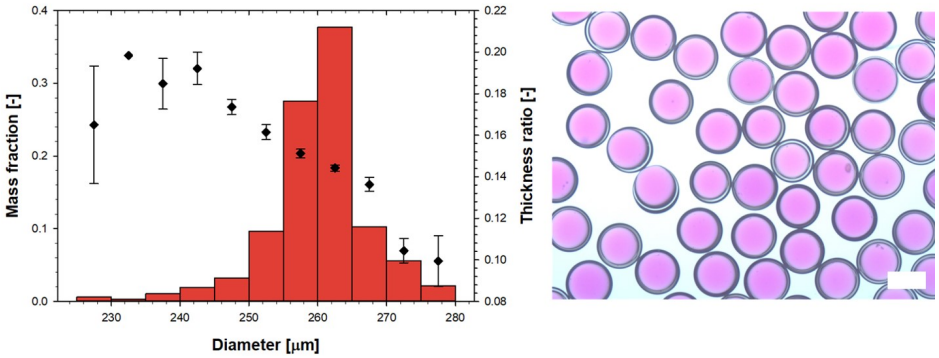

Figure 5.3: TT microcapsule size and thickness ratio distribution (left) with an optical micrograph of the microcapsules in water (right) for the sample TT1. Microcapsules were formed at flows of 300, 200 and 9000 $\mu L\ hr^{-1}$ of the inner, middle and outer fluids, respectively. The scale bar represents a length of 200 μm.

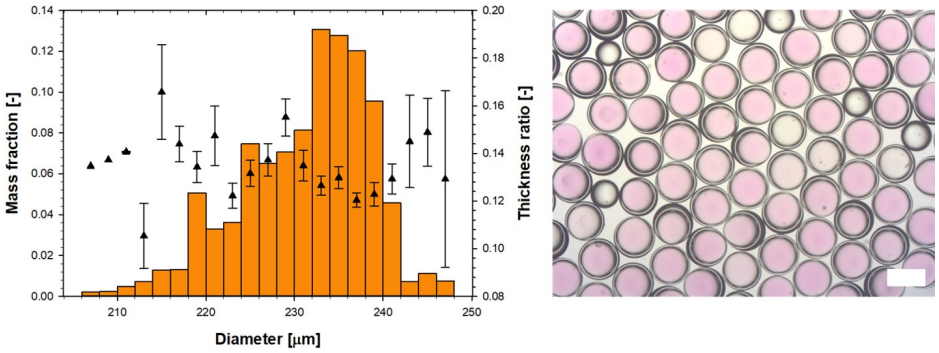

Figure 5.4: TT microcapsule size and thickness ratio distribution (left) with an optical micrograph of the microcapsules in water (right) for the sample TT2. Microcapsules were formed at flows of 500, 300 and 6000 $\mu L\ hr^{-1}$ of the inner, middle and outer fluids, respectively. The scale bar represents a length of 200 μm.

smaller than 320 μm had a more uniform shell thickness, with values closer to unity (Figure 5.5(b)). For the DT, TT1 and TT2 microcapsules, the degree of inhomogeneity was shown to be approximately independent of the microcapsules size (Figures 5.5(a), 5.5(c) and 5.5(d)) and falling in the range $1 - 2$, indicative of a random process most likely emanating from inertial flow effects between the shell and core fluids. This is expected as microcapsule size in the dripping mode is controlled by the outer phase flowrate and shell thickness by the ratio of the middle and inner fluid flowrates (Erb et al. 2011). By controlling the the middle and inner fluid flowrate ratios, Zhang et al. (2019) showed that greater shell inhomogeneity occurred at higher middle to inner fluid flow ratios and were able to tailor the shell inhomogeneity for osmotic triggered release. Table 5.1 summarises the average properties of the microcapsules used in this study.

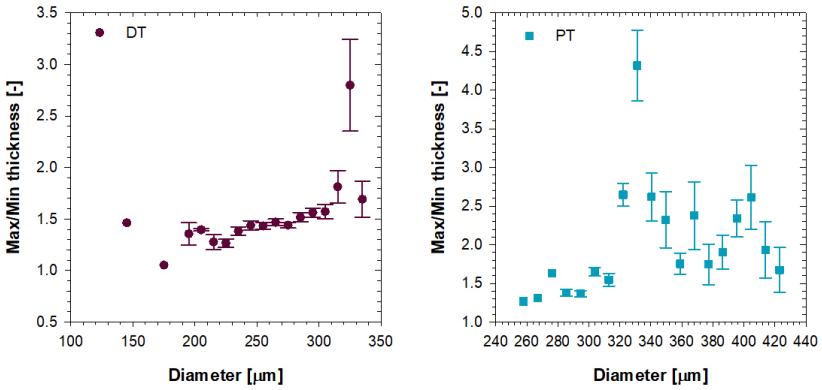

(a) DT microcapsules.

(b) PT microcapsules.

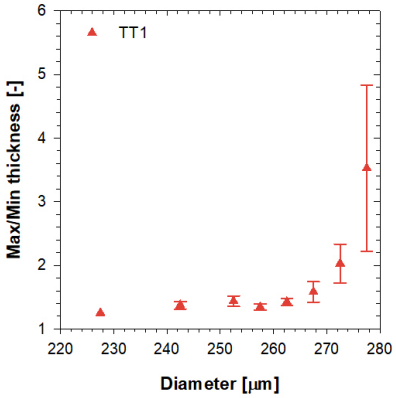

(c) TT1 microcapsules.

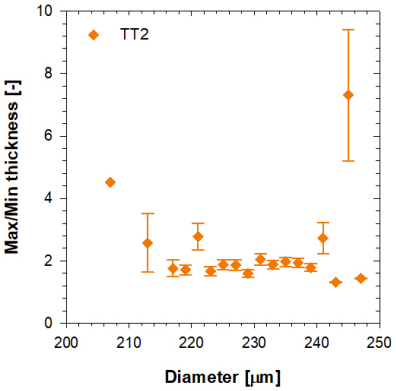

(d) TT2 microcapsules.

Figure 5.5: Variation of the maximum/minimum shell thickness ratio with microcapsule diameter for the DT, PT, TT1 and TT2 microcapsules.

Table 5.1: Average microcapsule dimensions.

Microcapsule	Average diameter $[\mu m]$	Average thickness ratio [%]
DT	277.8 ± 1.0	11.1 ± 0.2
PT	332.3 ± 1.3	13.7 ± 0.3
TT1	260.1 ± 0.5	14.6 ± 0.2
TT2	231.3 ± 0.4	13.2 ± 0.2

5.1.2 Microcapsule loading capacity

The amount of core material relative to the amount of shell material used to encapsulate it is an important property of any encapsulation technique. It is an indicator of material efficiency and waste reduction potential of the encapsulation process. The variation of the loading capacity of the microcapsules as a function of the outer diameter is presented in Figure 5.6 for the four capsule types. The data from the figures reflect those of the relative thickness shown in Figures 5.1 - 5.4 as the relative thickness is related to the ratio of the shell volume to the microcapsule volume. The TT2 microcapsules have a water content that is independent of the diameter as seen before with the relative shell thickness (Figure 5.6(d)). The DT microcapsules have the highest average loading capacity of water to total microcapsule mass at an average of 0.759 $\pm$ 0.004 followed by those of TT2, PT and TT1 microcapsules at 0.602 $\pm$ 0.004, 0.601 $\pm$ 0.005 and 0.568 $\pm$ 0.003 respectively.

5.2 Water vapour transport from microcapsules

5.2.1 Microcapsule deformation due to water loss

The extent of buckling in open air of each microcapsule type was studied qualitatively by observing the drying of a selection of microcapsules under a microscope until buckling as shown in Figure 5.7. The initial images at t = 0 *min* show the microcapsules surrounded by a small amount of water (also revealing the shell thickness by refraction) which gradually evaporates leaving the spherical microcapsules to dry by water transport through the

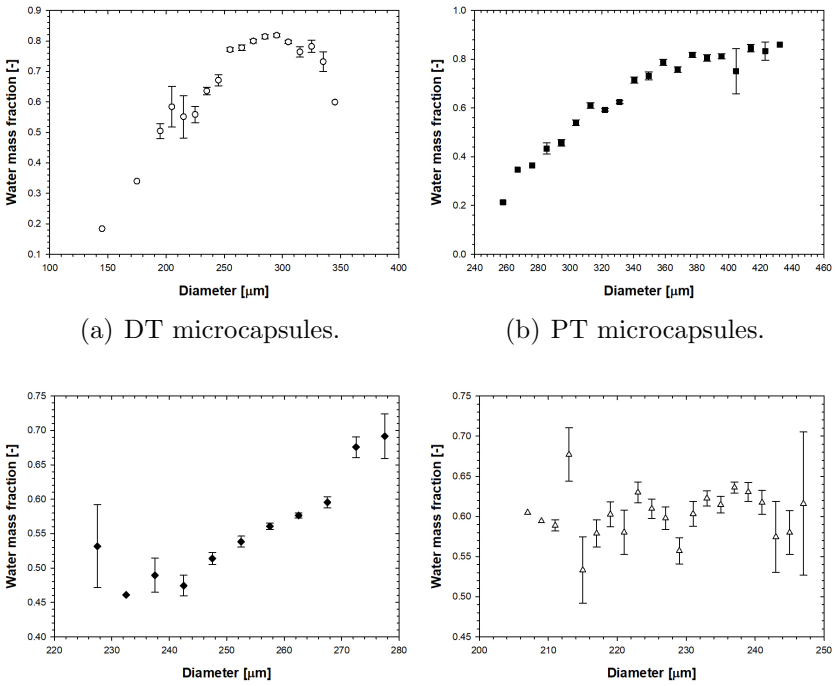

(a) DT microcapsules. (b) PT microcapsules.

(c) TT1 microcapsules. (d) TT2 microcapsules.

Figure 5.6: Water mass fraction of DT, PT, TT1 and TT2 microcapsules versus diameter.

membrane shell. The buckling behaviour of a solvent-filled microcapsule depends on the rate of solvent evaporation, where a higher rate of solvent loss can give rise to the appearance of metastable buckling states (Lei et al. 2019). The microcapsules in this study buckle with a single, axisymmetric indentation, indicative of the slow diffusive transport process of water from the core through the shell at ambient conditions. DT microcapsules buckle earlier than the PT and TT microcapsules respectively as dictated by the combined effect of shell thickness, permeability and stiffness. The first buckling incident was detected approximately 12 *min* after surface water loss. As microcapsules vary in size and shell thickness distribution, the buckling times will vary between microcapsules as clearly shown in Figure 5.7(a) for DT microcapsules. Furthermore, DT microcapsules were observed to collapse completely, with the walls of the capsule eventually coming into contact as shown in Figure 5.7(a). This was also observed for the PT microcapsules (Figure 5.7(b)) after a much longer duration. It is believed that a similar process would occur in a bed of these microcapsules, for example, in a crucible during STA measurements. The TT microcapsules shown in Figure 5.7(c) form a small dimple that showed little growth over the experimental observation time. These microcapsules have a greater average thickness and large thickness inhomogeneity thus making the buckling more localised around the thinnest section of the microcapsule shell. Although the ambient humidity and temperature were not controlled during the measurements, the results qualitatively show the differences in deformation rate/behaviour arising from the combined effect of permeability and shell material mechanical properties.

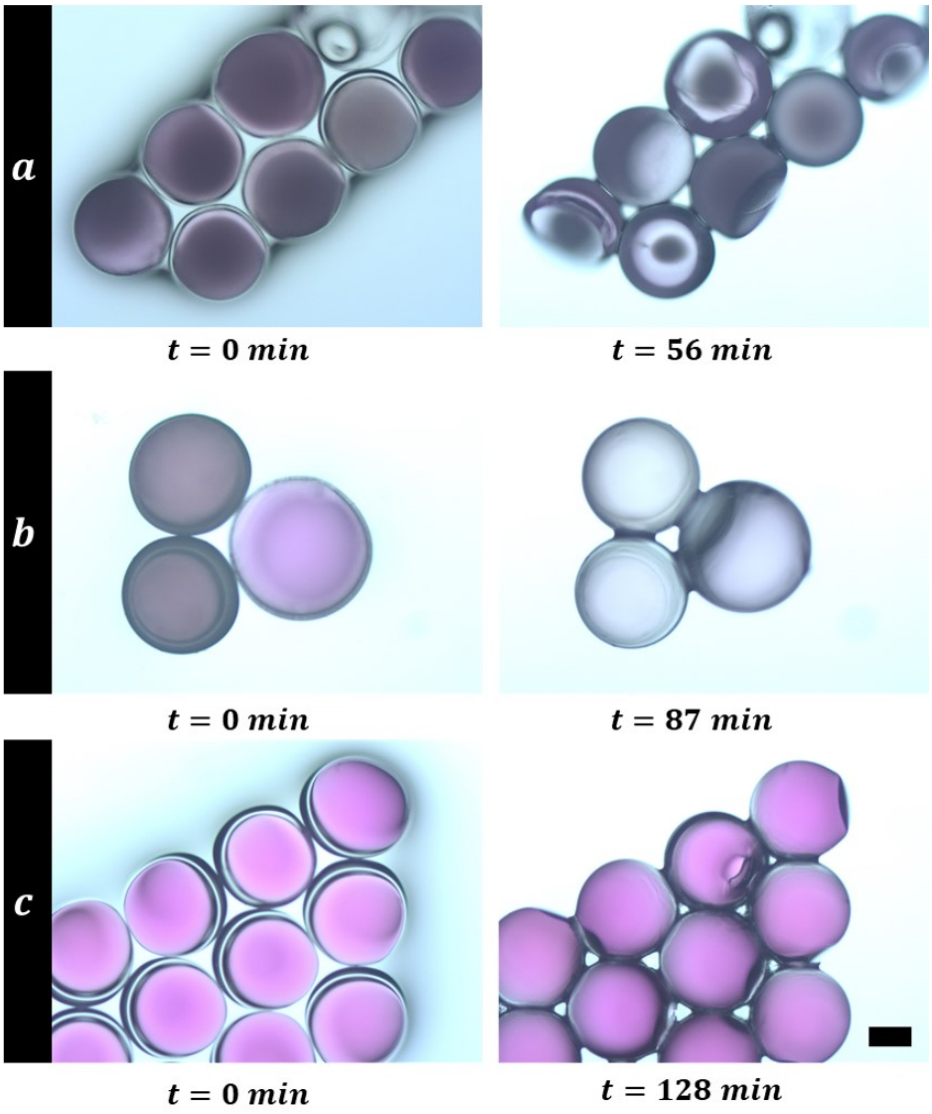

Figure 5.7: Optical microscope images of microcapsules buckling on exposure to ambient conditions on a glass slide. Scalebar is 100 μm.

Depending on the application, the buckling of absorptive microcapsules can be an advantage or disadvantage. For the case of packed beds for CO_2 capture, water loss may be induced by external pressures in the bed and affect the hydration level of capsules (Finn et al. 2019). Using stiffer yet permeable microcapsules presents an opportunity for circumventing such problems. Qualitatively, this shows the ease with which thiol-ene chemistry and microfluidics can be used to alter the stiffness (represented by the product of the Young's modulus E and shell thickness h) value of microcapsules to delay buckling, providing opportunities for tuning such properties for intended operating conditions.

5.2.2 Water vapour transport dynamics from bulk microcapsules

The loss of water from the microcapsules was investigated using STA at an overall nitrogen gas flowrate of 550 *sccm* under isothermal conditions ($30°C$) and atmospheric pressure. Two regimes, signified by a change of slope in the relative mass versus time plots in Figure 5.8 were identified. An initial constant drying rate period akin to other drying systems (Neikov 2019) is readily identifiable from the drying curves of PT (Figure 5.8(b)) and TT (Figure 5.8(c)) microcapsules. This linear regime is associated with the evaporation of free moisture from the surface of the microcapsules as the microcapsules are loaded partially wet into the thermobalance prior to measurement. This linear regime is then followed by a much longer decreasing drying rate period until the equilibrium water mass content of the microcapsule is reached. In

Table 5.2: Comparison of residual mass values as determined from STA and optical measurements for DT, PT and TT2 microcapsules.

Microcapsule	Residual mass (STA) [%]	Residual mass (Optical) [%]
DT	25 ± 1	24 ± 1
PT	35 ± 1	40 ± 1
TT2	44 ± 4	40 ± 1

this regime, it is assumed that there is no free moisture on the microcapsule surface and water loss is driven by diffusion through the microcapsule shell. For DT microcapsules (Figure 5.8(a)), the two regions show similar gradients and are not clearly distinguishable. The time for complete loss of encapsulated water was observed to increase with the density of the shell material with DT microcapsules taking the shortest time of approximately 300 *min* whilst those of the TT type required a longer time period of around 1000 *min* for total water loss. The residual mass of the studied samples, without accounting for the free water, was consistent with the shell mass fraction distribution data determined from optical micrographs and shown in Table 5.2. These results are also consistent with the observations in Section 5.2.1 where the order of total drying time was highest for TT and lowest for DT microcapsules.

As the microcapsules are packed into the platinum crucible, they form a bed and thus a moisture gradient between the open end of the crucible and the bottom. It is thus likely that evaporation of free water from the microcapsule surface and diffusion of water from the microcapsule core occur simultaneously during the constant drying rate period. As the capsules lose water by diffusion, the pressure difference between the internal and external

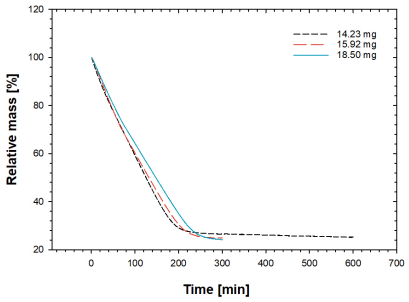

(a) DT microcapsules.

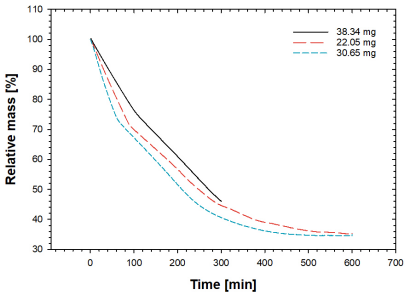

(b) PT microcapsules.

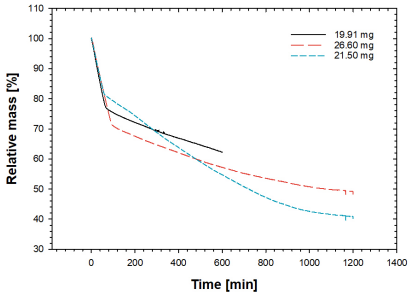

(c) TT2 microcapsules.

Figure 5.8: Relative mass loss of water from DT (a), PT(b) and TT2(c) microcapsules over time.

environment of the shell will reach the critical buckling pressure of the capsule. Theory (Equation 2.8) predicts buckling at an overall volume change of water of 8%, 15% and 14% for DT, PT and TT microcapsules based on average thickness ratio values, respectively. These volume fraction values can be taken as equivalent to the expected mass change for buckling as the density of water is approximately 1 $g\ cm^{-3}$. Thus, comparing these theoretical predictions to the turning points in the STA data reveals that capsule buckling occurs earlier than the observed point of change in the rate of water loss which occurred at an average mass loss of $26wt\%$ and $23wt\%$ for the distinguishable cases of the PT and TT microcapsules, respectively. This implies that buckling most likely occurs during the constant drying rate period with no discernible effect on the drying behaviour of the microcapsules. Continued buckling and thus, preservation of a constant internal pressure as predicted by Equation 2.9 depends on whether the shell deforms plastically or elastically in the buckled region where processes like strain hardening could see a resistance to further buckling.

Determination of the initial rate of mass transfer in the decreasing drying rate period allows for an estimation of the permeability of the microcapsule shell according to Equation 2.10 assuming an average particle size and average, uniform thickness value. It is also assumed that the microcapsules are not compressed and that the external conditions to the microcapsules are dry. Permeability values for the DT, PT and TT microcapsules were determined to be $6.39 \times 10^{-12}\ g\ (Pa\ s\ m)^{-1}$, $10.20 \times 10^{-12}\ g\ (Pa\ s\ m)^{-1}$, and $1.28 \times 10^{-12}\ g\ (Pa\ s\ m)^{-1}$, respectively. The estimated values indicate similar values of permeability for the types of shell material, within an order of

Table 5.3: Glass transition and on-set temperatures of the thiol-ene polymers DT, PT and TT and corresponding sample measurement mass.

Polymer	T_g $[^\circ C]$	Onset temperature $[^\circ C]$	Sample mass $[mg]$
DT	-18.9	-22.8	11.29
PT	3.1	-2.3	7.33
TT	40.5	28.7	21.08

magnitude of each other. Prediction of the water loss profile below the linear regime based on drying models is affected by the size distribution, available surface area in the packed particles as well as mass transfer phenomena from the microcapsules to the pores and the surrounding flow conditions at the crucible outlet. Thus, permeability alone cannot explain the differences in the observed mass loss profiles.

5.3 Thermal properties of the shell material

The chemical structure of the thiol and alkene functional groups dictate the thermo-mechanical properties of the formed polymer. Structures such as the hexagonal rings in the alkene monomer in this work (Figure 5.9) act to raise the glass transition temperature through close packing (Li et al. 2009*a*). Furthermore, the number of reactive groups in the monomers influences the crosslink density and consequently the thermo-mechanical properties. Depending on the working/application temperature of a microcapsule in relation to the glass transition of the polymeric shell, the shell could be either in a "glassy" or "rubbery" physical state with several orders magnitude difference in the elastic moduli.

The DSC scans of the three shell materials in this study are shown in

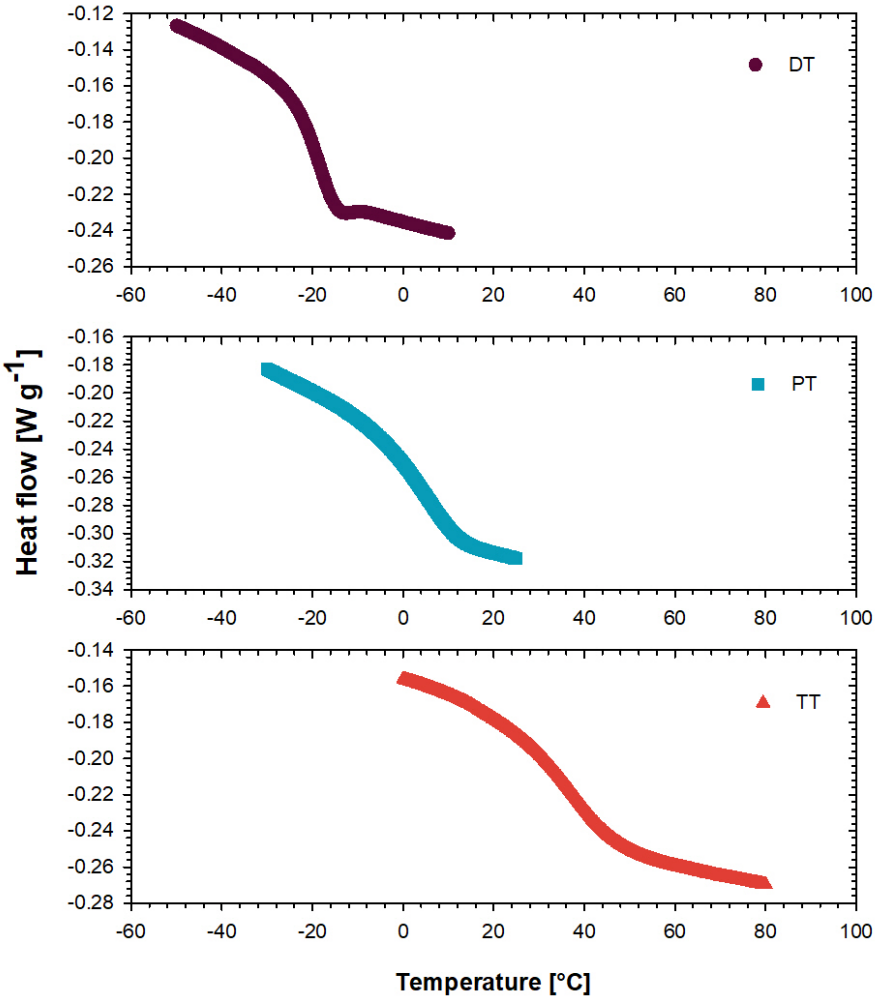

Figure 5.9: DSC curves of the second scan of the thiol-ene polymers DT, PT and TT at a heating rate of $10°C\ min^{-1}$.

Figure 5.9 and the corresponding glass transition temperatures in Table 5.3. The DT polymer had the lowest glass transition temperature at $-18.9°C$, followed by the PT and TT polymers at $3.1°C$ and $40.5°C$, respectively. This can partly be explained on the basis of cross-link density, in that the cross-link density is expected to increase with the number of thiol groups in the monomers (2 for D,3 for P and 4 for T) for the same alkene monomer and thus the glass transition temperature expectedly mirrors this trend. The onset temperatures for the transitions are $-22.8°C$, $-2.3°C$ and $28.7°C$ for the DT, PT and TT polymers, respectively. As well as indicating that the onset of changes in mechanical behaviour are to be expected at lower temperatures than the glass transition temperature, these values show that the width of the glass transition is affected by the chemical structure. The width of the glass transition is affected by the uniformity of the polymer network and Li et al. (2009*a*) indicated that for the TT polymer, conversion tends to be low for polymerisation below the glass transition temperature. The T_g value for TT is consistent with DSC results from other investigators (Li et al. 2009*a*)) to within $5 - 7°C$. However, the values obtained for DT and PT polymers were approximately $25°C$ by DMA (Podgórski et al. 2016) and approximately $30°C$ (Kwisnek 2011) by DSC, respectively. The degree of conversion was not measured for the DSC scans in this work as resins were exposed to conditions (light intensity and temperature) close to those experienced by the microcapsules, however, they confirm the "rubbery" state for DT and PT for conversions $< 100\%$.

Overall, the DSC results reveal that the DT and PT microcapsule shells were in the "rubbery" state and the TT microcapsule shells were in the

"glassy" state at the measurement conditions in Chapter 4.

5.4 Compressive deformation and modelling of microcapsules

5.4.1 Compressive deformation of polymer particles

As alluded to in Section 4.3.2, the single emulsion droplets formed in the decussate regime can be polymerised to form polymer particles of the shell material. The micromanipulation results for the deformation behaviour of these particles are presented in Figure 5.10 for the DT, PT and TT shell materials.

Figure 5.10 shows that the TT shell material is significantly stiffer than both the DT and PT shell materials. This supports the observations of buckling due to water loss presented in Figure 5.7 where the TT shell microcapsules showed only slight buckling after 128 min compared with DT microcapsules which showed early buckling at 12 min into drying. Assuming the Hertz theory can be applied, the Young's modulus of the shell materials can be determined from a linear regression fitting of the compression data as shown in Figure 5.11. A good fitting was obtained for all compressed particles showing good agreement with the Hertz model and thus indicated the assumption of a Poisson's ratio of 0.5, that the material is incompressible (or not swollen) holds. The Young's moduli of the DT, PT and TT shell materials were determined to be $14.8 \pm 0.4\ MPa$, $9.3 \pm 0.3\ MPa$ and $555.3 \pm 0.9\ MPa$, respectively. At the measurement temperature of $30°C$,

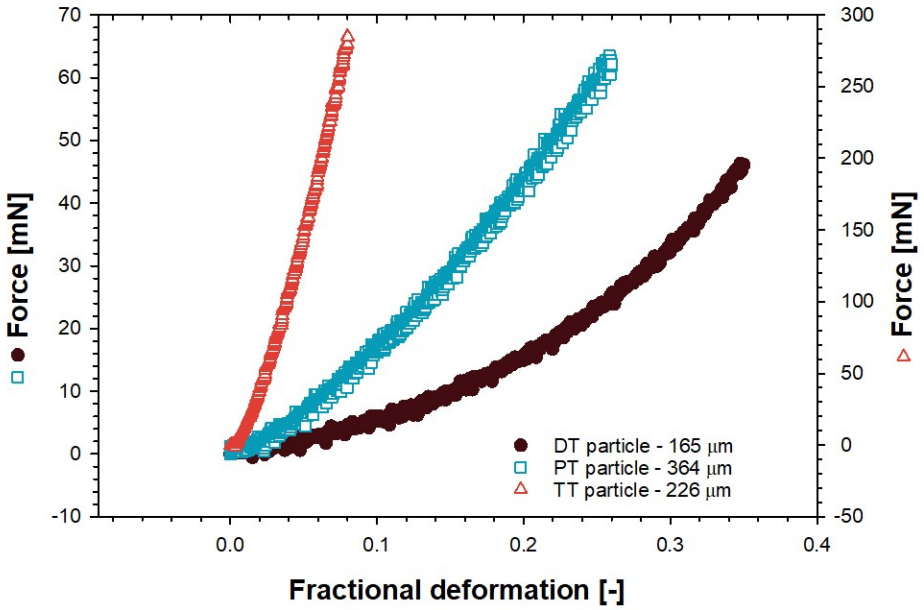

Figure 5.10: Force versus fractional deformation data for microparticales of the DT, PT and TT shell material. Values of the force values for the TT microparticles are shown on the right vertical axis for clarity.

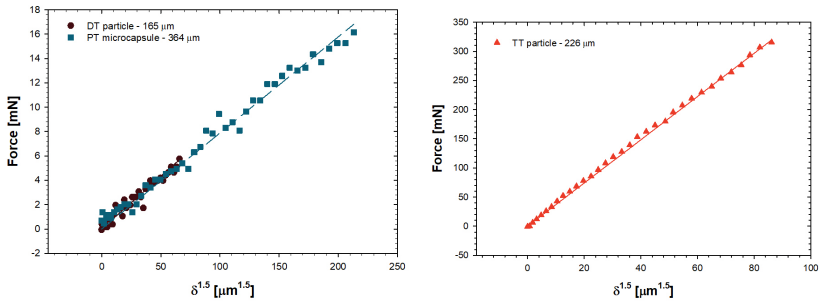

(a) DT and PT microparticles. (b) TT microparticle.

Figure 5.11: Hertz model fittings of the DT, PT (a) and TT microparticle (b) compression data. δ is the raltive displacement between the compressing platens.

these values are estimated to be 10 MPa, 63 MPa and 1568.1 MPa from literature data (Podgórski et al. (2016); Nair et al. (2010); Li et al. (2009a)). Possible differences in the measured values to those in the literature may arise from the fact that the polymer particles are produced in carrier liquid and may be plasticized by possible absorbed water which stresses the importance of droplet formation in the decussate regime as the conditions of the microcapsules are replicated.

5.4.2 Compressive deformation and rupture strength

Representative experimental results of the deformation response to a compressive force until rupture of the studied microcapsules are shown in Figure 5.13 and Figure 5.14. The force was normalised to the cross-sectional area of the undeformed microcapsule. The microcapsules were compressed at a speed of 8 $\mu m\ s^{-1}$ with the minimum number of capsules tested set at 20 in order to ensure statistical significance. Water loss from the microcapsule

reduces the volume of the core in the microcapsule which can lead to errors in the compression data. Additionally, as the internal pressure of the capsule rises due to compression, the rate of loss of the core will increase as captured in Equation 2.10. Experimental data from STA measurements reveal that the rate of mass loss at $30°C$ was in the order of $\sim 10^{-5}\ mg\ s^{-1}$ which is approximately a volume loss rate of $0.2\%\ s^{-1}$ for a particle 200 μm in diameter, for example. Given the time to compress a single microcapsule is $\leq 1\ min$, the permeability at larger deformations, and thus greater internal pressures, may be significant. To investigate the influence of the permeability on the deformation response of the microcapsules, they were initially compressed at three different speeds; 2, 8 and 20 $\mu m\ s^{-1}$ as shown in Figure 5.12. It can be seen that in all cases, as the compression speed is increased, a greater force for a given fractional displacement is realised. As the speed of compression is raised, the timescale for compression becomes shorter than that for the rate of volume loss and thus at a high enough compression speed, the effect of permeability is diminished. This is evident in Figures 5.12(b) and 5.12(c), for PT and TT microcapsules, respectively, where the force-deformation curves coincide at lower deformations. Using this principle, Stenson et al. (2009) were able to show that the "leakiness" of yeast cells could be neglected at high compression speeds, allowing for the modelling of their deformation and determination of the intrinsic mechanical properties of the cell membrane. Results for DT microcapsules in Figure 5.12(a) show a greater change in the force-deformation profiles with speed indicating a higher degree of leaking compared with the PT and TT microcapsules. The results also show that for higher fractional deformations, the speed dependence of the compression

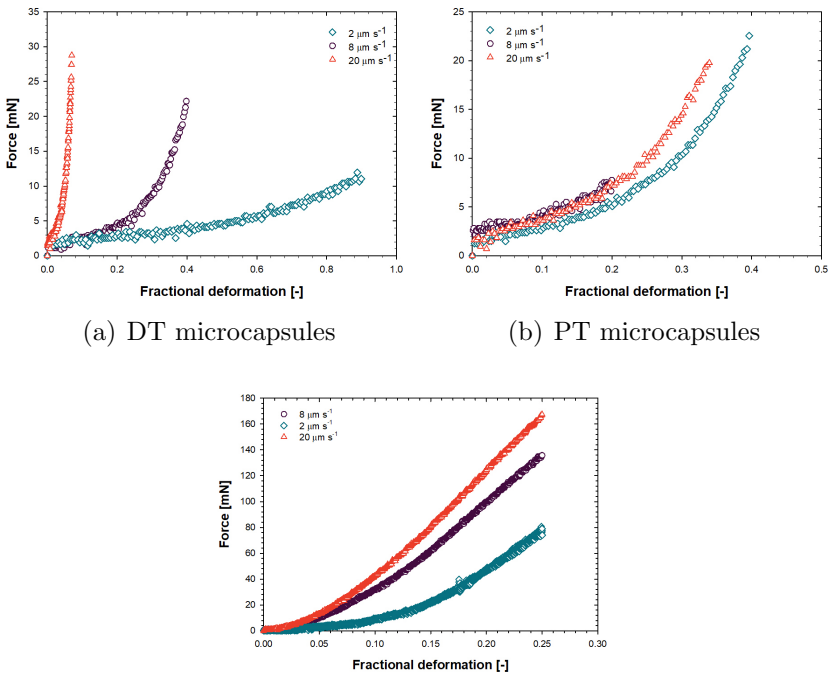

(a) DT microcapsules

(b) PT microcapsules

(c) TT microcapsules

Figure 5.12: Force versus fractional deformation profiles of DT (a), PT (b) and TT (c) microcapsules at sompression speeds of 2, 8 and 20 μm $s6{-}1$.

response is not negligible and must thus be considered in the application in and modelling of real systems. As the speed dependence cannot be easily eliminated from the compression study, a speed of 8 μm s^{-1} was selected for studying the deformation behaviour of DT, PT and TT for comparison.

DT and PT microcapsules have similar deformation behaviour, accommodating large strains at relatively low stresses before the stress rises sharply until rupture. As shown previously, this is partially linked to the volume loss in the microcapsules but also the mechanical properties of the shell material. Nominal rupture stress values for the DT and PT microcapsules permit the direct comparison of the microcapsules given that the deformations at rup-

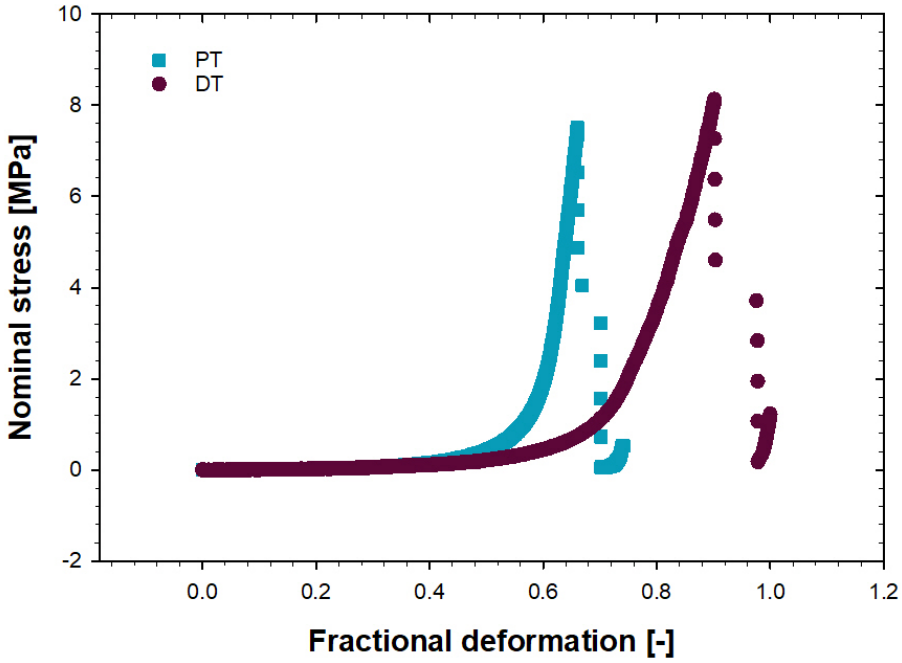

Figure 5.13: Stress-deformation profiles of single microcapsules of DT and PT measuring 287 μm and 361 μm in diameter, respectively.

ture are comparable (Liu 2010). PT microcapsules had an average nominal rupture stress of $3.75 \pm 0.47 MPa$ at an average deformation of $54 \pm 2\%$ with an average particle size of 364.8 ± 6.6 μm. DT microcapsules had an average nominal rupture stress of $8.76 \pm 0.79 MPa$ at an average deformation of 63 $\pm$ 4% with an average particle size of 280.1 ± 4.4 μm. After rupture and on removing the load from the DT microcapsules, the empty capsule shell retained its original spherical shape demonstrating the elastic nature of the shell. The PT microcapsules remained deformed once the load was removed, indicative of viscoelastic behaviour.

In contrast, the TT microcapsules with an average diameter of 257.6 μm $\pm$ 0.7 μm show plastic deformation behaviour with similarly high de-

formation at rupture. Beyond a certain fractional deformation, represented by point P on Figure 5.14, the applied force plateaus, similar to the plastic deformation observed with more widely studied shell materials of melamine-formaldehyde and urea formaldehyde (Mercadé-Prieto, Ruben et al. 2011). Two types of failure behaviour were observed, represented by the experimental data in Figure 5.14. Of the 49 microcapsules compressed, 30% showed deformation behaviour represented by the compression profile M1 in Figure 5.14 with the rest represented by compression profile M2. Microcapsules represented by M1 show an initial linear region at fractional deformations less than 0.1 and corresponding forces less than 2 MPa. The trend then mirrors that of M2, characteristic of plastic yield as observed in the work of Mercadé-Prieto et al. (2012). Thus a "pseudo" yield stress and the corresponding relative deformation can be identified.

The average deformation at rupture and nominal rupture stress of these microcapsules was determined to be 62.5 $\pm$ 0.6% and 8.12 $\pm$ 0.27 MPa, respectively. Additionally, the average nominal yield stress of the capsules was determined to be 2.40 $\pm$ 0.09 MPa at a corresponding fractional deformation of 0.20 $\pm$ 0.01 by determining the point of maximum gradient in the fractional deformation range of 0.1 – 0.4 as previously utilised in the work of Mercadé-Prieto et al. (2012) and Zhang Z. (2001). According to FEM simulation results from Mercadé-Prieto et al. (2012), this point represents a departure from elastic behaviour as a result of yielding in the shell near but not in contact with the platen. Although the rupture stress of the TT microcapsule is comparable to that of the other microcapsules in this study, the pseudo yield point data suggests that they lose their structural integrity

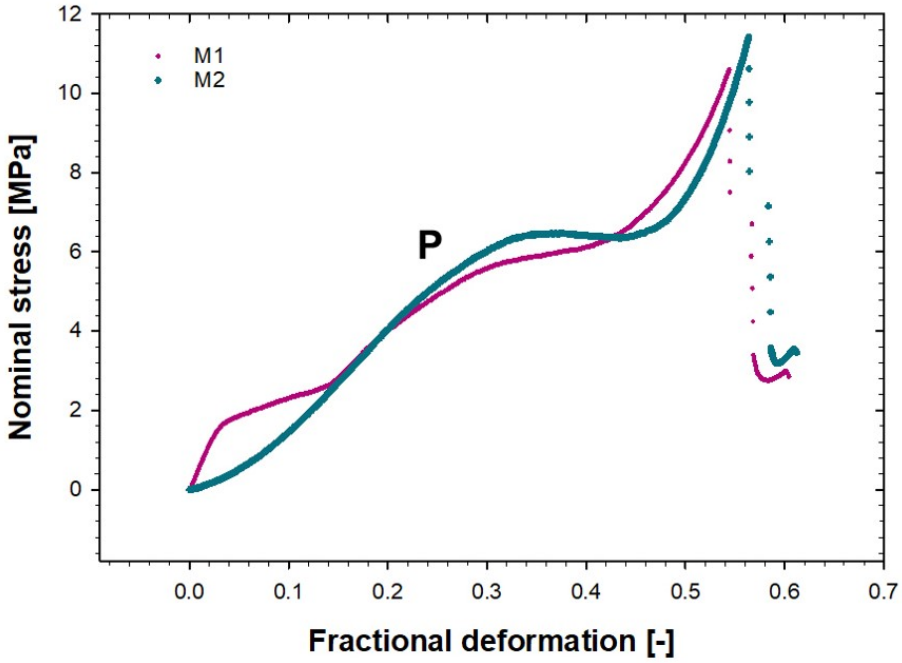

Figure 5.14: Stress-deformation profiles of TT1 microcapsules M1 and M2 measuring 273 μm and 260 μm in diameter, respectively.

at much lower stresses. Thus, the lower water vapour loss properties of the microcapsule have to be weighed against these revelations about the mechanical properties. The TT microcapsules fail by yielding without the loss of core material as later verified by an audible popping of the microcapsules on rupture. These micromanipulation and DSC results demonstrate that a better understanding of the temperature and strain dependent Young's modulus is required for application of these microcapsules in environments where temperature variation and buckling is expected such as in carbon capture. Understanding of these dependencies also presents an opportunity to tailor the buckling response of such microcapsules as a way to influence their sorption behaviour. As the temperature of the microcapsule changes during a sorption cycle, it is possible for the shell material to transition from a glassy to a more rubbery state, increasing the tendency to collapse as demonstrated by the three materials studied in this section.

Figure 5.15 shows the relationship between the microcapsule nominal rupture stress against microcapsule diameter. In general, the rupture force is inversely proportional to the diameter as demonstrated in the works of Mercadé-Prieto et al. (2011). The size ranges of DT and TT microcapsules coincide and allow for comparison in Figure 5.15(a). The DT microcapsules have thinner walls and rupture at higher apparent stresses than the thicker-walled TT microcapsules. At room temperature, the DT material is in the rubber state and fails at much larger strains compared to that of TT which is in the brittle-ductile state at room temperature (Smith et al. 2009). However, further consideration of the "leakiness" is required in order to determine the true rupture stress of the microcapsules. A distinction was made between the

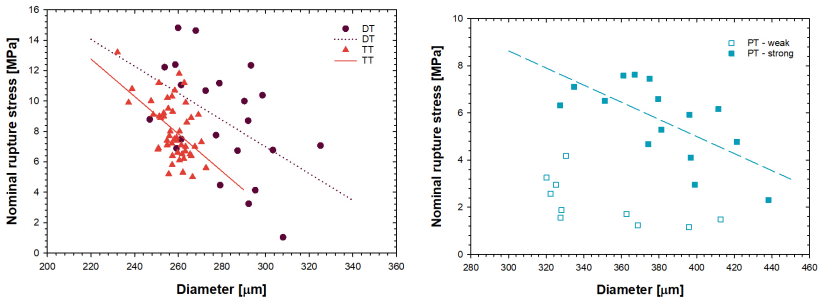

(a) DT and TT1 microcapsules. (b) PT microcapsules.

Figure 5.15: Nominal rupture stress as a function of microcapsule diameter for DT, PT and TT1 microcapsules.

PT microcapsule rupture data to separate the "weak" microcapsules from the "strong" as shown in Figure 5.15(b). These "weak" ruptures are concentrated in the 300 – 350 μm diameter range which displayed the highest values of the maximum/minimum thickness ratios and are thus expected to show the greatest variability in rupture strength. Lines in Figure 5.15 are drawn as a guide to the eye however, Mercadé-Prieto & Zhang (2012) indicates that a linear behaviour between the rupture stress and microcapsule size is expected, provided rupture occurs at a specified failure strain of the material for all microcapsules. The deformation at rupture for the microcapsules in this study are presented against microcapsule diameter in Figure 5.16 and show that this criterion applies in this study as well.

5.4.3 Modelling based on the Hertz and Tatara theories

In the application of the Hertz and Tatara models, the microcapsule is treated as a single entity regardless of the internal structure. The simplicity of the measurements and application of the models are the basis for the continued

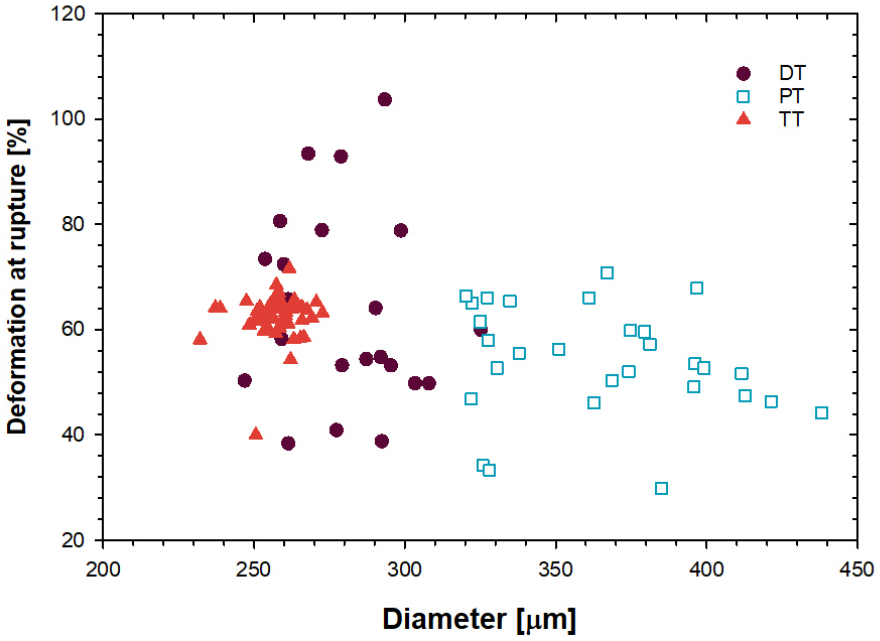

Figure 5.16: Variation of deformation at rupture for DT, PT and TT1 microcapsules with the microcapsule outer diameter.

use of the models in the characterisation of microcapsules. The assumptions in applying the two models are introduced in Chapter 2 (refer to Johnson (1985) and Shima et al. (1993) for further details) and include strain conditions of $< 10\%$ for the Hertz model (Equation 2.5) and $< 60\%$ for the simplified Tatara model (Equation 2.6). It is also assumed that water loss from the microcapsules can be neglected as well as that the Poisson ratio (ν) of the microcapsules is 0.5. Additionally, compression is assumed to occur on a frictionless surface. In light of these assumptions, data were fitted to the models and the Young's moduli (E) determined for the three types of microcapsules.

At low displacement values, the force measurement is comparable to the sensitivity of the transducer ($0.49\ mN$), this uncertainty in the measurement has a further contribution from the accuracy in specifying the point of zero displacement between the probe and the microcapsule. For a consistent specification of the point of zero displacement, only force readings above twice the sensitivity value were used with the displacement corresponding to the initial force value that meets this criterion set as the zero displacement value.

The compression data for archetypal microcapsules of the three types of microcapsules are presented in Figure 5.17 and Figure 5.18 along with the minimum least squares fitting results of the Hertz and simplified Tatara models, respectively. Figure 5.17 is the linearized form the experimental data from the compression of TT microcapsules where the slope indicates the Hertzian Young's modulus. The correlation coefficients for the Hertz fitting are > 0.9. As shown in Figure 5.12(c), the volume loss effect is negligible for small fractional deformations of the TT microcapsules at compression speeds

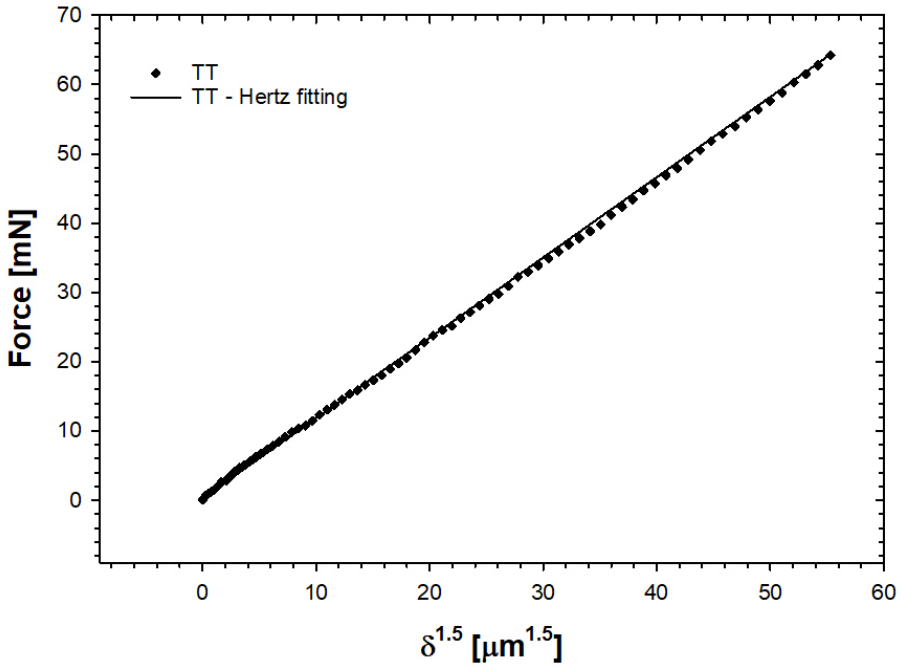

Figure 5.17: Linearized Hertz model fitting to compression data for a single TT1 microcapsule with a diameter of 269 μm.

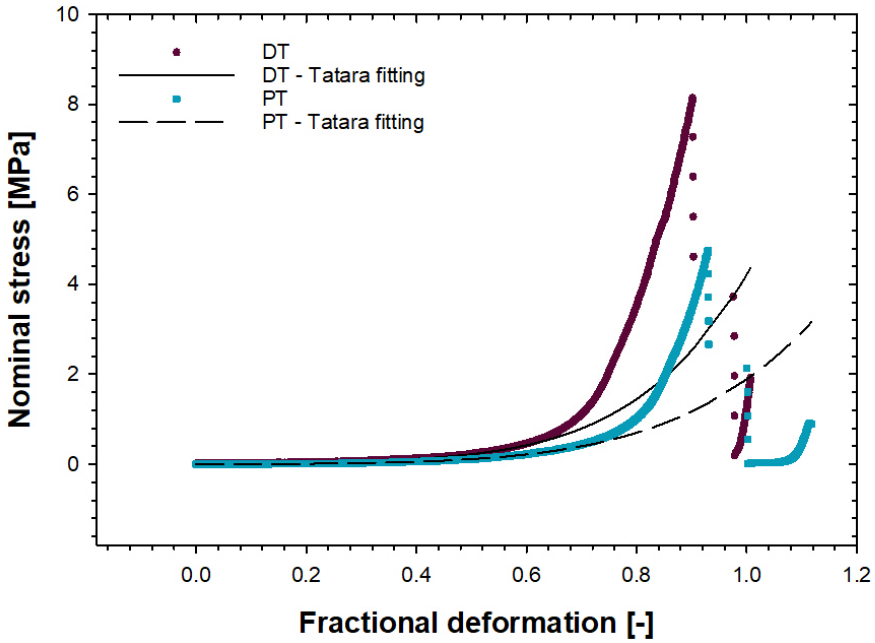

Figure 5.18: DT and PT microcapsules compression data with simplified Tatara model fitting by minimum least squares. Diameters of the DT and PT microcapsules were 287 μm and 361 μm, respectively.

$> 8\mu m\ s^{-1}$ and indicates that the Hertz model can be used to determine a pseudo-Young's modulus for the TT microcapsules. For the DT and PT microcapsules, force values in the deformation range of $< 10\%$ were comparable to the sensitivity of the force transducer and a Hertzian Young's modulus could not be determined accurately. The pseudo-Young's modulus from the Tatara model fitting is computed from the first coefficient of Equation 2.6. The average values for the calculated moduli are shown in Table 5.4 and are compared with the values obtained for the pure bulk material from the literature.

The experimental compression results are shown (Figure 5.18) in com-

parison to the Tatara model using the fitted Young's moduli for the full compression of the microcapsule up to a fractional deformation value of 0.4. Expectedly, the model does not describe the full deformation behaviour of the microcapsules. The simplified Tatara model, assuming linear elasticity, underestimates the force at larger deformations but captures the deformation behaviour well for fractional deformations up to 0.6. The consistency of the experimental results for the core-shell microcapsule compression with those of rubber spheres (Shima et al. (1993) and James et al. (2020)) suggests the applicability of non-linear elastic models. As the model assumes there is no volume loss in the microcapsules, its applicability is limited to situations where the external conditions such as water vapour pressure do not vary. Thus new models that account for the volume change as well as water vapour pressure need to be developed for applications in real systems.

The nominal rupture stress provides a convenient method of comparing microcapsule strength, however, the true rupture stress has utility in cases where a microcapsule is expected to rupture due to rising internal pressure for example, due to osmosis (Nabavi et al. 2016). The true rupture stress can be calculated from the nominal rupture stress if the contact area is known. This requires an assumption about the material properties such that an appropriate model can be applied to determine the contact area in the situation that it cannot be measured directly. In the case of small deformations, of the order of the shell thickness, the Hertz model can be applied to describe the contact area of a linearly elastic sphere (Liu 2006). However, at large deformations, the contact area increases laterally, this is unaccounted for in the Hertz model. In contrast, the Tatara model (Tatara 1993) accounts for

Table 5.4: Young's moduli determined from least squares fittings of the Hertz and Tatara models compared with literature values.

Microcapsule	E $[MPa]$	E (bulk) $[MPa]$
DT	31.1 ± 3.4 (Tatara)	10 (Podgórski et al. 2016)
PT	9.0 ± 3.2 (Tatara)	63 (Nair et al. 2010)
TT	135.9 ± 1.8 (Hertz)	1568.1 (Li et al. 2009*a*)

this lateral change assuming the spherical material obeys the Mooney-Rivlin equation. This involves solving a series of equations given the linear elastic modulus, Poisson's ratio and load on the elastic sphere. Thus, using the data for the force at rupture with the elastic moduli from the Tatara fitting for the DT and PT microcapsules in this study, the rupture stresses were recalculated to be 3.6 MPa and 1.8 MPa, respectively. Additionally, the corresponding contact radii were determined to be 216 μm and 238 μm for DT and PT microcapsules, respectively. The Poisson's ratio was assumed to be 0.5. These values are significantly smaller than the nominal rupture stresses presented in the previous subsection and highlight the importance of the model and material property considerations in characterizing the critical mechanical parameters for applications where significant volume changes in the core are anticipated.

Using the bulk moduli values from literature for the three types of shell material, the critical buckling pressure and the internal pressure after buckling can be calculated using Equations 2.8 and 2.9 from the work of Coupier et al. (2019). Values of the internal pressure after buckling are in the order of MPa whereas as the driving force for water loss, the water vapour pressure difference, is in the order of kPa. The deformed capsule experiences

an elastic stress in the shell and a resulting internal pressure which Quilliet (2012) and Finn & Galvin (2018) have shown is negative and opposes further mass transfer out of the shell in the deflated state. Thus, in this particular case, such a high pressure would resist any further water transport from the microcapsule. Indeed for the modelling work of Finn & Galvin (2018) on microcapsules with a shell Young's modulus of 150 kPa, the internal pressure of the deflated capsule was shown to modulate the driving force for water vapour transport. However, the large buckling and internal pressures calculated here and the observed capsule buckling suggest that the water loss is driven by capillary pressure. This observation has critical implications on the transport mechanism of the core material to the external environment as for microcapsules that do not buckle upon the loss of internal solvent, a cavity can form as observed by Nabavi et al. (2016), in such a situation mass transfer of a vapour through the shell to the external environment will occur which could result in several orders of magnitude difference in the mass transfer rates compared with direct liquid transport through the shell. Capillary forces generated by the evaporation of water from nanopores in the polymer shell (Lei et al. 2019) could be sufficiently large to cause the buckling and mass loss observed in Figure 5.7 - Figure 5.8. This inward capillary pressure can be estimated from Darcy's law (Handscomb et al. 2009).

5.5 Summary

Microcapsules of three different types of thiol-ene shell material with a water core were prepared in glass microfluidics and their thermal, water-loss

and mechanical properties were measured. Three different thiol monomers were reacted with a single alkene monomer to form the three different kinds of shell material (DT, PT and TT). Size distribution data determined from optical measurements indicated variability in both average thickness and loading capacity with the microcapsule diameter. Shell inhomogeneity was also characterised with the ratio of the maximum to minimum thickness (max/min ratio) of the shell. This value was shown to impact the rupture strength of microcapsules with weaker microcapsules also having high max/min ratios. DSC results for the neat shell materials showed glass transition temperatures in the range $-20°C$ to $45°C$. This was explained in terms of the number of functional groups in each thiol monomer type where monomers with a greater number of thiol groups lead to greater cross-linking and thus higher glass transition temperatures. It was also verified that the DT and PT microcapsules were in the "rubbery" state whereas the TT microcapsules were in the "glassy" state under water-loss and micromanipulation measurement conditions.

The use of particles produced in the decussate regime allowed for the determination of the Young's moduli of the three shell materials from fitting the Hertz model to polymer particle compression measurements. The Young's moduli of the DT, PT and TT shell materials were determined to be $14.8 \pm 0.4\ MPa$, $9.3 \pm 0.3\ MPa$ and $555.3 \pm 0.9\ MPa$, respectively. The values followed the same trend as literature values but were lower than the expected values. As the polymer particles are produced in emulsion conditions, results may be affect by the presence of other components such as water in the bulk polymer.

Micromanipulation compressions of the microcapsules revealed elastic deformation behaviour for the DT and PT microcapsules whereas the TT microcapsules displayed "elastic-plastic" deformation behaviour. Nominal rupture stress values were determined to be higher for the DT microcapsules followed by PT and TT microcapsules. Water-loss rates determined by thermogravimerty under isothermal conditions decreased with increasing glass transition temperatures and could be explained on the basis of cross-linking. Buckling of all the microcapsules at ambient conditions was verified for all microcapsule types and theoretical predictions of the buckling pressure indicate that buckling is most likely as a consequence of capillary forces in the shell membrane arising from the evaporation of the water core. The force-displacement data for the DT and PT microcapsules were fitted to the Tatara model up to fractional deformations of 0.6 and the good fitting to the Hertz model was obtained with the TT microcapsules up to a fractional deformation of 0.1. These models were used to calculate pseudo-Young's moduli of the microcapsules for comparison. However, a true core-shell model that accounts for shell thickness and thermally-dependent mechanical properties needs to be developed for encapsulation processes involving volume changes of the core with large temperature changes.

CHAPTER 6

Results and Discussions III: Dynamic study of microencapsulated water vapour sorbents

Key challenges of conventional composite sorbents based on porous matrices are the overhydration of the porous matrix, due to excessive water uptake, which leads to salt loss via deliquescence and leaking as well as salt agglomeration within the porous network upon drying. Promising sorbent materials will be capable of addressing these issues whilst also maintaining the important properties such as high energy storage density. New composite sorbents of $LiBr$ and $CaCl_2$ inside core-shell microcapsules are presented in this chapter. Their performance in addressing these issues over hydration-dehydration cycles is explored. The sorption dynamics are investigated using the simultaneous thermal analysis (STA) technique and interpreted on the basis of the linear driving force model. In producing the encapsulated sorbents, a broader range of shell materials were used in order to extend the range of shell ma-

terial hydrophobocity and cross-linking. The internal and external changes in the encapsulated sorbents are also investigated using a combination of scanning electron microscopy and x-ray computed microtomography.

6.1 Morphology and size distribution

The size of microcapsules determines the available surface area for mass transfer of the sorbate and the shell thickness governs the structural integrity of the microcapsules as well as the mass transfer resistance between the core and the external environment. The optical measurement of these parameters is presented in this subsection including the shell inhomogeneity which was demonstrated to have an impact on the microcapsule strength in Chapter 5. The loading capacity in terms of the dry contents of the microcapsule is also introduced as a useful basis for comparison of different samples.

6.1.1 Size and shell thickness distribution

As in Chapter 5, the composite materials are identified according to their shell material; DT, PT, TP, TT and F, with the numbers indicating differences such a core contents or shell thickness as summarised in Table 6.1. Size distribution area plots of the microcapsules studied in this section are presented in Figure 6.1. DT2 microcapsules have the largest dry mass weighted mean diameter of 421.4 $\pm$ 1.1 μm and the TT1 microcapsules have the lowest dry mass weighted mean diameter of 235.9 $\pm$ 0.5 μm. The coefficient of variation (CV) is in the range 1.5 – 11%; the higher values in this range are due to unsteady flows in the microfluidic device which gives rise to more

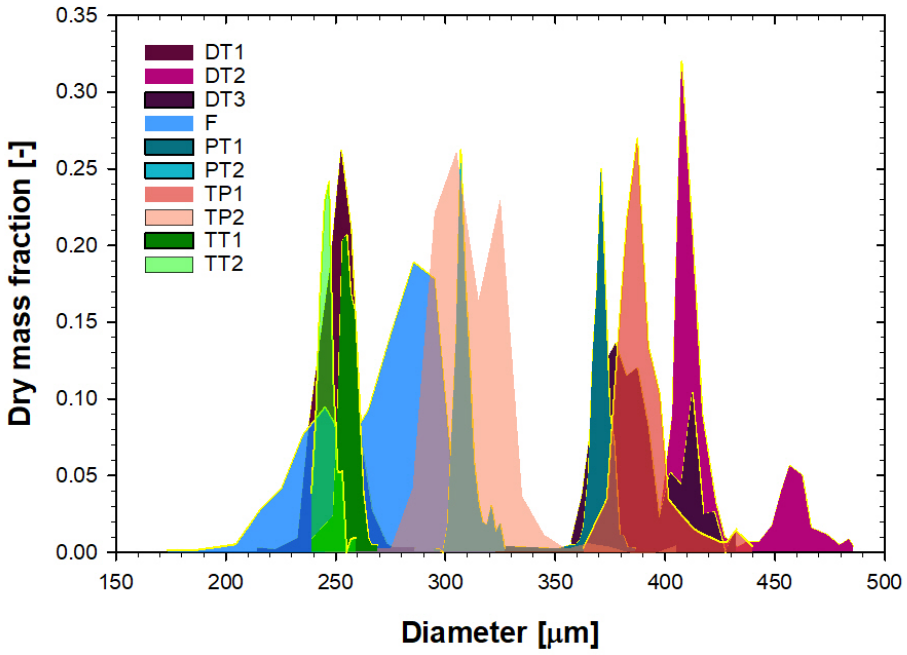

Figure 6.1: Size distribution of microcapsules on a dry mass basis.

polydisperse distributions. In fact, some microcapsules show bimodality in their distributions as shown in Figure 6.1 for the distributions of DT2, DT3 and F microcapsules. Bimodality of the size distribution in microfluidics is an artefact of pulsed flow at the flow conditions used in forming the double emulsion templates. These three microcapsule types accordingly show high values of the CV at 4.7%, 4.1% and 10.6%, as well as matching span values of 13.0%, 11.1% and 23.4%, respectively. The average thickness ratio values for the studied microcapsules are presented in Table 6.1 and fall in the range 0.05 – 0.15 with TP1 microcapsules possessing the smallest relative thickness of the shell at a value of 0.03 and PT1 microcapsules, the largest with a thickness ratio of 0.18.

6.1.2 Microcapsule loading capacity

The mean salt mass fraction of the dry microcapsules is presented in Figure 6.2 classed according to the microcapsule type. Values are calculated based on size data from the optical images of the microcapsules and assuming the salt concentration of the core is equivalent to the bulk concentration of the inner fluid in the microfluidic device ($LiBr$: 1 $g\ cm^{-3}$ and $CaCl_2$: 0.75 $g\ cm^{-3}$) and also that the shell material does not swell. Microcapsules with the thinnest and least dense shells expectedly have the highest salt dry mass fraction with TP1 microcapsules possessing the highest content exceeding the salt loading of some conventional porous host matrix composites (Jabbari-Hichri et al. 2015). PT1 microcapsules have the lowest salt content of $46wt\%$. Figure 6.1 shows that the fractional salt content versus the microcapsule size mirrors the relative shell thickness which indicates that microcapsules with the highest salt content have the thinnest shells. Variation of the loading capacity and relative thickness is dependent on the ratio of the inner and middle fluid flows and deviation in this value will give rise to a variable thickness of the microcapsules.

6.1.3 Shell inhomogeneity

Values of the average shell inhomogeneity of each microcapsule type are presented in Table 6.1. TT and PT type microcapsules have the larger values of shell inhomogeneity with the thickest part of the shell exceeding three times the thickness of the thinnest. Shell inhomogeneity is governed by the volume of the shell fluid, flowrate, interfacial tension as well as density difference

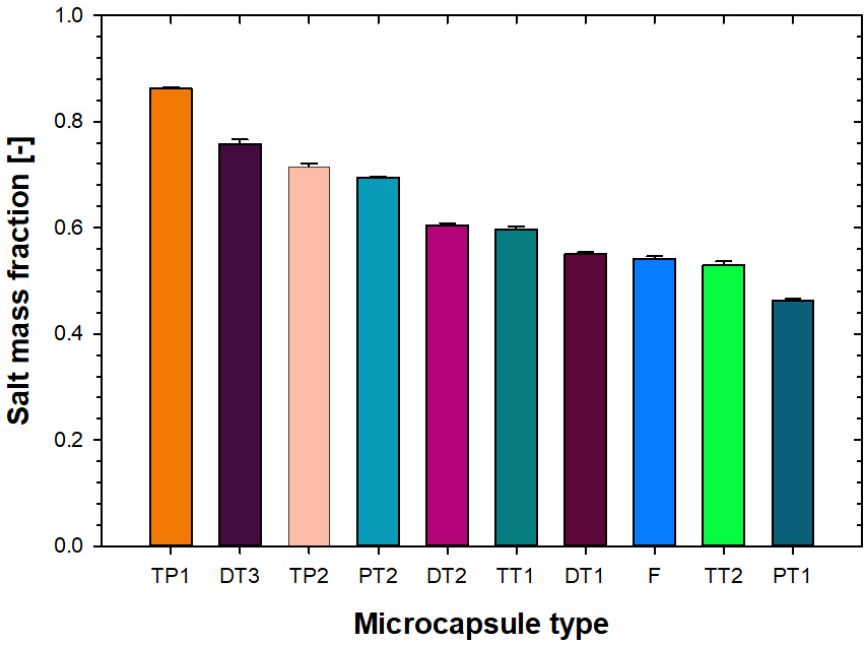

Figure 6.2: Salt mass fraction of microcapsules in descending order of salt content. Microcapsules of the same shell material have bars of the same colour.

Table 6.1: Microcapsule mean size, thickness and max/min thickness ratios.

Microcapsule	Core	$d_{4,3}$ $[\mu m]$	Thickness $[\mu m]$	Max/Min [-]
DT1	$LiBr$	251.1 ± 0.4	18.0 ± 0.2	2.49 ± 0.11
DT2	$LiBr$	421.4 ± 1.1	25.2 ± 0.3	1.87 ± 0.08
DT3	$CaCl_2$	386.5 ± 2.2	10.5 ± 0.5	1.44 ± 0.04
F	$LiBr$	270.4 ± 1.1	19.4 ± 0.3	1.28 ± 0.03
PT1	$LiBr$	370.7 ± 0.3	32.9 ± 0.4	6.51 ± 0.35
PT2	$LiBr$	309.2 ± 0.2	12.3 ± 0.1	2.09 ± 0.22
TP1	$LiBr$	389.5 ± 0.6	6.0 ± 0.1	1.61 ± 0.20
TP2	$LiBr$	309.8 ± 0.7	11.8 ± 0.4	1.97 ± 0.07
TT1	$LiBr$	256.1 ± 0.2	14.7 ± 0.4	3.18 ± 0.08
TT2	$LiBr$	235.9 ± 0.5	16.5 ± 0.4	4.40 ± 0.35

between the core and shell. For the TT and PT microcapsules, their double emulsion templates were generated asymmetrically in the flow-focusing microfluidic device with the middle phase concentrated towards the leading edge of the double emulsion droplet and the inner phase towards the rear end of the droplet as represented by the schematic in Figure 3.6. This asymmetry was "fixed" in place by photopolymerization as discussed in earlier sections.

6.2 Dynamics of water vapour sorption/desorption

6.2.1 The sorption-desoption test cycle

The microcapsules of different shell material and thickness are compared on the basis of sorption/desorption kinetics. Typical experimental data are shown in Figure 6.3 for the second sorption/desorption cycle of a sample of the TP1 microcapsules after initially running the same cycle with the nascent microcapsules. The dry mass content of the sample is determined from this

initial run and used in subsequent calculations for determining properties on a dry-mass basis. The sample was exposed to a relative humidity of 23% at a temperature of $30°C$ for 120 min, this is represented by a water mass flowrate of 0.3 $g\ hr^{-1}$ in Figure 6.3. The desorption stage commences with a step change in the water vapour supply to zero and a ramp to a dehydration temperature of $150°C$, at a rate of $5°C\ min^{-1}$. The temperature profile represented by the dotted line in Figure 6.3 shows an overshoot past the set-point temperature to a maximum temperature of $170°C$ (governed by the set temperature and the PID controller of the device) which is below the thermal degradation temperature of the shell material (Li et al. 2009*b*) and above the equilibrium temperature of the salt hydrates of both the $LiBr$ and $CaCl_2$ salts used in this work (Conde 2004). On a step rise in the water vapour pressure, hydration commences after a short lag-time and continues until a step drop in the water vapour pressure to zero where the mass drops due to the loss of absorbed water as a result of the partial vapour pressure drop; this is then followed by a more rapid rate of loss of mass driven by the temperature change. The desorption cycle commences instantaneously with no observable lag-time at the measurement resolution. During desorption, water is transported from the microcapsule core to the external surface where it evaporates. The concentration of the salt solution in the core gradually increases until the crystallisation point where salt crystals nucleate and gradually grow until all the water has been removed. At high desorption temperatures, the remaining water of crystallisation in the salt hydrates is further removed. This is often observed as a second peak in the heat flow profile, however, at the heating rate used in this work, the peaks due to

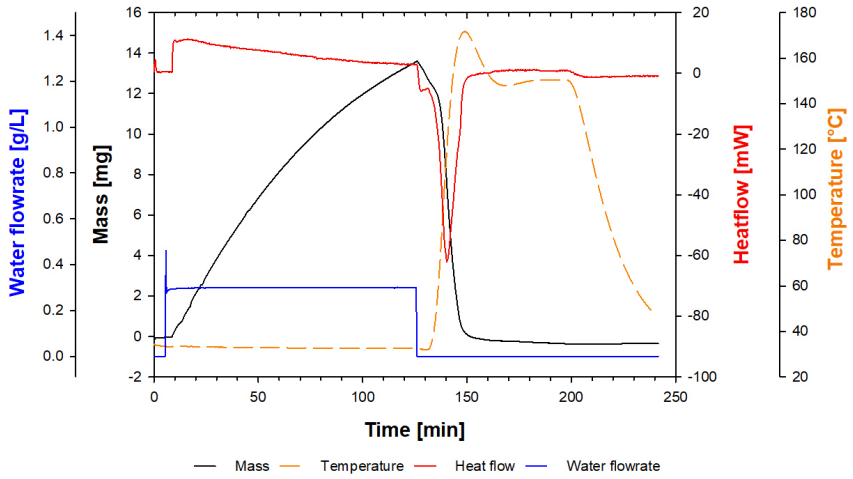

Figure 6.3: Typical sorption-desorption response of microencapsulated salt sample measured using simultaneous thermal analysis (STA).

loss of solution water and hydrate water cannot be distinguished. This is the case also during absorption when heat is released by the sample. A sharp peak in the heatflow profile is observed during desorption compared to ad/absorption, representing the heat absorbed by the evaporating water and is determined by the heating rate. The total mass of water absorbed was calculated as the difference between the initial and maximum mass during the absorption cycle. There is a slight difference between the initial and final "dry" mass of the microcapsules which is most likely due to reabsorption of low level moisture in the system once the furnace has cooled to the starting temperature of the cycle of $30°C$. This has an average error contribution of approximately 1% to the calculated water uptake mass. The consistency with the initial mass also demonstrates the thermal stability of the materials in this study. Thus, the requirement for new composite materials to have thermal stability at a temperature of $150°C$ has been met.

The area under the DSC signal curve, represented by the heat-flow profile in Figure 6.3, for the duration of the sorption cycle, indicates the amount of energy released when water vapour is ad/absorbed and the peak in the desorption region indicates the absorption of this energy as water vapour is released from the sample. Further assessment of these values is presented in Section 4. In a typical absorption cycle, the water is only partially removed and thus the energy released will be lower as it scales with the amount of water absorbed/desorbed by the system (N'Tsoukpoe et al. 2010).

6.2.2 The linear driving force model

The temporal progress of the hydration reaction can be characterised by the conversion x which can be expressed as the ratio of the difference between the instantaneous mass m and initial mass m_0 (mass gain) of the sorbent to the difference between the final/equilibrium mass m_{eq} and the initial mass of the sorbent and thus varies between zero and unity for the dry and fully saturated sorbent cases, respectively. This can be expressed as in Equation 6.1.

$$x = \frac{m - m_0}{m_{eq} - m_0} \tag{6.1}$$

A linear driving force (LDF) model relating the conversion to the sorption time was adopted in analysing the kinetics in this work as has been used in other studies (Dawoud & Aristov 2003) as it satisfactorily characterises the overall uptake at the bulk level, where the particle-level sorption kinetics are lost (Sircar & Hufton 2000). The LDF model is expressed as in Equation

6.2,

$$x = x_0(1 - \exp(\frac{-t}{\tau})) \tag{6.2}$$

where τ is the characteristic time for the process, x_0 is the equilibrium conversion and the other symbols are as previously introduced. Another mathematical model frequently used to describe sorption dynamics is the Fickian diffusion model (Sircar & Hufton 2000), however, often the LDF model is favoured for its mathematical simplicity and low computation requirements in modelling sorption systems. Absorption measurements were run for a fixed time of 120 *min* which does not allow for the equilibration of the sample mass during the hydration process thus an approximate equilibrium mass was determined by fitting data to the LDF model using non-linear model fitting functions in Matlab. Consistency of the model fitting in determining the value of equilibrium mass was checked by sampling down the number of datapoints for the fitting and predicted values and it was found that for profiles spanning at least twice the characteristic time, the model estimates were satisfactory with an error of approximately 1%. However, where the sorption time (120 *min*) does not satisfy this condition, the error in the calculated characteristic time is larger and can be estimated by interpolation from the master curve (Appenndix C). Thus, the characteristic time for each absorption profile of the microcapsules in this study can be determined and compared assuming the LDF model can describe all profiles.

6.2.3 Variation of the sorption dynamics with the shell material

The absorption dynamics of the microcapsules with different shell material are compared in Figure 6.5 which shows the mass of water absorbed per unit dry mass of the sample over time. The PT2 and TP1 microcapsules show the greatest rise in water content per unit dry mass compared with all other samples. These microcapsules have the high salt content estimated to be $69wt\%$ and $86wt\%$, respectively. These microcapsules also have low relative shell thicknesses of 0.08 and 0.03, respectively. The lowest uptake is by the PT1 microcapsules with the lowest estimated salt mass fraction of $36wt\%$ and relative shell thickness of 0.18. Figure 6.5 also shows that the TT microcapsules reach the equilibrium uptake within the fixed absorption period, this was unexpected considering the lower water permeability of these microcapsules observed in Chapter 5 as well as their relatively thick walls. However, the TT microcapsules also suffered from severe salt egress due to the presence of micropores resulting from the presence of air bubbles in the shell phase during encapsulation. Under the cycle conditions it is possible that these micropores open and allow the core contents to leak and thus negating any mass transfer effects of the shell on the microcapsule. These regions are visible in the optical images in Figure 6.4, however, the loss of core (shown by a loss of dye) was not detected under wet conditions. Figure 6.5 also shows that the equilibrium water uptake varies for each sample as indicated by the variation in dry salt content for each microcapsule type represented by the loading capacity shown in Figure 6.2. This is a property

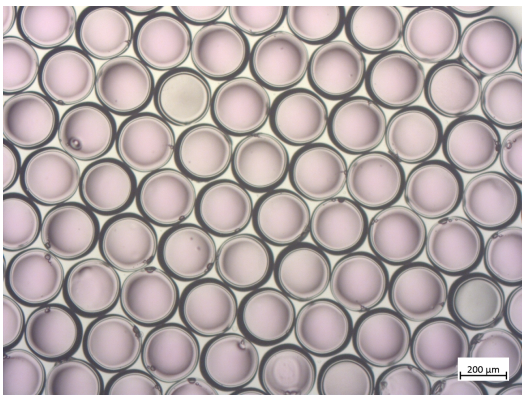

Figure 6.4: Air bubbles in TT microcapsule shells after polymerization.

not only affected by the salt content but may be affected by the encapsulating material. However, it is important to note that this effect is compounded by the sensitivity of the reaction rate to the sample mass (Gaeini et al. 2018).

Water uptake is shown to increase with the salt content. However, a high salt content may result in overfilled microcapsules as well as a reduction in sorption dynamics due to thick aggregates in the core. Condensation of water on the external surface of the microcapsules may lead to salt leaching by osmosis.

Figure 6.6 presents the data in terms of the conversion as a function of time. In this case, the water uptake is calculated relative to the estimated equilibrium loading on a dry mass basis according to the LDF model. This allows for differences in the microcapsule uptake rate to be compared more clearly. The profiles of the TT microcapsules are almost fully coincident with the lowest calculated characteristic time relative to the other microcapsules. The conversion profiles for the DT microcapsules are similarly close with the DT2 microcapsules having a larger characteristic time compared with DT1 microcapsules. This indicates a minor effect of particle size on the hydration

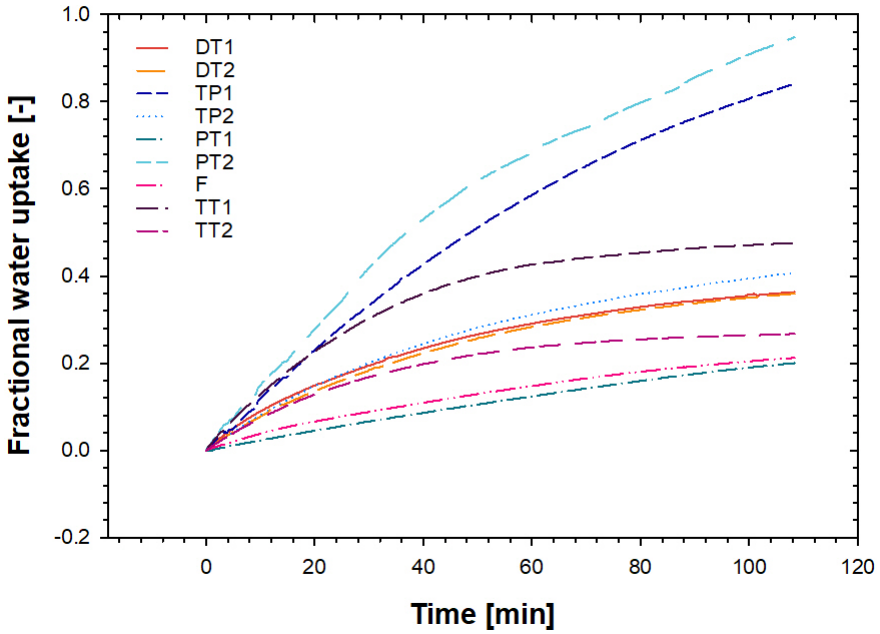

Figure 6.5: Water uptake on a dry mass basis for microcapsules with a $LiBr$ core.

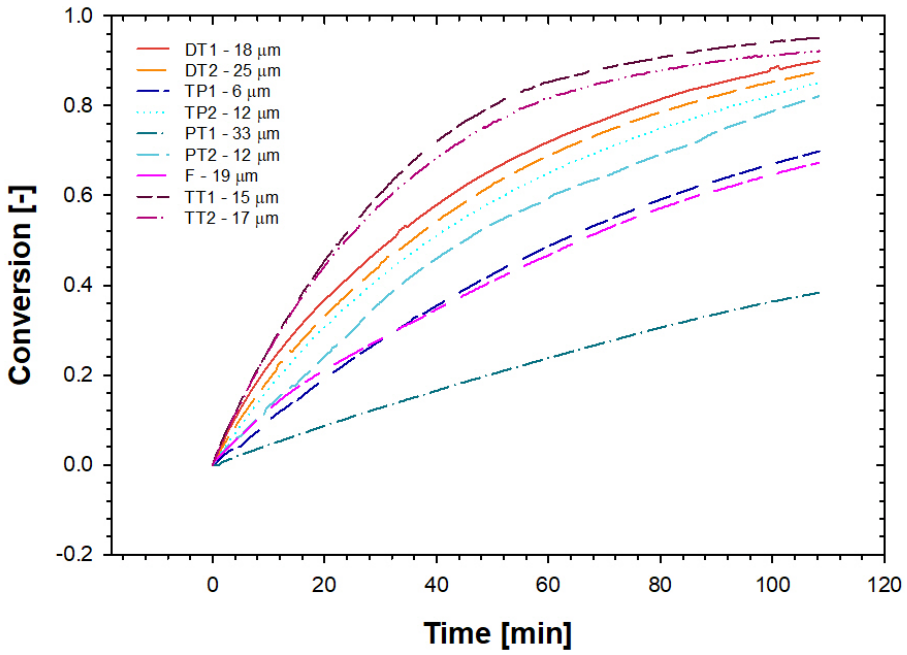

Figure 6.6: Dynamic conversion profiles of microcapsules with $LiBr$ core and varying shell material type and average thickness.

kinetics of these microcapsules and that mass transport is dominated by extra-particle factors.

The characteristic sorption time τ is an aggregative term of the overall sorption behaviour and is affected by the capsule size, shell thickness and permeability as well as the sample size. Microcapsules with a thicker shell of the same material will have reduced heat and mass transfer rate and this can be observed in the TP and PT samples which have thickness values of twice and 2.8 times the thickness of the thinner shelled capsule, respectively. The PT1 microcapsules with the thicker shell have a greater characteristic time of 210 min $\pm$ 12.6% compared with that of PT2 microcapsules of 67 min $\pm$ 1.2%. In contrast, the thinner-shelled TP1 microcapsules have a larger

characteristic time of 90 min ± 0.5% compared with that of the thicker-walled TP2 microcapsules at 55 min ± 0.9%. The characteristic times for all microcapsules are presented in Table 6.2.

To highlight the impact of shell thickness on the sorption behaviour of the microcapsules, their absolute shell thickness was considered. In this case, the minimum thickness and the max/min thickness ratio were considered as the most representative duplet as the minimum thickness is associated with the highest mass transfer rates across the shell and the max/min ratio reflects the shell inhomogeneity. These values are shown in the legend of Figure 6.6 and show that in general, microcapsules with thicker shells have lower rates of mass transfer, however, this will only be the case where the shell permeabilities are similar as reflected by the DT microcapsules with thick shells and high water uptake rates. In this case the water vapour permeability of the microcapsule has to be considered. Of the polymer shells studied here, the DT shell is the most hydrophilic with a water contact angle of 82.00 ± 1.83° and surface free energy of 41.46 ± 3.16 $mN\ m^{-1}$ (Appendix D). This is due in part to the glycol functional groups in the polymer structure which have been shown to enhance water transport within the polymer (Lundberg et al. 2010). This is also linked to polymer swellability due to water and is also a reflection of the cross-link density of the polymer. In general, with the exception of the TT and TP microcapsules, the characteristic time increased with material hydrophobocity as shown in Table 6.2 where the F and PT1 microcapsules had the longest chatacteristic times of 96.16 ± 0.50 min and 210 ± 26.61 min, respectively. The larger PT1 characteristic times can be explained considering the the thicker shells of these microcapsules, at 32.9 ±

Table 6.2: Chatacteristic times for microencapsulated sorbents as determined from a linear driving force model fitting.

Material	Contact angle [°]	Characteristic time (τ) [min]
TT1	84.75 ± 1.07	30.53 ± 0.03
TT2	84.75 ± 1.07	31.69 ± 0.09
DT1	82.00 ± 1.83	46.89 ± 0.57
DT2	82.00 ± 1.83	50.93 ± 0.23
TP2	70.05 ± 1.77	54.75 ± 0.51
PT2	91.25 ± 1.37	67.00 ± 0.82
DT3	82.00 ± 1.83	68.22 ± 0.87
TP1	70.05 ± 1.77	89.26 ± 0.44
F	113.00 ± 2.00	96.16 ± 0.50
PT1	91.25 ± 1.37	210.98 ± 26.61

0.4 μm, compared with the F microcapsules which had a shell thickness of 19.4 ± 0.3 μm and thus a lower mass transfer resistance.

6.2.4 Sorption dynamics of different salt cores

The sorption dynamics of the DT microcapsules was also studied with a core of $CaCl_2$ and compared with that of the LiBr core. Figure 6.7 shows the water uptake by the microcapsules at isothermal conditions over time. Water uptake rates with the two types of salts are comparable with average characteristic times of 47 min ± 1.2% and 68 min ± 1.3% for the DT1 and DT3 microcapsules, respectively. The driving force for absorption is the difference between the equilibrium vapour pressure of the core and that of the surroundings. Variation of the salt in the core varies the driving force for sorption as $CaCl_2$ has a higher equilibrium vapour pressure than LiBr at 30°C in the concentration range 40 – 60wt% (Conde 2004). Thus, it is expected that the rate of water uptake will be higher for microcapsules with

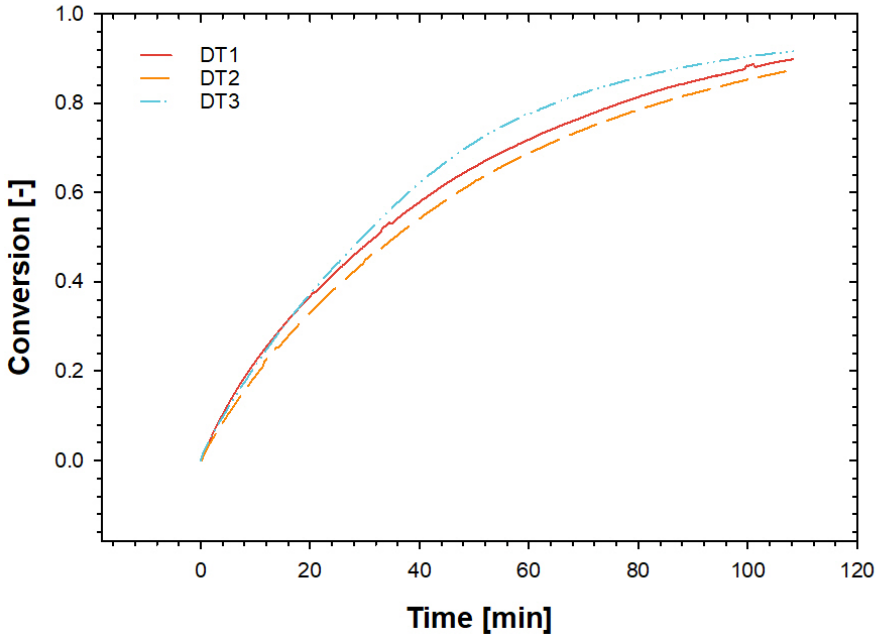

Figure 6.7: Dynamic conversion profiles of DT microcapsules with $LiBr$ and $CaCl_2$ core.

$LiBr$ compared with those with a core of $CaCl_2$ due to a higher driving force under isothermal conditions. The extent to which deliquescence has an impact on the mass transfer kinetics is beyond the scope of this work, however, it is important to highlight that the deliquescence point of $LiBr$ is 2 $mbar$ at 25°C compared with 7.8 $mbar$ at 25°C for $CaCl_2$ (Donkers et al. 2017). This is expected to have an impact on the mass transfer rates as in some composite adsorbents where it is posited that diffusion through the solution layer wetting the salt granule is the rate limiting step for mass transfer (Ostrovskii et al. 2007). For the case of DT microcapsules, only a minor difference in water uptake rate is observed.

6.3 Heat storage capacity

The enthalpy of hydration is compared to that of dehydration in Figure 6.8 obtained by integration of the heat-flow curves (DSC signal) in the absorption and desorption segments of the experimental measurement. There is a mismatch between the hydration and dehydration enthalpy values which vary by as much as 52% for the case of F microcapsules. This is explained by considering that the hydration process is slow compared to the dehydration process and the energy released is partially lost to the surroundings especially considering the high purge gas flowrates which act to enhance heat loss by convection. This is especially significant for cases where the absolute mass of absorbed water is relatively low compared to the sample dry mass which is 0.2 for F microcapsules. Additionally, the microcapsules are not packed in a monolayer in the test crucible and thus heat is not released uniformly throughout the sample and crucible walls for detection.

The energy storage capacity values per cycle are presented in Table 6.3 on a dry mass and water mass basis. The energy released per gram of desorbed water is comparable to the energy of vaporisation of water for most samples. For a process where the salt is fully dehydrated, it is expected that this value exceeds the enthalpy of vaporisation of water due to the solution enthalpy contribution of the salt. The energy storage capacity values on a water mass basis are consistent with those for a $LiBr$-H_2O absorption system that incorporates crystallisation in its cycle (Hui et al. 2011). For comparison of the energy storage potential of the microcapsules, the energy released when the fraction of absorbed water is 50% of the estimated equilibrium loading

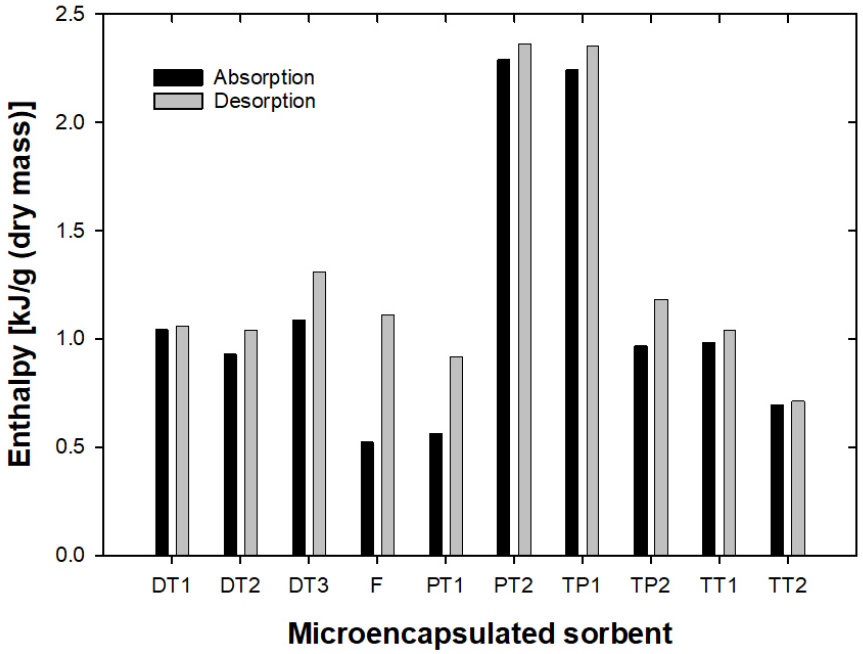

Figure 6.8: Comparison of water absorption and desorption enthalpies of microencapsulated sorbents on a dry mass basis.

Table 6.3: Energy storage capacity over the absorption cycle and average shell thickness values.

Microcapsule	Thickness	Energy storage capacity		Energy storage (half loading)	
	$[\mu m]$	$[kJ\ g^{-1}]$ (dry mass)	$[kJ\ g^{-1}]$ (water)	$[kJ\ g^{-1}]$ (dry mass)	$[kJ\ g^{-1}]$ (water)
DT1	18	1.1	2.9	0.58	2.84
DT2	25	1.0	2.8	0.61	2.98
DT3	11	1.3	1.6	0.59	1.72
F	19	1.1	4.9	0.39	2.41
PT1	33	0.9	4.1	0.57	2.56
PT2	12	2.4	2.9	1.77	3.01
TP1	6	2.4	4.0	2.03	3.16
TP2	12	1.2	4.7	0.69	2.86
TT1	15	1.0	2.5	0.73	3.04
TT2	17	0.7	1.0	0.39	2.98

is considered. The data are summarised in Table 6.3 on a dry mass basis of the microcapsules and show that under the test conditions considered in this work, the microcapsules have energy densities in the range of 742 $J\ g^{-1}$ to 2400 $J\ g^{-1}$ with the lowest range value associated with the TT2 microcapsules and the range maximum associated with the TP1 microcapsules.

Energy density values were calculated assuming the densest theoretical close-packed sphere scenario where the volume fraction of the spheres is 74% ($\frac{\pi}{3\sqrt{2}}$) with a sphere diameter equal to the mass weighted mean diameter of the microcapsules with a mass equivalent to the dry mass of the microcapsule. The mass density, ρ_{cap}, of the microcapsules is thus calculated as $\rho_{cap} = 0.74\frac{m_{cap}}{V_{cap}}$, where m_{cap} is the capsule mass and V_{cap} is the capsule volume. These values are presented in Table 6.4. The PT2 microcapsules have the highest energy density value of 2.52 $GJ\ m^{-3}$, this value is close

to the theoretical value for the total dehydration of a similar concentration $LiBr$ solution at 2.65 $GJ\ m^{-3}$ (Donkers et al. 2017). Although the TP1 microcapsules have the same enrgy storage capacity as PT2 microcapsules in Table 6.3, they have a lower volumetric energy density due to their larger size in spite of the high salt loading capacity values as shown in Table 6.4. This highlights the importance of microcapsule size in the formulation of these new composite materials. The lower volumetric energy storage density values obtained with the other samples can be explained lower water uptake due to thicker shells and lower salt loading. The simplified estimate of the volumetric energy density is dependent only on the capsule size, the shell thickness (or mass) and the salt content, however, variation of microcapsule size during the sorption process can lead to buckled capsules which may increase the packing density of the microcapsules affecting both the porosity of the packed bed and the volume of the sorption bed. The energy density values are comparable with those reported in the literature and fall in the range of 0.09 - 3.6 $GJ\ m^{-3}$ for sorption energy storage materials reviewed by Yu et al. (2013). Theoretical values of the energy storage density of the highest hydrates of $LiBr$ and $CaCl_2$ are 1.37 $GJ\ m^{-3}$ and 1.54 $GJ\ m^{-3}$, respectively, for a closed system (Donkers et al. 2017). Thus, encapsulation allows for the uptake of water beyond the deliquescence of the hygroscopic salt, increasing the total energy stored compared with the pure hydrates. However, the downside of this is that the energy will be delivered at a reduced discharging temperature (Hauer 2007). Such values are also dependent on the energy storage cycle, however, as a first approximation, they indicate that encapsulated sorbents may become an alternative composite material in

Table 6.4: Volumetric energy density of microcapsules with average microcapsule diameter, shell thickness and loading capacity.

Microcapsule	Diameter $[\mu m]$	Thickness $[\mu m]$	Loading [% (dry salt/total dry mass)]	Energy density $[GJ\ m^{-3}]$
DT1	251	18	52	1.12
DT2	421	25	74	1.09
DT3	386	11	64	0.67
F	270	19	51	0.76
PT1	370	33	36	0.82
PT2	309	12	69	2.52
TP1	390	6	86	1.40
TP2	310	12	45	1.15
TT1	256	15	60	0.70
TT2	236	17	53	0.6

sorption energy storage applications.

6.4 Stability: Salt loss and morphological changes

6.4.1 Cycle stability

The first and second absorption-desorption cycles of the microcapsules were compared in order to identify issues related to the cycle stability. Performance loss of the microencapsulated composite materials can be detected as a change in the loading capacity of water during the cycle. Such an effect could result from a loss of hygroscopic material or a reduction in the available surface area for mass transfer as a consequence of reduced porosity. Another possible manifestation of poor cycle stability can be observed as a change in the water uptake rate. For microencapsulated salts, an increase

in the surface salt due to leaking/leaching can lead to a raised initial uptake rate. In this context, leaking can be described as the loss of salt through pores or cracks in the shell whereas leaching involves the transport of the salt by diffusion through the shell. The cycle loading capacity and initial water uptake rates of successive cycles are compared for the microcapsules studied in this work in Figure 6.9. Values are compared against each other with the line drawn representing the cases where the values from each cycle coincide (y = x). Values below this line indicate a decrease in the parameter being compared in the second cycle. As only two cycles are compared in this work, only microcapsules with severe instability will have detectable change. PT2 microcapsules show a large drop in loading capacity between the first and second cycles of 23.8% whereas DT3 and TP2 microcapsules show a large rise of 41.6% and 16.5%, respectively. The TP1 microcapsules show little change in loading capacity compared with the TP2 microcapsules even though they have thinner shells. As the thinner shell in TP1 microcapsules is more likely to suffer from early salt leaching as a result of the shorter mass transfer distance of the shell, it is possible that significant salt leaching had already occurred during the initial drying cycle. The change in water loading capacity of the TP2 microcapsules also results in a 32.8% drop in the total desorption energy and highlights the impact of cycle stability on the energy storage performance of the material. The initial sorption rates are shown to be higher on the second cycle for the majority of microcapsules in Figure 6.9(b) with DT3 microcapsules showing the highest increase of 28.3% indicating salt loss in concurrence with the changes in loading capacity. The majority of microcapsules show little variation (within 10%) between the

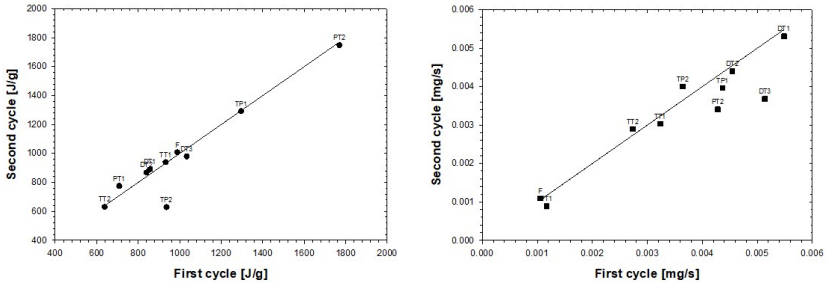

(a) Desorption enthalpies (b) Initial absorption rate

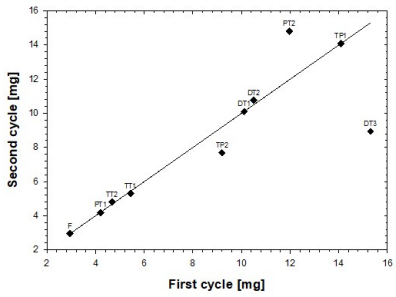

(c) Water vapour uptake

Figure 6.9: Comparison of (a) the desorption enthalpies, (b) the initial absorption rate and (c) water uptake of the first and second desorption cycles of microencapsulated sorbents.

two cycles, however, more rigorous cycle stability tests are required to fully characterise the differences in microcapsule properties that give rise to the variation in the extent of salt loss.

6.4.2 Salt loss

The SEMs of the microcapsules left to dry at ambient temperature in a vacuum desiccator overnight are shown in Figure 6.10. TT, DT and F microcapsules are presented with similar characteristics observed for all microcapsules in this study. The drying process is necessitated by the need to remove moisture prior to exposing the sample to the vacuum conditions in the SEM. This

inevitably means that any possible differences due to cycling or processing will be compromised in samples due to the SEM measurement conditions. Figure 6.10 reveals the extent of salt leaching through the polymer shell after drying conditions as white spots on the microcapsule surface. For the TT microcapsules where large pores due to air-bubbles were identified, extensive salt leaking is observed, localised at the microcapsule-microcapsule interfaces. This is caused by loss of core solution which collects at the liquid bridges of the microcapsule-microcapsule interface by capillary action and eventually dries, leaving the dry solute. For microcapsules where large pores are not present, closer inspection (see Figure 6.10(f)) shows that the surface near the salt crystal spots have no physical damage such as ripping or holes suggesting salt transport through the shell as the source of the salt crystal growth. The extent of salt leaching has not been quantified in this work, however, the shell material plays a significant role in that polymers with a high water permeability and swellability have a greater propensity for transport of the salt ions through the shell wall (Latnikova & Jobmann 2017). Thus, in this work, it is expected that the DT microcapsules will show the greatest propensity to leach and the superhydrophobic microcapsules, the least. The presence of this surface salt will result in higher rates of water uptake over repeated cycles as there is no mass transfer resistance due to the shell, however, a noticeable change depends on the amount of surface salt present.

Some of the microcapsules were split open with a scalpel prior to drying in order to reveal their internal structure as shown in Figure 6.11. DT microcapsules with $LiBr$ and $CaCl_2$ cores are also shown revealing the differences

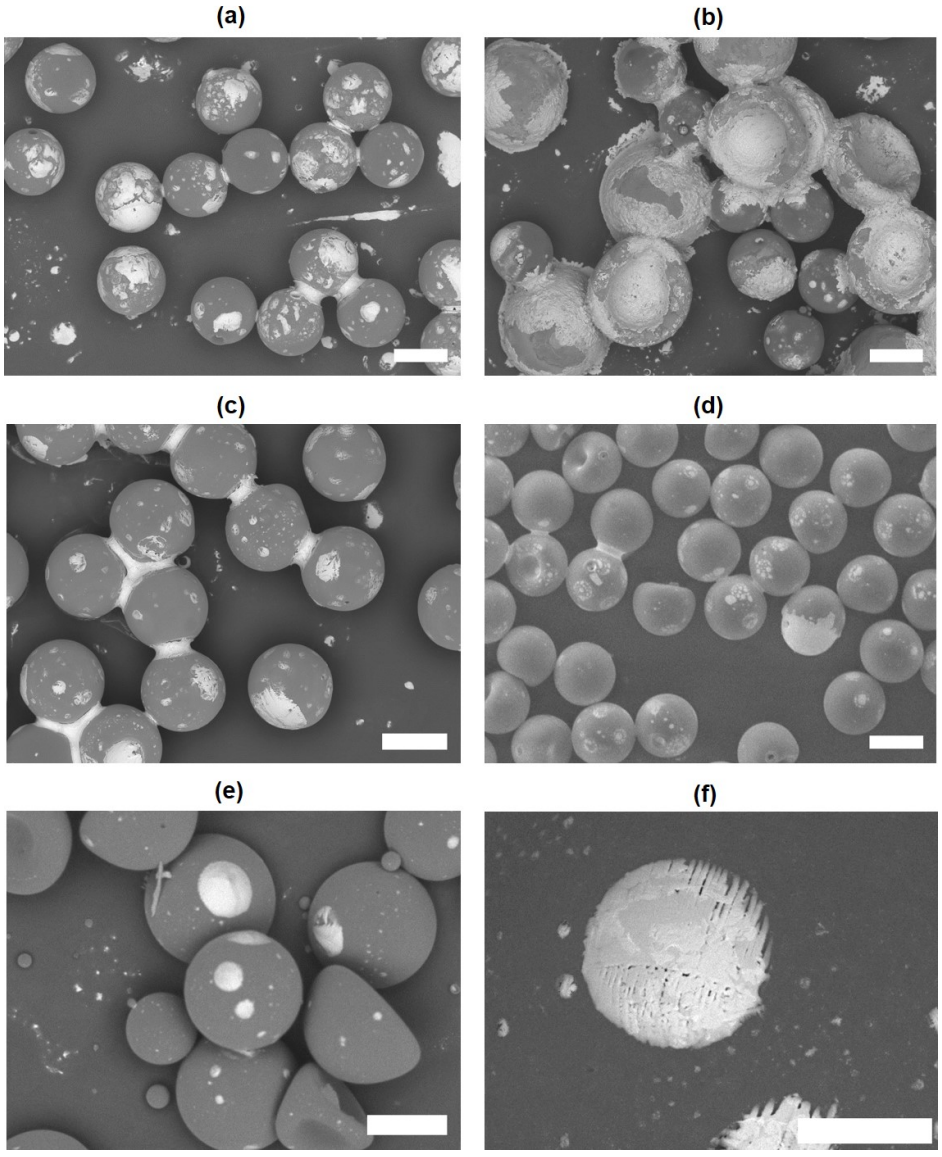

Figure 6.10: SEM images of (a) DT1, (b) DT3, (c) TT1, (d) TT2, (e) F microcapsules and (f) close-up of F microcapsules (Scale bar is 50 μm). Dried salt crystals are shown as white regions in the images. Scale bars measure 200 μm in length.

in the structure of the dried salt crystals in the internal microcapsules surface. The $LiBr$ salt forms a smoother salt layer on the internal surface compared with the uneven layer formed by $CaCl_2$ salt. Such a porous salt layer may present some mass transport benefits if microcapsules are considered for use in applications where extensive crystallization of the core salt is required. Traces of the solution released after splitting of the capsule can be seen as streaks on the conducting carbon pad surface indicating successful retention of the salt solution in the core. Inspection of the internal surface of the microcapsule shells reveals a layer of salt crystals lining the internal surface with a thickness in the order of 10 μm for the single measurement from Figure 6.11. The layer of salt is sectioned in the same location as the shell indicating that it was formed prior to sectioning. This reveals that during the desorption process, salt ions are rejected by the polymer shell and form a layer that grows towards the centre of the microcapsule as water vapour is lost. The growth of such a layer will present a resistance to mass transfer of water through the crystal layer as well as concentration polarization effects akin to membrane distillation where the driving force for desorption is reduced. For example, experimental work by Yun et al. (2006) with high concentration $NaCl$ solutions in direct contract membrane distillation showed a sharp decrease in water fluxes above a concentration of 25% $NaCl$. Such a drop in the rate of mass transfer would translate into increased energy consumption during the charging phase of the sorbent. Concentration polarization also impacts the membrane lifespan through increasing the propensity for salt leaching as well as fouling (Alkhudhiri et al. 2012). For conventional membranes, this problem is countered by the application of cross-flows on

the membrane surface as well as through the introduction of routine cleaning cycles (Alkhudhiri et al. 2012). However, for encapsulated liquid sorbents, the core fluid is expected to be stagnant and such internal surface flows are not likely. Nevertheless, for microcapsules that buckle due to a decrease in the internal volume as a result of solvent loss, the collapsing shell may act to disrupt the formation of an internal crust of salt, however, this requires further investigation.

6.4.3 Three-dimensional visualisation of morphological changes

The internal structure of the microcapsules was visualised using the non-destructive x-ray microtomography technique (micro-CT). As discussed in Section 6.4.2, formation of the salt crust inside the dry microcapsules may impact the shell material integrity, and micro-CT offers an alternative technique to SEM to study both the internal and external changes of microcapsules due to absorption/desorption cycling.

Sample holder and microcapsule mounting

An important aspect of micro-CT is the preparation of samples and their mounting on a rotating stage. For encapsulated sorbents, there is no established technique and thus the practical aspects involved are presented in this section. Figure 6.12 shows the three-dimensional images of DT1 and DT3 microcapsules along with the corresponding cross-sectional images. In the cross-sectional images of microcapsules with filled cores, the high-density regions consisting of the salt solution are represented by the white pixels

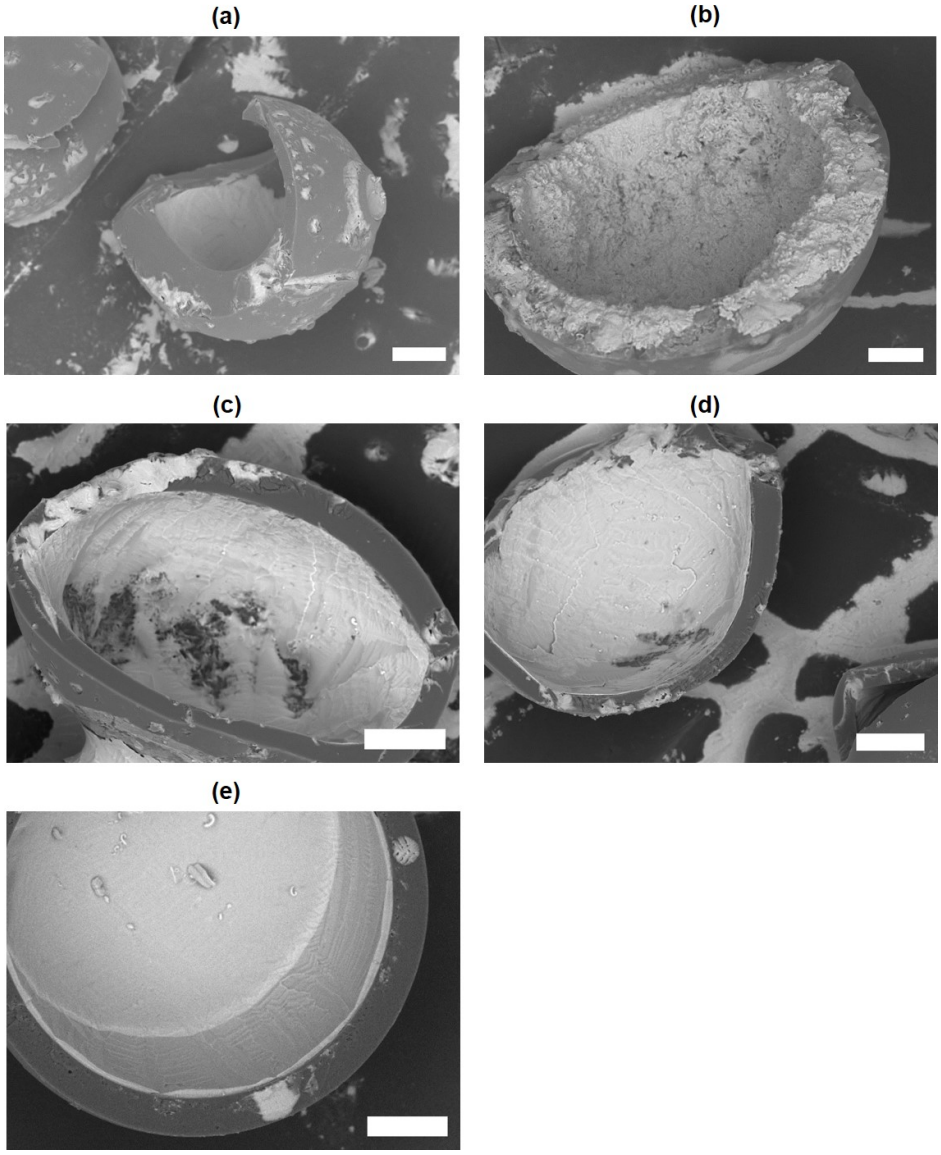

Figure 6.11: SEM images of sectioned (a) DT1, (b) DT3, (c) TT1, (d) TT2 and (e) F microcapsule. Salt crystals appear white in the images. The scale bars measure 50 μm in length.

and the less dense polymer shell, grey, whilst the black regions represent air as the least dense material. The microcapsules are evenly dispersed on a layer of double-sided tape attached to the outer surface of a cylinder of low-density material (cocktail straw). The diameter of the polymeric cylinder is approximately 3 mm which allows for close approach of the x-ray source. The image pixel size attained with this set-up was 2.89 $\mu m\ pixel^{-1}$ which is approximately half the thinnest shell of the microcapsules studied in this work. Additionally, the rigid cylinder ensures that the microcapsules are supported securely throughout the measurement as the sample is rotated whilst the adhesive tape prevents movement of the individual microcapsules thus avoiding the need to embed the microcapsules in a resin. Since the polymeric microcapsule shell has a relatively low density, it would be challenging to distinguish from an embedding resin. The three-dimensional images reveal the spherical nature of the filled DT1 microcapsules in contrast to the buckled, partially dry DT3 microcapsules. Through this visual medium, the size distribution can also be visualised with the bimodality of the size distribution of DT3 microcapsules readily recognisable with almost two distinct particle sizes.

Figure 6.13 is a cross-sectional image of a single microcapsule with the accompanying histogram showing the intensity along the line shown. The core and shell regions are distinguishable, however, the boundary between the two is not entirely distinct but rather a continuous combination of intensity contributions from both the shell and core materials. This indicates that the actual thickness of the microcapsule shell is dependent on the criterion of intensity thresholding.

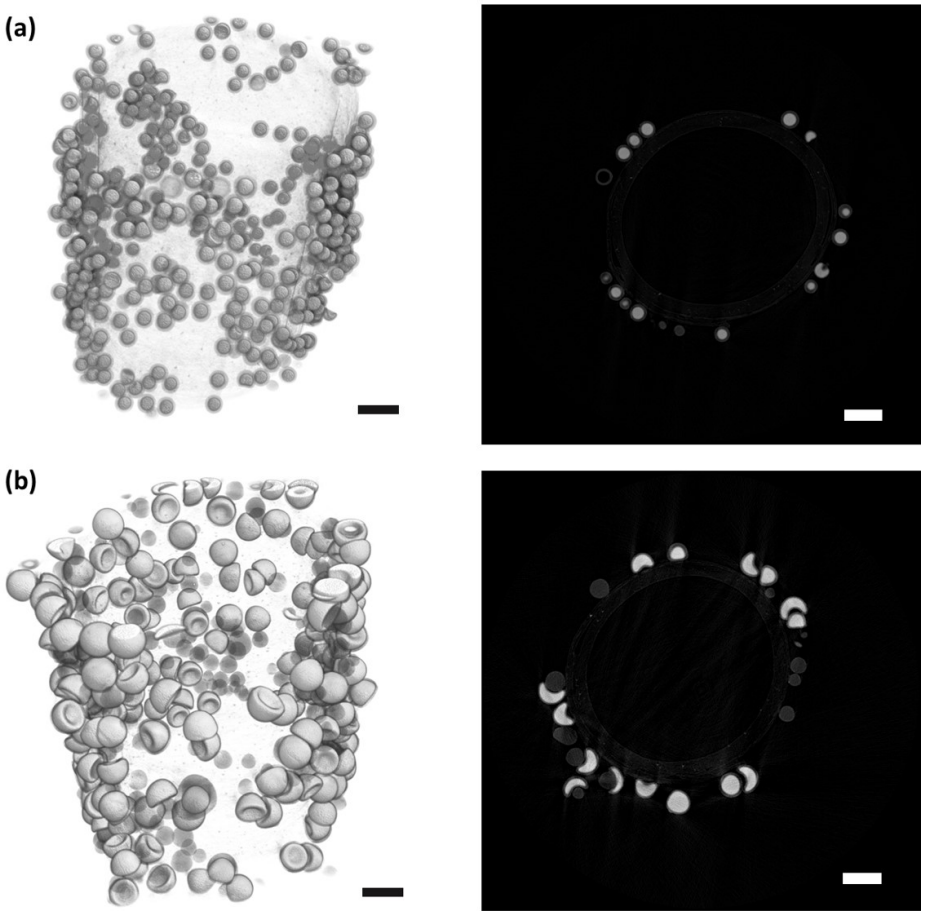

Figure 6.12: Three-dimensional (left) and 2D representation (right) of (a) DT1 and (b) DT3 microcapsules. Scale bars are 500 μm.

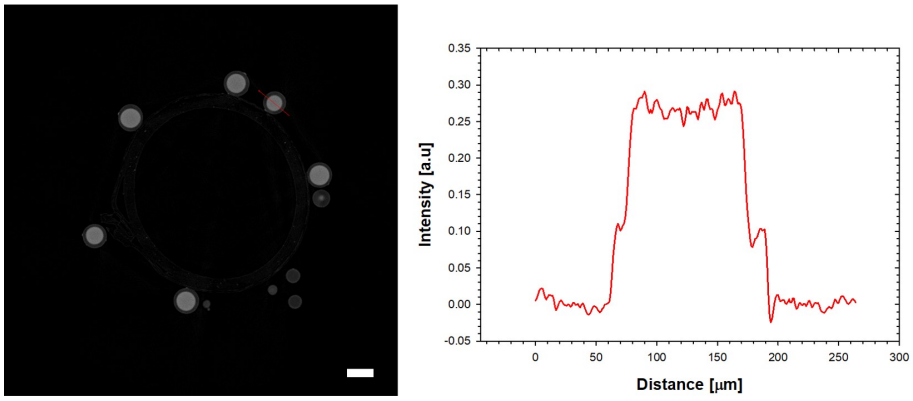

Figure 6.13: Cross-sectional image and accompanying histogram showing attenuation of x-rays along a line through a single microcapsule. Scale bar is 200 μm.

Image processing for visualisation

A critical step in micro-CT analysis is in selecting the appropriate region of interest (ROI) for further 3D analysis. It is important that this ROI is representative of the sample. Thus, in this study, it was necessary to isolate the microcapsules from the straw by implementing a unique series of image analysis steps using the cTAN image processing software (Bruker, USA). These steps are summarised in Figure 6.14 and begin with (a) thresholding the reconstructed greyscale image to isolate only those pixels associated with the straw followed by (b) de-speckling to remove the small, isolated white pixels and filling in pores to reveal the region enclosed by the straw; this is then followed by (c) sweeping to remove all white pixels except those belonging to the largest object (straw) and finally (d) performing a bitwise operation to specify all regions outside the straw as the ROI. As the density values of the straw and polymer shell are close, there is an unavoidable loss in information (pixels) associated with the thresholding. Different thresholding

Table 6.5: Mean and modal microcapsules and core diameters of DT2 microcaspules as determined from optical microscopy and microCT measurements.

Method	Microcapsule diameter $[\mu m]$		Core diameter $[\mu m]$	
	Mean	Mode	Mean	Mode
Optical microscopy	422.2	407.5	374.5	355.0
MicroCT	292.1	375.1	271.2	285.8

values were required for each type of shell material, however, the same values were used for the same shell and core material type.

The defined ROI allows for the thresholding of the original greyscale image to isolate the whole microcapsules, the cores only and the shell material taken as the difference between the microcapsule and core images as shown in Figure 6.15.

A three-dimensional representation of the microcapsules can thus be reconstructed to reveal the location of the salt, shell thickness and size distribution of the microcapsules visually as shown in Figure 6.16 for DT2 microcapsules.

As an example, the size-distribution data and volume fraction of the core are compared in Figure 6.17 and Table 6.5 for DT2 microcapsules. In all cases the diameter measurements by micro-CT underestimate the microcapsule sizes. Distributions by micro-CT also have a long tail at the smaller sizes in the distribution due to the presence of specks as a result of the thresholding, this reduces the mean diameters calculated further. However, the smaller sizes are most likely due to the loss of information due to thresholding influenced by bias arising from the thresholding process.

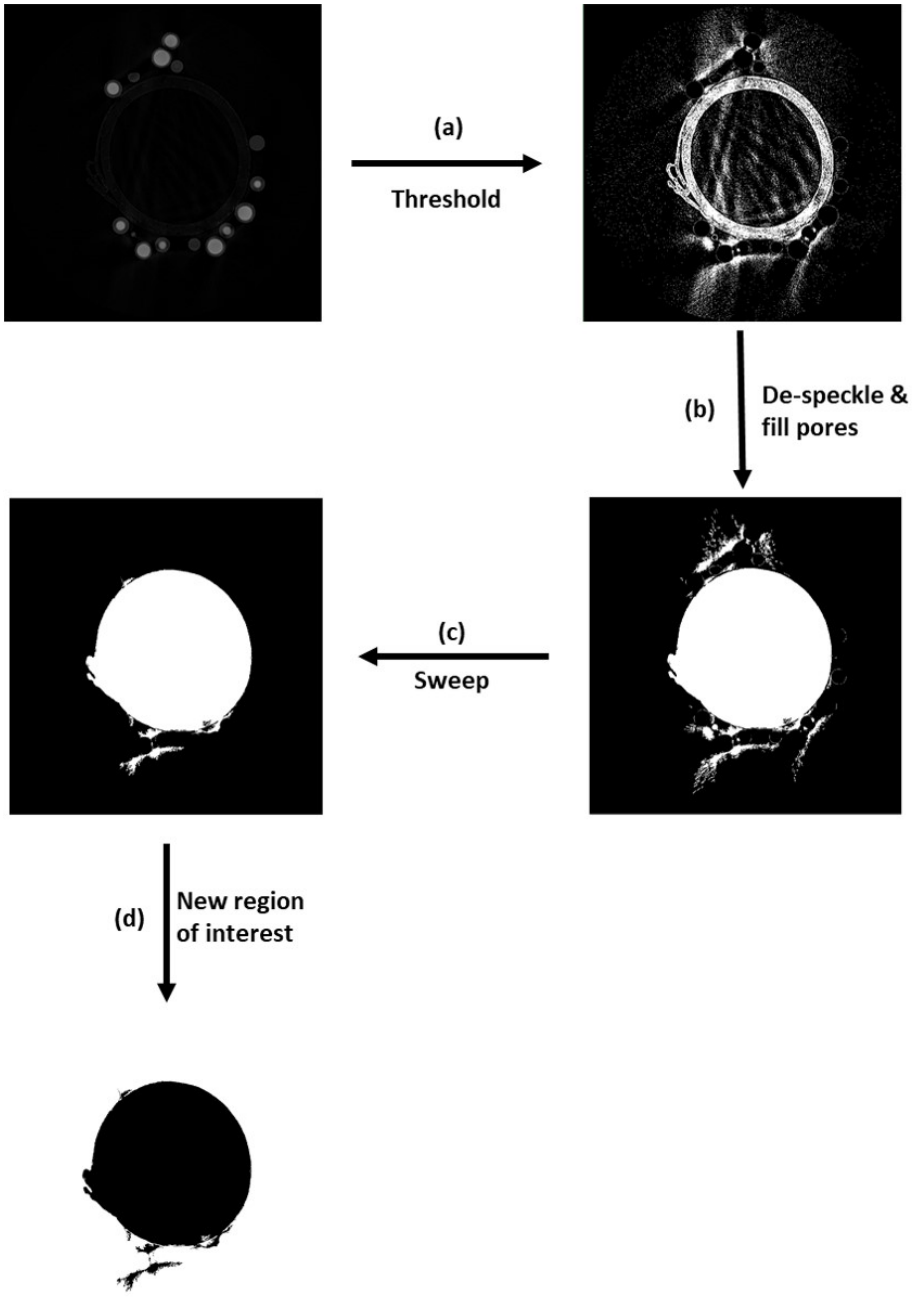

Figure 6.14: Procedure for removal of supporting straw from region of interest in image processing.

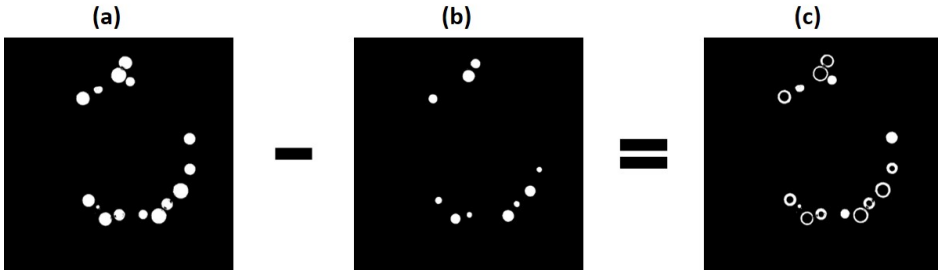

Figure 6.15: Threshold images showing the (a) microcapsules, (b) cores and bitwise operation to obtain the (c) shells o the microcapsules.

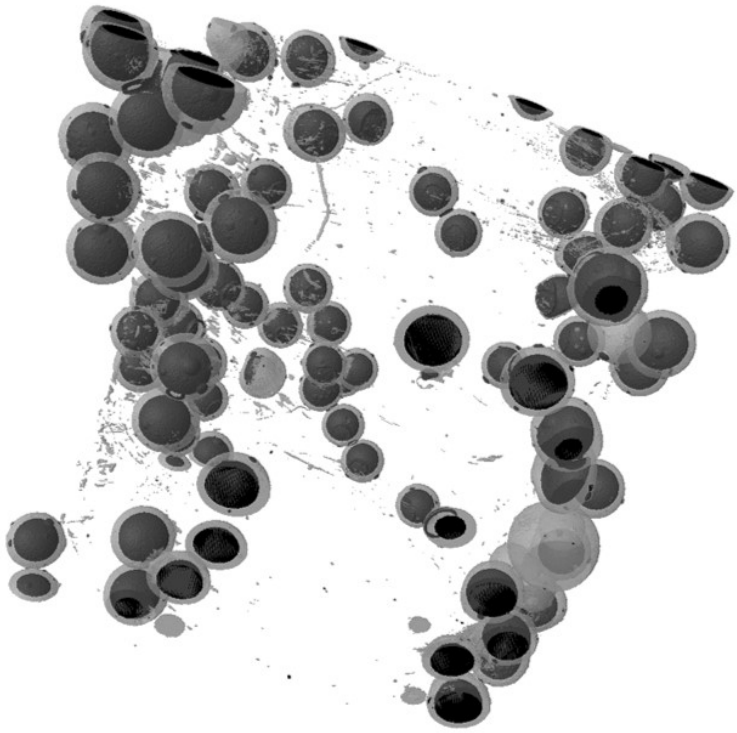

Figure 6.16: Three-dimensional representation of DT2 microcapsules revealing the cores (black) and shells (grey) of microcapsules.

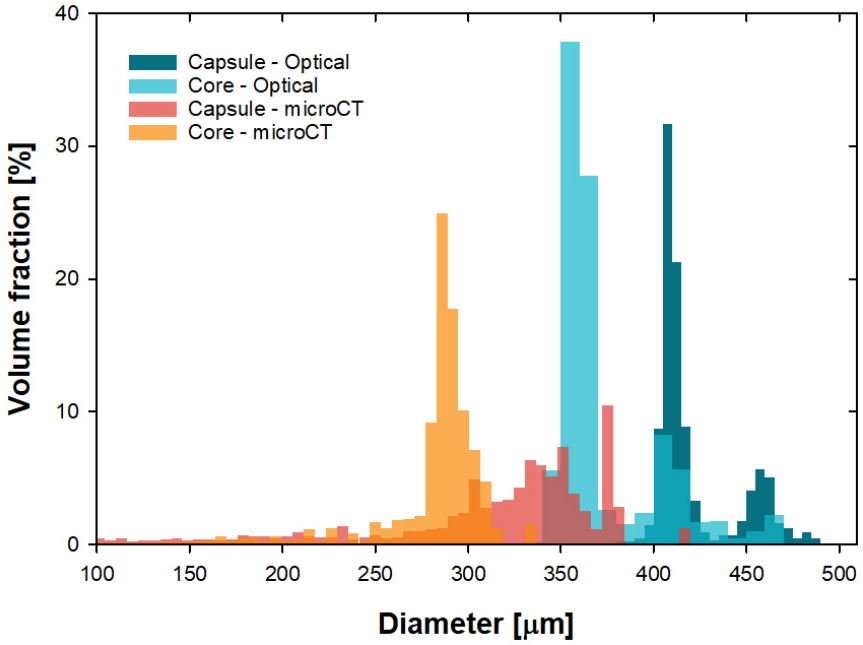

Figure 6.17: Comparison of volume size distributions determined by optical microscopy and microCT for DT2 microcapsules.

Detection of salt leaching

The limitations in using micro-CT to measure microcapsule size parameters have been demonstrated in the previous section, however, the non-destructive nature of the measurement technique allows for visualisation of the microcapsules after sorption-desorption cycling in three-dimensions. Cross-sectional images of the dried microcapsules after adsorption-desorption cycling are presented in Figure 6.18. The internal structure of the dried DT2 microcapsules is revealed and shows the internal salt crust identified in the split microcapsules in the SEM images shown in Figure 6.11. The images also show that the salt crust does not always cover the entire surface indicating that a cavity is formed inside the microcapsule during desorption. However, this is not the case for buckled TP2 microcapsules as shown in Figure 6.18(b) where surface contact with the liquid core is maintained throughout the desorption process. The buckled microcapsules indicate that the salt is agglomerated in the final dried capsule and does not form a crust as in the microcapsules that do not collapse. This result shows that there will be a variation in the surface-to-volume ratio of the salt which will impact the water uptake rate over subsequent cycles. An improvement could be to reduce the microcapsule size and thus the bulk dried particles will have a larger surface-to-volume ratio of the salt.

The images also show the degree of salt loss post cycling with the thin-walled TP1 microcapsules showing an extensive loss of salt from the core with the final microcapsule shell remaining hollow in Figure 6.18(c). The expected driving force for salt leaching is a concentration gradient across the

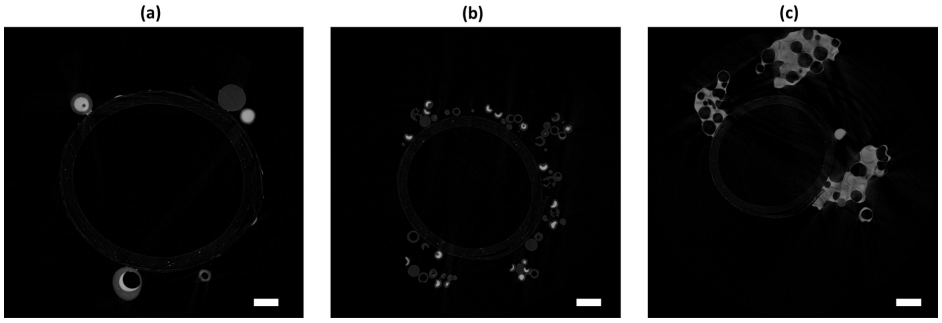

Figure 6.18: Extent of salt loss for (a) DT2, (b) TP2 and (c) TP1 microcapsules after absorption-desorption cycling.

shell and thus complete loss of the core from the shell is not theoretically possible. Such extensive loss of encapsulated salt is better explained by catastrophic rupture of the thin shell (circ. 6 μm) due to excessive loading or the presence of macropores. The thicker-walled TP2 and DT2 microcapsules show a more moderate salt leaching after cycling as shown by the relatively few salt crystals on the external microcapsule surface compared with the salt in the core.

A three-dimension representation of the DT2 microcapsules before and after absorption-desorption cycling is presented in Figure 6.19. Visualisation of the salt (black), reveals the extent of salt loss in the inter-capsule regions of Figure 6.19 (right).

6.5 Summary

The sorption dynamics of microcapsules of varying shell material with a core of hygroscopic salt solution were investigated and their energy storage capacities measured. The simultaneous thermal analysis technique was used to characterise the dynamic response of the microcapsules which were exposed

Figure 6.19: Three-dimension representation of the DT2 microcapsules before and after absorption-desorption cycling is presented. Scale bar is 500 μm.

to a water vapour partial pressure of 9.7 $mbar$ at 30°C for 120 min followed by a desorption step in which the temperature was raised to 150°C.

Thiol-ene-based (DT, PT, TP and TT) and a photopolymerizable fluoropolymer (F) were used as shell material to encapsulate $LiBr$ solution. The DT shell material was further used to encapsulate $CaCl_2$ salt solution for comparison with the $LiBr$ core. The microcapsule dynamics were compared by fitting TG results to a linear driving force (LDF) model with the characteristic time representing the overall sorption behaviour. It was shown that in general, the characteristic time increased with material hydrophobocity. The more hydrophilic DT microcapsules (contact angle (CA) = 82.00 ± 1.83°)had a characteristic times of 46.89 ± 0.03 min and 50.93 ± 0.93 min whereas the more hydrophobic F (CA = 113 ± 2°) and PT1 microcapsules(CA = 91.25 ± 1.37°) had characteristic times of 96.16 ± 0.50 min and 210 ± 26.61 min, respectively. The PT1 microcapsules had a much thicker shell (32.9 ± 0.4 μm) compared with the F microcapsules (19.4 ± 0.3 μm), indicating the influence of the shell thickness on the aggregative term that is

the characteristic time. The core material was also shown to have an impact on the characteristic time of the microcapsules where DT microcapsules with a $LiBr$ core had a shorter characteristic time of $46.89 \pm 0.57\ min$ compared with that of DT microcapsules with $CaCl_2$ at $68.22 \pm 0.87\ min$. This was explained by considering that $LiBr$ solutions present a higher vapour pressure difference than $CaCl_2$ solutions under the conditions considered, and thus greater water uptake rates.

The energy storage densities of the encapsulated sorbents were shown to be comparable to those currently in the literature.The PT2 microcapsules had the highest energy density value of $2.52\ GJ\ m^{-3}$ whereas the TT2 microcapsules had the lowest energy density value of $0.60\ GJ\ m^{-3}$. The results indicate the feasibility of the implementation of optimised encapsulated sorbents in real systems. The microcapsules allowed for deliquescence of the internal salt and subsequent drying to form a layer of salt along the internal surface of the microcapsule. Visualisation of split microcapsules by SEM revealed that a layer of salt was formed in microcapsules with both $LiBr$ and $CaCl_2$. Such a layer could impact the sorption rates in dried microcapsules, acting as a diffusion barrier. The initial and second hydration/dehydration cycles were compared on the basis of loading capacity and initial rates to examine the microcapsule cycle stability. Salt leaching as evidenced by a combination of SEM and micro-CT measurements was shown to be the lead cause of cycle instability, however, this challenge can be addressed by refinement of the microcapsule shell thickness and composition

CHAPTER 7

Conclusions and future work

7.1 Overall conclusions

A flow-focusing glass capillary microfluidic device was developed for the production of microcapsules with a core of thermochemical materials, $LiBr$ and $CaCl_2$. The device assembly consisted of the use of pre-fabricated glass capillaries with circular and square cross-sections of different aperture sizes which eliminated the need for capillary tapering and grinding/etching. This improved the reproducibility of the devices and reduced the device assembly time as well as the need to use hazardous chemical etchants such as hydrofluoric acid. Furthermore, the use of 3D-printed connectors was implemented in the assembly process to improve capillary alignment.

The flow conditions for water-in-oil-in-water (w/o/w) double emulsion generation in the microfluidic devices were identified by varying inner, middle and outer fluid flowrates. The oil phase consisted of a series of thiol-ene

based photopolymers and an acrylate-based fluorophotopolymer with varying viscosity, density and interfacial tension. Single oil droplets, core-shell double emulsion droplets and multi-core double emulsion droplet morphologies were produced. The dripping to jetting transition was shown to be in agreement with the semi-empirical model developed by Nabavi & Vladisavljević (2017). The alternate production of o/w and w/o/w emulsion droplets was observed in the decussate regime which allowed for the simultaneous formation of microcapsules and solid polymer particles of the shell material. This droplet formation mode was shown to be useful for the investigation of the mechanical properties of microcapsules by micromanipulation as the bulk shell material properties could be determined from tests on the solid spheres produced at similar conditions to the corresponding microcapsules. The influence of Capillary numbers of the middle (Ca_2) and outer (Ca_3) fluids were shown to have a strong impact on the decussate droplet formation. Increasing Ca_2 from 1.0×10^{-4} to 1.3×10^{-4} whilst holding Ca_1 (Capillary number of the inner fluid) and Ca_3 constant, doubled the number of single emulsion droplets per double emulsion droplet produced. A further increase in Ca_2 from 1.3×10^{-4} to 3.1×10^{-4} lead to the formation of larger o/w emulsion droplets with pinch-off of both the single and double emulsion droplets occurring simultaneously. By adjusting both values of (Ca_2) and (Ca_3) to 7.5×10^{-5} and 4.1×10^{-3}, respectively, the frequency of single emulsion droplets was increased to 5 droplets per double emulsion droplet and their size reduced by $\sim 57\%$. Therefore showing how the flow parameters can be controlled in the decussate regime such that double and single emulsions could be separated easily on the basis of size.

Microcapsules with a water core and three types of shell material were produced from the photopolymerization of the thiol-ene resins of the thiols pentaerythritol tetrakis(3-mercaptopropionate), trimethylolpropane tris(3-mercaptopropionate), 2,2'-(Ethylenedioxy)diethanethiol in combination with the alkene 1,3,5-tri-allyl-1,3,5-triazine-2,4,6(1H,3H,5H)-trione to form the shell materials TT, PT and DT. The thiol monomers had four, three and two reactive thiol groups, respectively and thus, different degrees of crosslinking density. Size distribution data determined from optical measurements showed that the PT microcapsules had the largest average diameter 332.3 $\pm$ 1.3 μm followed by the DT, TT1 and TT2 microcapsules with $d_{4,3}$ values of 277.8 $\pm$ 1.0 μm, 260.1 $\pm$ 0.5 μm and 231.3 $\pm$ 0.4 μm, respectively. Additionally, there was variability in both the average shell thickness and loading capacity with the microcapsule diameter. Shell inhomogeneity was also characterised by the ratio of the maximum to minimum thickness (max/min ratio) of the shell. The mechanical properties of these microcapsules were measured using the micromanipulation technique which revealed elastic deformation behaviour for the DT and PT microcapsules whereas the TT microcapsules displayed "elastic-plastic" deformation behaviour. This was consistent with the DSC results for the neat shell materials which showed glass transition temperatures in the range -20$^{\circ}C$ to 45$^{\circ}C$. This verified that the DT and PT microcapsules were in the "rubbery" state whereas the TT microcapsules were in the "glassy" state at the measurement temperature. This was explained in terms of the number of functional groups in each thiol monomer type where monomers with a greater number of thiol groups lead to greater cross-linking and thus higher glass transition temperatures.

Formed polymer particles of the shell material in the decussate regime were utilised to estimate the Young's moduli from the Hertz model. The Young's moduli of the DT, PT and TT shell materials were determined to be 14.8 ± 0.4 MPa, 9.3 ± 0.3 MPa and 555.3 ± 0.9 MPa, respectively. It was indicated that the difference in these values from the literature values could arise from the wet conditions in which the polymer particles are produced which may lead to the presence of other species in the polymer which may lower the measured values. Thus, it is shown that shell material properties may not be equivalent to the bulk polymer properties produced and measured under different conditions. The decussate production of such particles and microcapsules presents an opportunity for determining the bulk shell properties at the microcapsule conditions.

Nominal rupture stress values were determined to be higher for the DT microcapsules followed by PT and TT microcapsules. These values were shown to be impacted by the shell inhomogeneity of the microcapsules with weaker microcapsules also having high max/min ratios. Water-loss rates determined by thermogravimetry under isothermal conditions decreased with increasing glass transition temperatures and could be explained on the basis of cross-linking. Buckling of all the microcapsules at ambient conditions was verified for all microcapsule types and theoretical predictions of the buckling pressure indicate that buckling is most likely as a consequence of capillary forces in the shell membrane arising from the evaporation of the water core.

The force-displacement data for the DT and PT microcapsules fit well to the Tatara model up to fractional deformations of 0.6 and the good fitting to the Hertz model was obtained with the TT microcapsules up to a fractional

deformation of 0.1. However, such model fittings and the measured nominal rupture strength values of the microcapsules are only a first approach to the true microcapsule material properties on account of volume loss from the permeable shell. A true core-shell model that accounts for shell thickness, thermally-dependent mechanical properties and compressibility of the microcapsule needs to be developed for encapsulation processes involving volume changes of the core with large temperature changes.

The sorption dynamics of microcapsules of varying shell material with a core of hygroscopic salt solution were investigated and their energy storage capacities were measured. Microcapsules were exposed to a relative humidity of 23% at 30°C for 120 min followed by a desorption step in which the temperature was raised to 150°C. Thiol-ene-based polymers (DT, PT, TP and TT) and a photopolymerizable fluoropolymer (F) were used as shell material to encapsulate 1 $g\ cm^{-3}$ aqueous $LiBr$ solution. The DT shell material was also used to encapsulate 0.75 $g\ cm^{-3}$ aqueous $CaCl_2$ solution for comparison with the $LiBr$ core. Microcapsule sorption dynamics were compared by fitting TG results to a linear driving force (LDF) model from which a characteristic time, allowing for comparison of the sorption behaviour of the different composites, could be determined. In general, the characteristic time was shown to increase with material hydrophobocity. The more hydrophilic DT microcapsules (contact angle (CA) = 82.00 ± 1.83°)had a characteristic times of 46.89 ± 0.03 min and 50.93 ± 0.93 min whereas the more hydrophobic F (CA = 113 ± 2°) and PT1 microcapsules(CA = 91.25 ± 1.37°) had longer characteristic times, at 96.16 ± 0.50 min and 210 ± 26.61 min, respectively. Furthermore, the effect of shell thickness on the characteristic

time was demonstrated by the fact that the thicker walled PT1 microcapsules ($32.9 \pm 0.4\ \mu m$) had larger characteristic times compared with the more hydrophobic F microcapsules with thinner shell measuring $19.4 \pm 0.3\ \mu m$. DT microcapsules with a $LiBr$ core had a shorter characteristic time of $46.89 \pm 0.57\ min$ compared with that of DT microcapsules with $CaCl_2$ at $68.22 \pm 0.87\ min$. This was explained by considering that $LiBr$ solutions present a higher vapour pressure difference than $CaCl_2$ solutions under the conditions considered, and thus greater water uptake rates. Thus by adjusting the shell thickness and core material type, the sorption kinetics can be tailored to a specific application.

The energy storage densities of the encapsulated sorbents were shown to be in the range $0.60\ GJ\ m^{-3}$ ($742\ J\ g^{-1}$) to $2.52\ GJ\ m^{-3}$ ($2400\ J\ g^{-1}$) for TT2 and PT2 microcapsules, respectively. These values were shown to be comparable to those of matrix-based composites in the literature. This demonstrates that encapsulated thermochemical materials have the potential of avoiding the issues of over-hydration encountered with matrix-based TCM materials whilst maintaining their high energy storage density properties. The microcapsules allowed for deliquescence of the internal salt and subsequent drying to form a layer of salt along the internal surface of the microcapsule. Visualisation of split microcapsules by SEM revealed that for $LiBr$ salt, this layer was dense and smooth whereas that formed from $CaCl_2$ salt was rough. Visualisation of split microcapsules by SEM revealed that a layer of salt was formed in microcapsules with both $LiBr$ and $CaCl_2$. Such a layer could impact the sorption rates in dried microcapsules, acting as a diffusion barrier. The initial and second hydration/dehydration cycles were

compared on the basis of loading capacity and initial rates to examine the microcapsule cycle stability. Salt leaching as evidenced by a combination of SEM and micro-CT measurements was shown to be the lead cause of cycle instability, however, this challenge can be addressed by refinement of the microcapsule shell thickness, composition and core material sorption properties, including diffusivity, selectivity and hydrophobicity.

7.2 Future work

This work has addressed the key factors for microfluidic device fabrication as well as the main characterisation techniques for validating new encapsulated sorbents for sorption thermochemical energy storage. One of the main challenges of working with microencapsulated hygroscopic salts is in ensuring their retention in the shell. This is governed by the properties of the shell material and its permeability to both water vapour and salt ions. Additionally, formation of the salt crust at the membrane interface upon total dehydration of microcapsules can occur and is a condition most conventional desalination membrane systems avoid due to fouling issues. Three possible routes are proposed for the optimisation of encapsulated sorbents in TCM applications: a) The development of polymer shell materials with improved permeability and selectivity properties ensuring higher water vapour permeability and greater salt ion rejection. The modularity of thiol-ene chemistry makes this a possible route for development in this regard as thiol and alkene functionality can be grafted onto suitably identified polymer precursors. Additionally, the currently available thiol-ene polymers themselves can be modi-

fied by chemical oxidation with hydrogen peroxide solution to raise their glass transition temperatures and alter their salt transport properties; b) Performing sorption-desorption cycles with microcapsules avoiding total dehydration and formation of the salt crust. c) The utilisation of larger molecules that are compatible with hygroscopic salts such as ethanol could be used with possibly reduced salt loss or salt ions with larger hydration diameters and lower mobility through polymer membranes such as $SrBr_2$. However, the implementation of points (b) and (c) depend on the cost to the final energy storage performance in each case.

The buckling and compression-induced water loss demonstrated in this work presents an opportunity for increasing the driving force during desorption or recharging of encapsulated TCM materials. Compression of microcapsules in a packed bed due to a gas flow can lead to significant solvent loss as observed by Finn et al. (2019). Thus, by leveraging the mechanical compression and low temperature heat sources, the heat requirements for the desorption process may be reduced. This presents a new possibilty for improving the energy efficiency of sorption systems.

Appendices

APPENDIX A

Corrected flowrates

Table A.1 presents the corrected flowrates used in subsequent calculations of the flow parameters in Chapter 4.

Table A.1: Set and recorded flowrates of fluids in microfluidic devices.

Fluid			Set flowrate $[\mu L\ hr^{-1}]$			Measured flowrate $[\mu L\ hr^{-1}]$	
Core	Middle	Continuous	Q1	Q2	Q3	Q1	Q2
LiBr	DT	PEG20-15	500	700	5000	474	360
LiBr	DT	PEG20-15	200	300	2000	101	320
LiBr	DT	PEG20-15	500	900	5000	581	837
LiBr	DT	PEG20-15	300	500	3000	215	204
LiBr	DT	PEG20-15	300	600	8000	137	351
Water	DT	PEG20-15	300	300	5000	282	220
LiBr	DT	PEG20-15	500	300	5000	463	272
CaCl2	DT	PEG20-15	500	700	5000	854	416
LiBr	PT	PEG20-15	300	250	2500	170	206
LiBr	PT	PEG20-15	400	300	5000	489	137
Water	PT	PEG20-15	400	300	5000	536	272
LiBr	PT	PEG20-15	500	500	10000	365	355
LiBr	PT	PEG20-15	500	800	10000	702	589
Water	PT	PEG20-15	300	300	5000	328	276
LiBr	PT	PEG20-15	300	300	5000	280	173
LiBr	PT	PEG20-15	200	300	5000	306	187
LiBr	TP	PEG20-15	400	150	3000	475	67
LiBr	TP	PEG20-15	300	600	6000	386	629
Water	TT	PEG20-20	250	150	6000	402	247
Water	TT	PEG20-15	300	400	5000	487	406
LiBr	TT	PEG20-5	100	100	10000	103	57
LiBr	TT	PEG20-5	100	300	10000	90	134
LiBr	TT	PEG20-5	200	100	7000	206	60
LiBr	TT	PEG20-5	200	100	10000	253	77

APPENDIX B

Alternative glass capillary microfluidic geometries

An alternative MFD geometry was experimentally investigated for the production of microcapsules with an ultrathin shell in a two-step emulsification process based on the work of Kim et al. (2011). As shown in Figure 16, the device consists of a tapered glass injector capillary from which a binary fluid of inner fluid plugs carried in the middle phase is focussed in the collector capillary to form emulsion droplets. Figure 15 shows the droplet production process as the plugs flow through the injector capillary. When an oil plug is flowing, oil droplets are formed until a plug of the inner phase reaches the injector capillary outlet where emulsion droplets are formed with a thin middle layer. The middle phase forms droplets of the same diameter as the emulsion droplets in contrast to those formed in the work of Kim et al. (2011), where the oil plug formed a single large droplet. The plug flow was formed upstream of the injector capillary by injecting the inner phase using

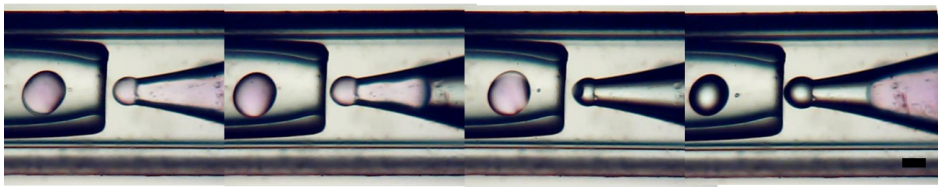

Figure B.1: Double emulsion production from water-in-oil plugs. Scale bar is 200 μm

a smaller square capillary inserted inside the injector capillary. The surface of the injector capillary is modified with hydrophobic silane to ensure the middle phase flows along the wall of the injector capillary.

Increasing the inner fluid flowrate in-order-to increase the fraction of double emulsion droplets produced resulted in a splitting of the streams. This also occurred over time at lower flowrates of the inner phase due to loss of the hydrophobic surface coating. In order to have a higher efficiency of double emulsion droplet production, the flow criteria of the inner and middle phases must satisfy the conditions set by Guillot et al. (2007) whilst maintaining a low enough overall flowrate to form emulsion droplets at the exit. Due to the relative complexity in the device assembly, issues with maintaining concentric flows and a desired broader range of shell thicknesses the capsule production was based solely on the simpler design discussed earlier.

APPENDIX C

Error estimates from the LDF model

The error in the estimate of the characteristic time and equilibrium loading in sorption experiments is dependent on the absorption run time with respect to the characteristic time (t_{ext}/τ) as shown in Figure C.2. Thus variation in the error as a function of t_{ext}/τ was simulated in Matlab for a general LDF model with random noise (Figure C.1)in order to estimate percentage error in the parameters.

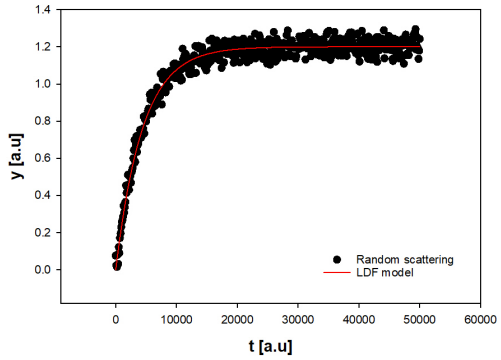

Figure C.1: Linear driving force model fitting (line) to randomised model data (dots).

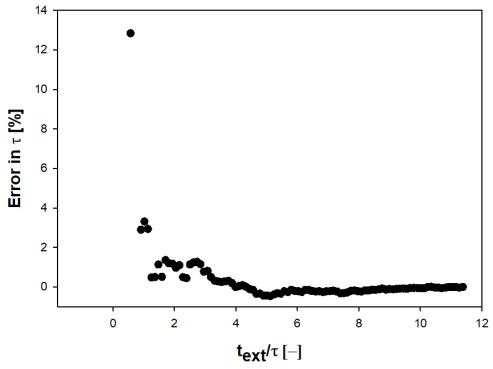

Figure C.2: Error in model characteristic time estimates as a function of the extent of run (t_{ext}) of the sorption experiment.

APPENDIX D

Contact angle and surface free energy of microcapsule shell materials

Table D presents the contact angle and interfacial tension data for the oil phases used to form double emulsions and microcapsules in Chapter 4.

Values for F (MD700) obtained from Solvay Specialty Chemicals.

Table D.1: Water contact angle and surface free energy of thiol-ene polymers.

Material	Mean Contact angle [°]	Surface free energy $[mN\ m^{-1}]$	Disperse $[mN\ m^{-1}]$	Polar $[mN\ m^{-1}]$
DT	82.00 ± 1.83	41.46 ± 3.16	38.37 ± 2.43	3.08 ± 0.72
PT	91.25 ± 1.37	39.28 ± 2.86	38.41 ± 2.52	0.87 ± 0.34
TP	70.05 ± 1.77	49.93 ± 1.52	43.58 ± 0.75	6.35 ± 0.77
TT	84.75 ± 1.07	49.78 ± 0.54	48.79 ± 0.35	0.99 ± 0.19
F	113 ± 2	-	-	-

APPENDIX E

Average shell thickness derivation and core radius measurement

E.1 Derivation of the average shell thickness

The derivation of $\overline{h}$ was performed from the geometry of a hypothetical microcapsule cross-section as shown in Figure E.1.

$$l^2 = b^2 \ + \ (f+R)^2 - 2b(f+R)cos(\frac{\pi-\theta}{2})$$

$$l^2 = 2R^2(1 - cos\theta) \ + \ (f+R)^2 - 2\sqrt{2}\ R\ (f+R)\ \sqrt{1-cos\theta}\ cos(\frac{\pi-\theta}{2})$$

$$average\ l^2 = \frac{1}{\pi}\left[\int_0^{\pi} l^2 d\theta\right]$$

$$average\ l^2 = \frac{1}{\pi}\left[2R^2(\theta - sin\theta) + (f+R)^2\theta - 2\sqrt{2}R(f+R)\frac{\sqrt{1-cos\theta}(\theta - sin\theta)}{2sin(\frac{\theta 2}{)}}\right]_0^{\pi}$$

$$\text{average } l^2 = 2R^2 + f^2 + 2fR + R^2 - 2fR - 2R^2$$

$$average\ l^2 = f^2 + R^2$$

$$therefore\ \overline{h} = \sqrt{f^2+R^2} \ - \ r$$

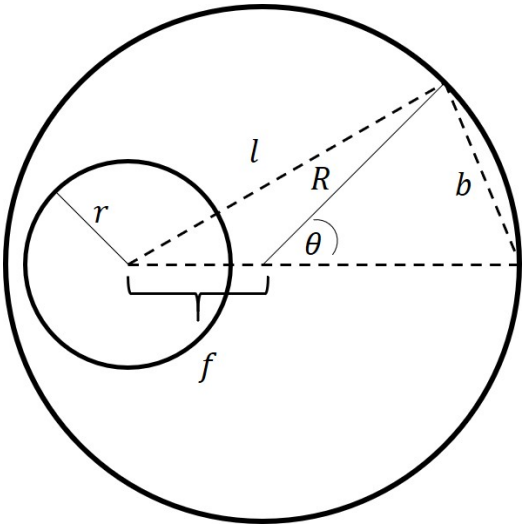

Figure E.1: Schematic of the cross-sectional profile of a microcapsule with asymmetrical core.

E.2 Core radius measurement variability

In three dimensions, the radius of the core r in the projected 2D image represented in Figure E.1 will vary depending to vertical position of the core relative to the focal plane when a 2D image is captured. As a first approach to investigate the effect of the vertical position (z-diraction in Cartesian coordinates) of the core on the measured radius in 2D, the measured "2D radius" for the core centred at several x-y-z coordinates within the microcapsule was used to generate a frequency distribution of the average thickness for microcapsules of different core volume fractions as shown in Figure E.2. It can be seen that at high volume fractions, the error in the measured radius will be small.

To generate Figure E.2, it was assumed that a spherical core of radius r_c centred at position (x_c, y_c, z_c) within the microcapsule can be represented

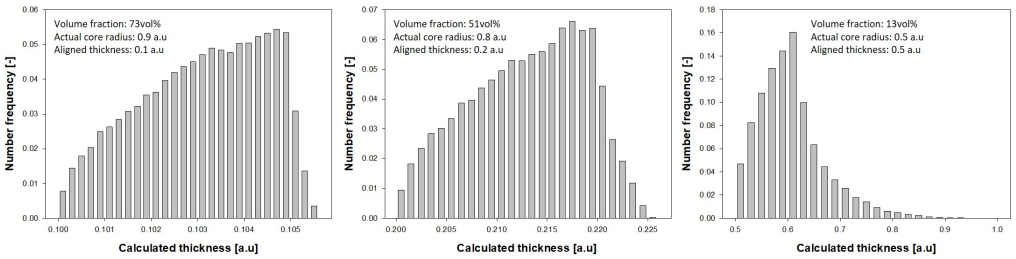

Figure E.2: Frequency distribution of the average thickness for microcapsules of different core volume fractions generated by varying the position of the core within the microcapsules.

by the equation $(x - x_c)^2 + (y - y_c)^2 + (z - z_c)^2 = r_c^2$ and intersects the focal plane ($z = 0$), to define a circle of radius r according to the equation $(x - x_c)^2 + (y - y_c)^2 = r^2$, where $r^2 = r_c^2 - z_c^2$. Thus the average thickness can be determined from the equation $\overline{h} = \sqrt{x_c^2 + y_c^2 + R^2} - \sqrt{r_c^2 - z_c^2}$, at several positions of the core to generate the frequency plots in Figure E.2.

Bibliography

Abate, A. R., Krummel, A. T., Lee, D., Marquez, M., Holtze, C. & Weitz, D. A. (2008), 'Photoreactive coating for high-contrast spatial patterning of microfluidic device wettability', *Lab on a Chip* **8**(12), 2157–2160.

Alkhudhiri, A., Darwish, N. & Hilal, N. (2012), 'Membrane distillation: A comprehensive review', *Desalination* **287**, 2 – 18. Special Issue in honour of Professor Takeshi Matsuura on his 75th Birthday.

Alva, G., Lin, Y., Liu, L. & Fang, G. (2017), 'Synthesis, characterization and applications of microencapsulated phase change materials in thermal energy storage: A review', *Energy and Buildings* **144**, 276–294.

Amato, D. (2018), Functional Emulsions via Thiol-Ene Chemistry, PhD thesis, University of Southern Mississippi.

Amato, D. V., Lee, H., Werner, J. G., Weitz, D. A. & Patton, D. L. (2017), 'Functional Microcapsules via Thiol–Ene Photopolymerization in Droplet-Based Microfluidics', *ACS Applied Materials & Interfaces* **9**(4), 3288–3293.

Aristov, Y. I. (2007*a*), 'New family of solid sorbents for adsorptive cooling: Material scientist approach', *Journal of Engineering Thermophysics* **16**(2), 63–72.

Aristov, Y. I. (2007*b*), 'Novel Materials for Adsorptive Heat Pumping and Storage: Screening and Nanotailoring of Sorption Properties', *JOURNAL OF CHEMICAL ENGINEERING OF JAPAN* **40**(13), 1242–1251.

Aristov, Y. I. (2012), 'Adsorptive transformation of heat: Principles of construction of adsorbents database', *Applied Thermal Engineering* **42**, 18–24.

Arshady, R. (1992), 'Suspension, emulsion, and dispersion polymerization: A methodological survey', *Colloid and Polymer Science* **270**(8), 717–732.

Artioli, Y. (2008), Adsorption, *in* S. E. Jørgensen & B. Fath, eds, 'Encyclopedia of Ecology', Academic Press, Oxford, pp. 60–65.

Aydin, D., Casey, S. P. & Riffat, S. (2015), 'The latest advancements on thermochemical heat storage systems', *Renewable and Sustainable Energy Reviews* **41**, 356–367.

Aymerich, M., Gómez-Varela, A. I., Álvarez, E. & Flores-Arias, M. T. (2016), 'Study of Different Sol-Gel Coatings to Enhance the Lifetime of PDMS Devices: Evaluation of Their Biocompatibility', *Materials (Basel, Switzerland)* **9**(9), 728.

Azarmanesh, M., Farhadi, M. & Azizian, P. (2016), 'Double emulsion formation through hierarchical flow-focusing microchannel', *Physics of Fluids* **28**(3), 032005.

Bandulasena, M. V., Vladisavljević, G. T. & Benyahia, B. (2019), 'Versatile reconfigurable glass capillary microfluidic devices with Lego® inspired blocks for drop generation and micromixing', *Journal of Colloid and Interface Science* **542**, 23–32.

Bardy, D. A., Cruickshank, C. A., Tezel, F. H., Carrier, Y. H. & Wong, B. (2020), 'An experimental investigation of fixed and fluidized beds as adsorbers in compact thermal energy storage systems', *Journal of Energy Storage* **31**, 101648.

Bell, S. (1996), 'A guide to the measurement of humidity'.

Brancato, V., Calabrese, L., Palomba, V., Frazzica, A., Fullana-Puig, M., Solé, A. & Cabeza, L. F. (2018), 'MgSO4·7H2O filled macro cellular foams: An innovative composite sorbent for thermo-chemical energy storage applications for solar buildings', *Solar Energy* **173**, 1278–1286.

Brancato, Vincenza, Gordeeva, L. G., Sapienza, A., Palomba, V., Vasta, S., Grekova, A. D., Frazzica, A. & Aristov, Y. I. (2018), 'Experimental characterization of the LiCl/vermiculite composite for sorption heat storage applications', *International Journal of Refrigeration* .

Brown, M. E. (2001), *Introduction to Thermal Analysis : Techniques and Applications*, Vol. 2 of *Hot Topics in Thermal Analysis and Calorimetry*, Springer, Dordrecht.

Cabeza, L. F., Solé, A. & Barreneche, C. (2017), 'Review on sorption materials and technologies for heat pumps and thermal energy storage', *Renewable Energy* **110**, 3–39.

Casey, S. P., Elvins, J., Riffat, S. & Robinson, A. (2014), 'Salt impregnated desiccant matrices for 'open' thermochemical energy storage—Selection, synthesis and characterisation of candidate materials', *Energy and Buildings* **84**, 412–425.

Chan, E.-S., Lim, T.-K., Voo, W.-P., Pogaku, R., Tey, B. T. & Zhang, Z. (2011), 'Effect of formulation of alginate beads on their mechanical behavior and stiffness', *Particuology* **9**(3), 228–234.

Chen, P. W., Cadisch, G. & Studart, A. R. (2014), 'Encapsulation of Aliphatic Amines Using Microfluidics', *Langmuir* **30**(9), 2346–2350.

Chen, Y., Wu, L. & Zhang, L. (2015), 'Dynamic behaviors of double emulsion formation in a flow-focusing device', *International Journal of Heat and Mass Transfer* **82**, 42–50.

Cheng, L. Y. (1987), 'Deformation analyses in cell and developmental biology. part i—formal methodology', *Journal of Biomechanical Engineering* **109**(1), 10–17.

Conde, M. R. (2004), 'Properties of aqueous solutions of lithium and calcium chlorides: formulations for use in air conditioning equipment design', *International Journal of Thermal Sciences* **43**(4), 367–382.

Coupier, G., Djellouli, A. & Quilliet, C. (2019), 'Let's deflate that beach ball', *The European Physical Journal E* **42**(9), 129.

Courbon, E., D'Ans, P., Permyakova, A., Skrylnyk, O., Steunou, N., Degrez, M. & Frère, M. (2017), 'A new composite sorbent based on SrBr2 and silica gel for solar energy storage application with high energy storage density and stability', *Applied Energy* **190**, 1184–1194.

Crank, J. (1979), *The mathematics of diffusion*, Oxford university press.

Darkwa, K., Ianakiev, A. & O'Callaghan, P. W. (2006), 'Modelling and simulation of adsorption process in a fluidised bed thermochemical energy reactor', *Applied Thermal Engineering* **26**(8), 838–845.

Datta, S. S., Kim, S.-H., Paulose, J., Abbaspourrad, A., Nelson, D. R. & Weitz, D. A. (2012), 'Delayed Buckling and Guided Folding of Inhomogeneous Capsules', *Physical Review Letters* **109**(13), 134302.

Dawoud, B. & Aristov, Y. (2003), 'Experimental study on the kinetics of water vapor sorption on selective water sorbents, silica gel and alumina under typical operating conditions of sorption heat pumps', *International Journal of Heat and Mass Transfer* **46**(2), 273–281.

De La Vega, J. C., Elischer, P., Schneider, T. & Häfeli, U. O. (2013), 'Uniform polymer microspheres: monodispersity criteria, methods of formation and applications', *Nanomedicine* **8**(2), 265–285.

DeLassus, P. (2002), 'Barrier Polymers'.

Donkers, P., Sögütoglu, L., Huinink, H., Fischer, H. & Adan, O. (2017), 'A review of salt hydrates for seasonal heat storage in domestic applications', *Applied Energy* **199**, 45–68.

Ebrahimi, M. & Keshavarz, A. (2015), 8 - CCHP Thermal Energy Storage, *in* M. Ebrahimi & A. Keshavarz Heating and Power, eds, 'Combined Cooling, Heating and Power', Elsevier, Boston, pp. 183–188.

Erb, R. M., Obrist, D., Chen, P. W., Studer, J. & Studart, A. R. (2011), 'Predicting sizes of droplets made by microfluidic flow-induced dripping', *Soft Matter* **7**(19), 8757.

Fan, Y. & Luo, L. (2017), Energy Storage by Sensible Heat for Buildings, *in* R. Wang & X. Zhai, eds, 'Handbook of Energy Systems in Green Buildings', Springer Berlin Heidelberg, Berlin, Heidelberg, pp. 1–41.

Fei, Z., Wang, T., Fan, P., Chen, F. & Zhong, M. (2017), 'Facile preparation of crosslinked pan membranes based on thiol-ene photopolymerization', *Polymers* **9**(9), 390.

Feng, W. W. & Yang, W.-H. (1973), 'On the Contact Problem of an Inflated Spherical Nonlinear Membrane', *Journal of Applied Mechanics* **40**(1), 209–214.

Finken, R., Kessler, S. & Seifert, U. (2011), 'Micro-capsules in shear flow', *Journal of Physics: Condensed Matter* **23**(18), 184113.

Finn, J. R. & Galvin, J. E. (2018), 'Modeling and simulation of CO2 capture using semipermeable elastic microcapsules', *International Journal of Greenhouse Gas Control* **74**, 191–205.

Finn, J. R., Galvin, J. E., Panday, R. & Ashfaq, H. (2019), 'Deformation and water loss from solvent filled microcapsules under compressive loads', *AIChE Journal* p. e16905.

Frazzica, A. & Freni, A. (2017), 'Adsorbent working pairs for solar thermal energy storage in buildings', *Renewable Energy* **110**, 87–94.

Frazzica, A., Sapienza, A. & Freni, A. (2014), 'Novel experimental methodology for the characterization of thermodynamic performance of advanced working pairs for adsorptive heat transformers', *Applied Thermal Engineering* **72**(2), 229–236.

Gaeini, M., Rouws, A., Salari, J., Zondag, H. & Rindt, C. (2018), 'Characterization of microencapsulated and impregnated porous host materials based on calcium chloride for thermochemical energy storage', *Applied Energy* **212**, 1165–1177.

Giro-Paloma, J., Martínez, M., Cabeza, L. F. & Fernández, A. I. (2016), 'Types, methods, techniques, and applications for microencapsulated phase change materials (MPCM): A review', *Renewable and Sustainable Energy Reviews* **53**, 1059–1075.

Gokmen, M. T., Van Camp, W., Colver, P. J., Bon, S. A. F. & Du Prez, F. E. (2009), 'Fabrication of Porous "Clickable" Polymer Beads and Rods through Generation of High Internal Phase Emulsion (HIPE) Droplets in a Simple Microfluidic Device', *Macromolecules* **42**(23), 9289–9294.

Gordeeva, L. G. & Aristov, Y. I. (2011), 'Composite sorbent of methanol "LiCl in mesoporous silica gel" for adsorption cooling: Dynamic optimization', *Energy* **36**(2), 1273–1279.

Gothsch, T., Schilcher, C., Richter, C., Beinert, S., Dietzel, A., Büttgenbach, S. & Kwade, A. (2015), 'High-pressure microfluidic systems (HPMS): flow and cavitation measurements in supported silicon microsystems', *Microfluidics and Nanofluidics* **18**(1), 121–130.

Gouedard, C., Picq, D., Launay, F. & Carrette, P.-L. (2012), 'Amine degradation in CO2 capture. I. A review', *International Journal of Greenhouse Gas Control* **10**, 244–270.

Guillot, P., Colin, A., Utada, A. S. & Ajdari, A. (2007), 'Stability of a Jet in Confined Pressure-Driven Biphasic Flows at Low Reynolds Numbers', *Physical Review Letters* **99**(10), 104502.

Handscomb, C. S., Kraft, M. & Bayly, A. E. (2009), 'A new model for the drying of droplets containing suspended solids after shell formation', *Chemical Engineering Science* **64**(2), 228–246.

Hauer, A. (2007), 'Evaluation of adsorbent materials for heat pump and thermal energy storage applications in open systems', *Adsorption* **13**(3), 399–405.

Hench, L. L. & West, J. K. (1990), 'The sol-gel process', *Chemical Reviews* **90**(1), 33–72.

Hess, K. S. (2012), Generation of colloidal granules and capsules from double emulsion drops, PhD thesis, Purdue University, Ann Arbor.

Hoyle, C. E. & Bowman, C. N. (2010), 'Thiol–Ene Click Chemistry', *Angewandte Chemie International Edition* **49**(9), 1540–1573.

Hoyle, C. E., Nazarenko, S. & Wei, H. (2013), 'Photocuable thiol-ene low gas permeability membranes'.

Hui, L., Edem, N. K., Nolwenn, L. P. & Lingai, L. (2011), 'Evaluation of a seasonal storage system of solar energy for house heating using different absorption couples', *Energy Conversion and Management* **52**(6), 2427–2436.

Hussain, F., Rahman, M. Z., Sivasengaran, A. N. & Hasanuzzaman, M. (2020), Chapter 6 - Energy storage technologies, *in* M. D. Hasanuzzaman & N. Rahim, eds, 'Energy for Sustainable Development', Academic Press, pp. 125–165.

I Ré, M. (1998), 'Microencapsulation by Spray Drying', *Drying Technology* **16**(6), 1195–1236.

Jabbari-Hichri, A., Bennici, S. & Auroux, A. (2015), 'Enhancing the heat storage density of silica–alumina by addition of hygroscopic salts (CaCl2, Ba(OH)2, and LiNO3)', *Solar Energy Materials and Solar Cells* **140**, 351–360.

Jamekhorshid, A., Sadrameli, S. M. & Farid, M. (2014), 'A review of microencapsulation methods of phase change materials (PCMs) as a thermal energy storage (TES) medium', *Renewable and Sustainable Energy Reviews* **31**, 531–542.

James, J. D., Ludwick, J. M., Wheeler, M. L. & Oyen, M. L. (2020), 'Compressive failure of hydrogel spheres', *Journal of Materials Research* **35**(10), 1227–1235.

Jarimi, H., Aydin, D., Yanan, Z., Ozankaya, G., Chen, X. & Riffat, S. (2018), 'Review on the recent progress of thermochemical materials and processes for solar thermal energy storage and industrial waste heat recovery', *International Journal of Low-Carbon Technologies* **14**(1), 44–69.

Johnson, K. L. (1985), *Contact Mechanics*, Cambridge University Press, Cambridge.

Kalogirou, S. A. & Florides (2016), Solar Space Heating and Cooling Systems, *in* 'Reference Module in Earth Systems and Environmental Sciences', Elsevier.

Keller, M. W. & Sottos, N. R. (2006), 'Mechanical properties of microcapsules used in a self-healing polymer', *Experimental Mechanics* **46**(6), 725–733.

Kim, B., Jeon, T. Y., Oh, Y.-K. & Kim, S.-H. (2015), 'Microfluidic Production of Semipermeable Microcapsules by Polymerization-Induced Phase Separation', *Langmuir* **31**(22), 6027–6034.

Kim, S.-H., Kim, J. W., Cho, J.-C. & Weitz, D. A. (2011), 'Double-emulsion drops with ultra-thin shells for capsule templates', *Lab Chip* **11**(18), 3162–3166.

Kirinčič, S. & Klofutar, C. (1999), 'Viscosity of aqueous solutions of poly(ethylene glycol)s at 298.15 K', *Fluid Phase Equilibria* **155**(2), 311–325.

Knuutila, H., Svendsen, H. F. & Anttila, M. (2009), 'CO2 capture from coal-fired power plants based on sodium carbonate slurry; a systems feasibility and sensitivity study', *International Journal of Greenhouse Gas Control* **3**(2), 143–151.

Krajišnik, D., Čalija, B. & Cekić, N. (2017), Chapter 2 - Polymeric Microparticles and Inorganic Micro/Nanoparticulate Drug Carriers: An Overview and Pharmaceutical Application, *in* B. B. T. M. Čalija & N. C. for Nonsteroidal Anti-Inflammatory Drugs, eds, 'Microsized and Nanosized Carriers for Nonsteroidal Anti-Inflammatory Drugs', Academic Press, Boston, pp. 31–67.

Kwisnek, L. (2011), Photopolymerized Thiol-ene Networks for Gas Barrier and Membrane Applications, PhD thesis, University of Southern Mississippi.

Kwisnek, L., Goetz, J., Meyers, K. P., Heinz, S. R., Wiggins, J. S. & Nazarenko, S. (2014), 'PEG Containing Thiol–Ene Network Membranes for CO 2 Separation: Effect of Cross-Linking on Thermal, Mechanical, and Gas Transport Properties', *Macromolecules* **47**(10), 3243–3253.

Kwisnek, L., Nazarenko, S. & Hoyle, C. E. (2009), 'Oxygen transport properties of thiol-ene networks', *Macromolecules* **42**(18), 7031–7041.

Lardner, T. J. & Pujara, P. (1980), Xii – compression of spherical cells, *in* S. Nemat-Nasser, ed., 'Mechanics Today', Pergamon, pp. 161 – 176.

Latnikova, A. & Jobmann, M. (2017), 'Towards Microcapsules with Improved Barrier Properties', *Topics in Current Chemistry* **375**(3), 64.

Lei, C., Li, Q., Yang, L., Deng, F., Li, J., Ye, Z., Wang, Y. & Zhang, Z. (2019), 'Controlled reversible buckling of polydopamine spherical microcapsules: revealing the hidden rich phenomena of post-buckling of spherical polymeric shells', *Soft Matter* **15**(32), 6504–6517.

Leng, Y. (2013), *Materials Characterization : Introduction to Microscopic and Spectroscopic Methods*, John Wiley & Sons, Incorporated, Weinheim, GERMANY.

Leong, K. Y., Abdul Rahman, M. R. & Gurunathan, B. A. (2019), 'Nano-enhanced phase change materials: A review of thermo-physical properties, applications and challenges', *Journal of Energy Storage* **21**, 18–31.

Li, E. Q., Zhang, J. M. & Thoroddsen, S. T. (2013), 'Simple and inexpensive microfluidic devices for the generation of monodisperse multiple emulsions', *Journal of Micromechanics and Microengineering* **24**(1), 15019.

Li, M., Rouaud, O. & Poncelet, D. (2008), 'Microencapsulation by solvent evaporation: State of the art for process engineering approaches', *International Journal of Pharmaceutics* **363**(1-2), 26–39.

Li, Q., Zhou, H. & Hoyle, C. E. (2009*a*), 'The effect of thiol and ene structures on thiol–ene networks: Photopolymerization, physical, mechanical and optical properties', *Polymer* **50**(10), 2237–2245.

Li, Q., Zhou, H. & Hoyle, C. E. (2009*b*), 'The effect of thiol and ene structures on thiol–ene networks: Photopolymerization, physical, mechanical and optical properties', *Polymer* **50**(10), 2237–2245.

Liu, K.-K. (1995), Deformation of cellular entities, PhD thesis, Imperial College London.

Liu, K.-K. (2006), 'Deformation behaviour of soft particles: a review', *Journal of Physics D: Applied Physics* **39**(11), R189–R199.

Liu, K. K., Williams, D. R. & Briscoe, B. J. (1998), 'The large deformation of a single micro-elastomeric sphere', *Journal of Physics D: Applied Physics* **31**(3), 294–303.

Liu, M. (2010), Understanding the mechanical strength of microcapsules and their adhesion on fabric surfaces, PhD thesis, University of Birmingham.

Lundberg, P., Bruin, A., Klijnstra, J. W., Nyström, A. M., Johansson, M., Malkoch, M. & Hult, A. (2010), 'Poly(ethylene glycol)-Based Thiol-ene Hydrogel Coatings-Curing Chemistry, Aqueous Stability, and Potential Marine Antifouling Applications', *ACS Applied Materials & Interfaces* **2**(3), 903–912.

Mavrogiannis, N., Ibo, M., Fu, X., Crivellari, F. & Gagnon, Z. (2016), 'Microfluidics made easy: A robust low-cost constant pressure flow controller for engineers and cell biologists', *Biomicrofluidics* **10**(3), 34107.

Mercadé-Prieto, R., Allen, R., Zhang, Z., York, D., Preece, J. A. & Goodwin, T. E. (2012), 'Failure of elastic-plastic core-shell microcapsules under compression', *AIChE Journal* **58**(9), 2674–2681.

Mercade-Prieto, R & Nguyen, B. (2011), 'Determination of the elastic properties of single microcapsules using micromanipulation and finite element modeling', *Chemical Engineering Science* **66**(10), 2042–2049.

Mercadé-Prieto, R., Nguyen, B., Allen, R., York, D., Preece, J. A., Goodwin, T. E. & Zhang, Z. (2011), 'Determination of the elastic properties of single microcapsules using micromanipulation and finite element modeling', *Chemical Engineering Science* **66**(10), 2042–2049.

Mercadé-Prieto, R. & Zhang, Z. (2012), 'Mechanical characterization of microspheres – capsules, cells and beads: a review', *Journal of Microencapsulation* **29**(3), 277–285.

Mercadé-Prieto, Ruben, Allen, R., York, D., Preece, J. A., Goodwin, T. E. & Zhang, Z. (2011), 'Compression of elastic–perfectly plastic microcapsules using micromanipulation and finite element modelling: Determination of the yield stress', *Chemical engineering science* **66**(9), 1835–1843.

Moore, T., Mumford, K. A., Stevens, G. W. & Webley, P. A. (2018), 'Enhancement in specific absorption rate by solvent microencapsulation', *AIChE Journal* **64**(11), 4066–4079.

Nabavi, S. A. & Vladisavljević, G. T. (2017), 'Prediction and control of drop formation modes in microfluidic generation of double emulsions by single-step emulsification', *Journal of Colloid and Interface Science* **505**, 315–324.

Nabavi, S. A., Vladisavljević, G. T., Gu, S. & Manović, V. (2016), 'Semipermeable Elastic Microcapsules for Gas Capture and Sensing', *Langmuir* **32**(38), 9826–9835.

Nabavi, S. A., Vladisavljević, G. T. & Manović, V. (2017), 'Mechanisms and control of single-step microfluidic generation of multi-core double emulsion droplets', *Chemical Engineering Journal* **322**, 140–148.

Nair, D. P., Cramer, N. B., Scott, T. F., Bowman, C. N. & Shandas, R. (2010), 'Photopolymerized thiol-ene systems as shape memory polymers', *Polymer* **51**(19), 4383–4389.

Narayanan, T. S. N. S., Park, I.-S. & Lee, M.-H. (2015), 2 - Surface modification of magnesium and its alloys for biomedical applications: Opportunities and challenges, *in* T. S. N. S. Narayanan, I.-S. Park & M.-H. Lee, eds, 'Surface Modification of Magnesium and its Alloys for Biomedical Applications', Woodhead Publishing, Oxford.

Neikov, O. D. (2019), Chapter 14 - Processing of Powders and Processing Equipment, *in* O. D. Neikov, S. S. Naboychenko & N. A. Yefimov, eds, 'Handbook of Non-Ferrous Metal Powders (Second Edition)', Elsevier, Oxford, pp. 403–455.

Ninni, L., Burd, H., Fung, W. H. & Meirelles, A. J. A. (2003), 'Kinematic Viscosities of Poly(ethylene glycol) Aqueous Solutions', *Journal of Chemical & Engineering Data* **48**(2), 324–329.

N'Tsoukpoe, K. E., Le Pierrès, N. & Luo, L. (2010), Theoretical Investigation of a Long-Term Solar Energy Storage Based on LiBr/H2O Absorption Cycle, *in* 'Eurosun'.

N'Tsoukpoe, K. E., Schmidt, T., Rammelberg, H. U., Watts, B. A. & Ruck, W. K. (2014), 'A systematic multi-step screening of numerous salt hydrates for low temperature thermochemical energy storage', *Applied Energy* **124**, 1–16.

Okushima, S., Nisisako, T., Torii, T. & Higuchi, T. (2004), 'Controlled Production of Monodisperse Double Emulsions by Two-Step Droplet Breakup in Microfluidic Devices', *Langmuir* **20**(23), 9905–9908.

Ostrovskii, N. M., Chumakova, N. A., Bukhavtsova, N. M., Vernikovskaya, N. V. & Aristov, Y. I. (2007), 'Modeling of the limiting step of water sorption by composite sorbents of the "calcium chloride in porous matrix" type', *Theoretical Foundations of Chemical Engineering* **41**(1), 83–90.

O'Sullivan, J. D. B., Behnsen, J., Starborg, T., MacDonald, A. S., Phythian-Adams, A. T., Else, K. J., Cruickshank, S. M. & Withers, P. J. (2018), 'X-ray micro-computed tomography (μCT): an emerging opportunity in parasite imaging', *Parasitology* **145**(7), 848–854.

Paret, N., Trachsel, A., Berthier, D. L. & Herrmann, A. (2015), 'Controlled Release of Encapsulated Bioactive Volatiles by Rupture of the Capsule Wall through the Light-Induced Generation of a Gas', *Angewandte Chemie International Edition* **54**(7), 2275–2279.

Perignon, C., Ongmayeb, G., Neufeld, R., Frere, Y. & Poncelet, D. (2015), 'Microencapsulation by interfacial polymerisation: membrane formation and structure', *Journal of Microencapsulation* **32**(1), 1–15.

Podgórski, M., Wang, C., Yuan, Y., Konetski, D., Smalyukh, I. & Bowman, C. N. (2016), 'Pristine Polysulfone Networks as a Class of Polysulfide-Derived High-Performance Functional Materials', *Chemistry of Materials* **28**(14), 5102–5109.

Quilliet, C. (2012), 'Numerical deflation of beach balls with various poisson's ratios: from sphere to bowl's shape', *The European Physical Journal E* **35**(6), 1–9.

Rapp, B. E. (2017*a*), Chapter 1 - Introduction, *in* B. E. Rapp Mechanics and Mathematics, ed., 'Micro and Nano Technologies', Elsevier, Oxford, pp. 3–7.

Rapp, B. E. (2017*b*), Chapter 17 - Hydraulic Resistance, *in* B. E. Rapp Mechanics and Mathematics, ed., 'Micro and Nano Technologies', Elsevier, Oxford, pp. 351–370.

Ristić, A., Logar, N. Z., Henninger, S. K. & Kaučič, V. (2012), 'The Performance of Small-Pore Microporous Aluminophosphates in Low-Temperature Solar Energy Storage: The Structure–Property Relationship', *Advanced Functional Materials* **22**(9), 1952–1957.

Ristić, A. & Zabukovec Logar, N. (2018), 'New Composite Water Sorbents CaCl2-PHTS for Low-Temperature Sorption Heat Storage: Determination of Structural Properties', *Nanomaterials* **9**(1), 27.

Rydholm, A. E., Bowman, C. N. & Anseth, K. S. (2005), 'Degradable thiol-acrylate photopolymers: polymerization and degradation behavior of an in situ forming biomaterial', *Biomaterials* **26**(22), 4495–4506.

Santiago, R., Lemus, J., Moya, C., Moreno, D., Alonso-Morales, N. & Palomar, J. (2018), 'Encapsulated Ionic Liquids to Enable the Practical Application of Amino Acid-Based Ionic Liquids in CO2 Capture', *ACS Sustainable Chemistry & Engineering* **6**(11), 14178–14187.

Schoukens, G. (2009), Bioactive dressings to promote wound healing, *in* S. Rajendran, ed., 'Advanced Textiles for Wound Care', Woodhead Publishing Series in Textiles, Woodhead Publishing, pp. 114–152.
URL: *https://www.sciencedirect.com/science/article/pii/B9781845692711500054*

Schraml-Marth, M., Walther, K. L., Wokaun, A., Handy, B. E. & Baiker, A. (1992), 'Porous silica gels and TiO2/SiO2 mixed oxides prepared via the sol-gel process: characterization by spectroscopic techniques', *Journal of Non-Crystalline Solids* **143**, 93–111.

Scott, D. W. (1979), 'On optimal and data-based histograms', *Biometrika* **66**(3), 605–610.

Seemann, R., Brinkmann, M., Pfohl, T. & Herminghaus, S. (2011), 'Droplet based microfluidics', *Reports on Progress in Physics* **75**(1), 16601.

Shima, S., Tatara, Y., Iio, M., Shu, C. & Lucero, C. J. (1993), 'Large Deformations of a Rubber Sphere under Diametral Compression : Part 2 : Experiments on Many Rubber Materials and Comparisons of Theories with Experiments', *JSME international journal. Ser. A, Mechanics and material engineering* **36**(2), 197–205.

Sierke, J. & Ellis, A. V. (2019), 'Cross-linking of dehydrofluorinated pvdf membranes with thiol modified polyhedral oligomeric silsesquioxane (poss) and pure water flux analysis', *Journal of Membrane Science* **581**, 362 – 372.

Sircar, S. & Hufton, J. R. (2000), 'Why Does the Linear Driving Force Model for Adsorption Kinetics Work?', *Adsorption* **6**(2), 137–147.

Smith, K. E., Sawicki, S., Hyjek, M. A., Downey, S. & Gall, K. (2009), 'The effect of the glass transition temperature on the toughness of photopolymerizable (meth)acrylate networks under physiological conditions', *Polymer* **50**(21), 5112–5123.

Solé, A., Martorell, I. & Cabeza, L. F. (2015), 'State of the art on gas–solid thermochemical energy storage systems and reactors for building applications', *Renewable and Sustainable Energy Reviews* **47**, 386–398.

Soppimath, S., Kulkarni, A., Aminabhavi, T. M. & Bhaskar, K. (2001), 'Cellulose acetate microspheres prepared by o/w emulsification and solvent evaporation method', *Journal of Microencapsulation* **18**(6), 811–817.

Stenson, J. D., Thomas, C. R. & Hartley, P. (2009), 'Modelling the mechanical properties of yeast cells', *Chemical Engineering Science* **64**(8), 1892–1903.

Sticker, D., Geczy, R., Häfeli, U. O. & Kutter, J. P. (2020), 'Thiol–Ene Based Polymers as Versatile Materials for Microfluidic Devices for Life Sciences Applications', *ACS Applied Materials & Interfaces* **12**(9), 10080–10095.

Stolaroff, J. K., Ye, C., Oakdale, J. S., Baker, S. E., Smith, W. L., Nguyen, D. T., Spadaccini, C. M. & Aines, R. D. (2016), 'Microencapsulation of advanced solvents for carbon capture', *Faraday Discussions* **192**(0), 271–281.

Stovall, K. D., Hoyle, C. E. & Otaigbe, J. U. (2004), 'Comparative study of novel thiol-ene resins and composites', *RadTech Report* **18**(3), 26–29.

Sturges, H. A. (1926), 'The choice of a class interval', *Journal of the american statistical association* **21**(153), 65–66.

Sun, G. & Zhang, Z. (2002), 'Mechanical strength of microcapsules made of different wall materials', *International Journal of Pharmaceutics* **242**(1), 307–311.

Taber, L. A. (1982), 'Large Deflection of a Fluid-Filled Spherical Shell Under a Point Load', *Journal of Applied Mechanics* **49**(1), 121–128.

Tan, Y., Sun, D., Huang, W. & Cheng, S. H. (2008), 'Mechanical modeling of biological cells in microinjection', *IEEE Transactions on NanoBioscience* **7**(4), 257–266.

Tanaka, S. (1992), 'Theory of power-compensated DSC', *Thermochimica Acta* **210**, 67–76.

Tatara, Y. (1993), 'Large Deformations of a Rubber Sphere under Diametral Compression : Part 1 : Theoretical Analysis of Press Approach, Contact Radius and Lateral Extension', *JSME international journal. Ser. A, Mechanics and material engineering* **36**(2), 190–196.

Thompson, B., Riche, C. T., Movsesian, N., Bhargava, K. C., Gupta, M. & Malmstadt, N. (2016), 'Engineered hydrophobicity of discrete microfluidic elements for double emulsion generation', *Microfluidics and Nanofluidics* **20**(5), 78.

Utada, A. S., Fernandez-Nieves, A., Stone, H. A. & Weitz, D. A. (2007), 'Dripping to Jetting Transitions in Coflowing Liquid Streams', *Physical Review Letters* **99**(9), 094502.

Utada, A. S., Lorenceau, E., Link, D. R., Kaplan, P. D., Stone, H. A. & Weitz, D. A. (2005), 'Monodisperse Double Emulsions Generated from a Microcapillary Device', *Science* **308**(5721), 537 LP – 541.

Van Campen, L., Amidon, G. L. & Zografi, G. (1983), 'Moisture Sorption Kinetics for Water-Soluble Substances I: Theoretical Considerations of Heat Transport Control', *Journal of Pharmaceutical Sciences* **72**(12), 1381–1388.

van Herk, A. M. & Gilbert, R. G. (2013), 'Emulsion Polymerisation'.

Vasta, S., Brancato, V., La Rosa, D., Palomba, V., Restuccia, G., Sapienza, A. & Frazzica, A. (2018), 'Adsorption Heat Storage: State-of-the-Art and Future Perspectives.', *Nanomaterials (Basel, Switzerland)* **8**(7).

Vericella, J. J., Baker, S. E., Stolaroff, J. K., Duoss, E. B., Hardin, J. O., Lewicki, J., Glogowski, E., Floyd, W. C., Valdez, C. A., Smith, W. L., Satcher, J. H., Bourcier, W. L., Spadaccini, C. M., Lewis, J. A. & Aines, R. D. (2015), 'Encapsulated liquid sorbents for carbon dioxide capture', *Nature Communications* **6**(1), 6124.

Vladisavljević, G. T., Shahmohamadi, H., Das, D. B., Ekanem, E. E., Tauanov, Z. & Sharma, L. (2014), 'Glass capillary microfluidics for production of monodispersed poly (dl-lactic acid) and polycaprolactone microparticles: Experiments and numerical simulations', *Journal of Colloid and Interface Science* **418**, 163–170.

Wang, C. X., Wang, L. & Thomas, C. R. (2004), 'Modelling the Mechanical Properties of Single Suspension-Cultured Tomato Cells', *Annals of Botany* **93**(4), 443–453.

Wang, Hui, Chen, Y., Li, J., Guo, L. & Fang, M. (2020), 'Review of Encapsulated Salt Hydrate Core-Shell Phase Change Materials', *KONA Powder and Particle Journal* p. 2020010.

Wang, N., Semprebon, C., Liu, H., Zhang, C. & Kusumaatmaja, H. (2020), 'Modelling double emulsion formation in planar flow-focusing microchannels', *Journal of Fluid Mechanics* **895**, A22.

Wang, R. Z., Xu, Z. Y. & Ge, T. S. (2016), 1 - Introduction to solar heating and cooling systems, *in* R. Z. Wang & T. S. Ge, eds, 'Advances in Solar Heating and Cooling', Woodhead Publishing, pp. 3–12.

Wang, T., Chen, J., Zhou, T. & Song, L. (2018), 'Fabricating Microstructures on Glass for Microfluidic Chips by Glass Molding Process'.

Watanabe, T., G. Lopez, C., Douglas, J. F., Ono, T. & Cabral, J. T. (2014), 'Microfluidic Approach to the Formation of Internally Porous Polymer Particles by Solvent Extraction', *Langmuir* **30**(9), 2470–2479.

Wei, C., Yu, C., Wu, J. J., Li, J., Li, S., Dai, S. & Li, T. (2019), 'Easy-to-operate fabrication of tapered glass capillaries for microdroplet generation', *Journal of Micromechanics and Microengineering* **29**(3), 037001.

Wijmans, J. & Baker, R. (1995), 'The solution-diffusion model: a review', *Journal of Membrane Science* **107**(1), 1 – 21.

Wlodarczyk, K. L., Hand, D. P. & Maroto-Valer, M. M. (2019), 'Maskless, rapid manufacturing of glass microfluidic devices using a picosecond pulsed laser', *Scientific Reports* **9**(1), 20215.

Wu, S. (2010), 4 - Heat energy storage and cooling in buildings, *in* M. R. Hall, ed., 'Materials for Energy Efficiency and Thermal Comfort in Buildings', Woodhead Publishing, pp. 101–126.

Wu, W., You, T. & Leung, M. (2019), 'Screening of novel water/ionic liquid working fluids for absorption thermal energy storage in cooling systems', *International Journal of Energy Research* **n/a**(n/a).

Yan, T., Li, T. X. & Wang, R. Z. (2016), 18 - Thermochemical heat storage for solar heating and cooling systems, *in* R. Z. Wang & T. S. Ge, eds,

'Advances in Solar Heating and Cooling', Woodhead Publishing, pp. 491–522.

Yan, Y., Zhang, Z., Stokes, J. R., Zhou, Q.-Z., Ma, G.-H. & Adams, M. J. (2009), 'Mechanical characterization of agarose micro-particles with a narrow size distribution', *Powder Technology* **192**(1), 122–130.

Yashin, V. V. & Balazs, A. C. (2004), 'Theoretical model of interfacial polymerization', *The Journal of Chemical Physics* **121**(22), 11440–11454.

Yu, N., Wang, R. & Wang, L. (2013), 'Sorption thermal storage for solar energy', *Progress in Energy and Combustion Science* **39**(5), 489–514.

Yu, W., Wang, T., Park, A.-H. A. & Fang, M. (2020), 'Towards Sustainable Energy and Materials: CO2 Capture using Microencapsulated Sorbents', *Industrial & Engineering Chemistry Research* .

Yun, Y., Ma, R., Zhang, W., Fane, A. & Li, J. (2006), 'Direct contact membrane distillation mechanism for high concentration nacl solutions', *Desalination* **188**(1), 251 – 262. Integrated Concepts in Water Recycling.

Zahir, M. H., Mohamed, S. A., Saidur, R. & Al-Sulaiman, F. A. (2019), 'Supercooling of phase-change materials and the techniques used to mitigate the phenomenon', *Applied Energy* **240**, 793–817.

Zettl, B., Englmair, G. & Steinmaurer, G. (2014), 'Development of a revolving drum reactor for open-sorption heat storage processes', *Applied Thermal Engineering* **70**(1), 42–49.

Zhang, H., Sun, S., Wang, X. & Wu, D. (2011), 'Fabrication of microencapsulated phase change materials based on n-octadecane core and silica shell through interfacial polycondensation', *Colloids and Surfaces A: Physicochemical and Engineering Aspects* **389**(1), 104–117.

Zhang, H. & Wang, X. (2009), 'Fabrication and performances of microencapsulated phase change materials based on n-octadecane core and resorcinol-modified melamine–formaldehyde shell', *Colloids and Surfaces A: Physicochemical and Engineering Aspects* **332**(2), 129–138.

Zhang, W., Qu, L., Pei, H., Qin, Z., Didier, J., Wu, Z., Bobe, F., Ingber, D. E. & Weitz, D. A. (2019), 'Controllable Fabrication of Inhomogeneous Microcapsules for Triggered Release by Osmotic Pressure', *Small* **15**(42), 1903087.

Zhang, Z., Ferenczi, M. A., Lush, A. C. & Thomas, C. R. (1991), 'A novel micromanipulation technique for measuring the bursting strength of single mammalian cells', *Applied Microbiology and Biotechnology* **36**(2), 208–210.

Zhang, Z., Ferenczi, M. A. & Thomas, C. R. (1992), 'A micromanipulation technique with a theoretical cell model for determining mechanical properties of single mammalian cells', *Chemical Engineering Science* **47**(6), 1347–1354.

Zhang Z., G. S. (2001), 'Mechanical properties of melamine-formaldehyde microcapsules', *Journal of Microencapsulation* **18**(5), 593–602.

Zhou, C., Yue, P. & Feng, J. J. (2006), 'Formation of simple and compound drops in microfluidic devices', *Physics of Fluids* **18**(9), 92105.

Zhu, P., Kong, T., Kang, Z., Tian, X. & Wang, L. (2015), 'Tip-multi-breaking in capillary microfluidic devices', *Scientific reports* **5**, 11102.

Zhu, P. & Wang, L. (2017), 'Passive and active droplet generation with microfluidics: a review', *Lab on a Chip* **17**(1), 34–75.

Zondag, H. (2015), 'Sorption Heat Storage', *Solar Energy Storage* pp. 135–154.